NASA/TM—2005-213645

Thermal and Mechanical Property Characterization of the Advanced Disk Alloy LSHR

Timothy P. Gabb, John Gayda, and Jack Telesman
Glenn Research Center, Cleveland, Ohio

Peter T. Kantzos
Ohio Aerospace Institute, Brook Park, Ohio

June 2005

The NASA STI Program Office . . . in Profile

Since its founding, NASA has been dedicated to the advancement of aeronautics and space science. The NASA Scientific and Technical Information (STI) Program Office plays a key part in helping NASA maintain this important role.

The NASA STI Program Office is operated by Langley Research Center, the Lead Center for NASA's scientific and technical information. The NASA STI Program Office provides access to the NASA STI Database, the largest collection of aeronautical and space science STI in the world. The Program Office is also NASA's institutional mechanism for disseminating the results of its research and development activities. These results are published by NASA in the NASA STI Report Series, which includes the following report types:

- TECHNICAL PUBLICATION. Reports of completed research or a major significant phase of research that present the results of NASA programs and include extensive data or theoretical analysis. Includes compilations of significant scientific and technical data and information deemed to be of continuing reference value. NASA's counterpart of peer-reviewed formal professional papers but has less stringent limitations on manuscript length and extent of graphic presentations.

- TECHNICAL MEMORANDUM. Scientific and technical findings that are preliminary or of specialized interest, e.g., quick release reports, working papers, and bibliographies that contain minimal annotation. Does not contain extensive analysis.

- CONTRACTOR REPORT. Scientific and technical findings by NASA-sponsored contractors and grantees.

- CONFERENCE PUBLICATION. Collected papers from scientific and technical conferences, symposia, seminars, or other meetings sponsored or cosponsored by NASA.

- SPECIAL PUBLICATION. Scientific, technical, or historical information from NASA programs, projects, and missions, often concerned with subjects having substantial public interest.

- TECHNICAL TRANSLATION. English-language translations of foreign scientific and technical material pertinent to NASA's mission.

Specialized services that complement the STI Program Office's diverse offerings include creating custom thesauri, building customized databases, organizing and publishing research results . . . even providing videos.

For more information about the NASA STI Program Office, see the following:

- Access the NASA STI Program Home Page at ***http://www.sti.nasa.gov***

- E-mail your question via the Internet to help@sti.nasa.gov

- Fax your question to the NASA Access Help Desk at 301–621–0134

- Telephone the NASA Access Help Desk at 301–621–0390

- Write to:
  NASA Access Help Desk
  NASA Center for AeroSpace Information
  7121 Standard Drive
  Hanover, MD 21076

NASA/TM—2005-213645

Thermal and Mechanical Property Characterization of the Advanced Disk Alloy LSHR

Timothy P. Gabb, John Gayda, and Jack Telesman
Glenn Research Center, Cleveland, Ohio

Peter T. Kantzos
Ohio Aerospace Institute, Brook Park, Ohio

National Aeronautics and
Space Administration

Glenn Research Center

June 2005

Acknowledgments

The authors wish to acknowledge the support of NASA GRC programs Aviation Safety and HOTPC. Disk forging was performed at Wyman-Gordon Forgings under the direction of Ian Dempster. Disk heat treatments were performed at Ladish Forgings, Inc., under the direction of Joe Lemskey.

Available from

NASA Center for Aerospace Information
7121 Standard Drive
Hanover, MD 21076

National Technical Information Service
5285 Port Royal Road
Springfield, VA 22100

Available electronically at http://gltrs.grc.nasa.gov

Thermal and Mechanical Property Characterization of the Advanced Disk Alloy LSHR

Timothy P. Gabb, John Gayda, and Jack Telesman
National Aeronautics and Space Administration
Glenn Research Center
Cleveland, Ohio 44135

Peter T. Kantzos
Ohio Aerospace Institute
Brook Park, Ohio 44142

Abstract

A low solvus, high refractory (LSHR) powder metallurgy disk alloy was recently designed using experimental screening and statistical modeling of composition and processing variables on sub-scale disks to have versatile processing-property capabilities for advanced disk applications. The objective of the present study was to produce a scaled-up disk and apply varied heat treat processes to enable full-scale demonstration of LSHR properties. Scaled-up disks were produced, heat treated, sectioned, and then machined into specimens for mechanical testing. Results indicate the LSHR alloy can be processed to produce fine and coarse grain microstructures with differing combinations of strength and time-dependent mechanical properties, for application at temperatures exceeding 1300 °F.

Introduction

A series of experimental powder metallurgy disk alloys were recently evaluated for their processing characteristics and high temperature mechanical properties (ref. 1). Disks were subsolvus and supersolvus heat treated, then quenched using procedures designed to reproduce the cooling paths expected in large-scale disks. Mechanical tests were then performed at 1000, 1300, and 1500 °F. Several alloys had superior tensile and creep properties at 1300 °F and higher temperatures, but were difficult to process and prone to quench cracking, chiefly due to their high gamma prime solvus temperature. Several other alloys had more favorable processing characteristics due to their lower gamma prime solvus temperature and balanced time-dependent properties at 1300 °F. Results indicated an experimental low solvus, high refractory (LSHR) alloy could build upon the best attributes of all these alloys, giving exceptional tensile and creep properties at high temperatures with versatile processing characteristics due to a low gamma prime solvus.

The objective of this study was to verify the mechanical properties of this LSHR alloy using scaled-up material processing and disks. This would enable assessments of the processing-property and maximum temperature capabilities of this disk alloy for different potential applications in the engine community. Scaled-up disks were processed, machined into specimens, and tested in tensile, creep, fatigue, and fatigue crack growth tests by NASA Glenn Research Center (GRC) and test vendors. Results were compared to data previously generated on specimens from subscale disks.

Materials and Procedure

Powder of LSHR superalloy having the composition in weight percent listed in table 1 was atomized by Special Metals Corp. in argon and passed through screens of –270 mesh to give powder particle diameters of no more than about 55 μm. The powder was then sealed in a stainless steel container, hot compacted, and extruded at a reduction ratio of 6:1. Segments of the extrusion billet were machined to mults 6 in. diameter and 8 in. long, then isothermally forged into flat disks about 12 in. diameter and 2 in. thick by Wyman-Gordon Forgings. Two contoured disks were then prepared with an outer diameter of near 12 in., maximum bore thickness of near 2 in., and rim thickness of near 1.5 in. (ref. 18). These disks were then solution heat treated at Ladish, Co. either above or below the gamma prime solvus temperature, estimated at about 2120 °F. A "supersolvus" disk was solution heat treated at about 2140 °F for 2.5 h, then rapidly transferred, in under 30 seconds, to a station for fan cooling. The "subsolvus" disk was solution heat treated at about 2070 °F for 2.5 h, then rapidly transferred, in under 30 seconds, for a quench immersion in agitated oil. These quenching procedures were selected to typify those employed in quenching supersolvus and subsolvus disks of current alloys. The disks were then given a simple aging heat treatment of about 1500 °F for 8 h.

A spare disk of the same dimensions was prepared with numerous thermocouples embedded at different depths in the bore, web, and rim, then given the same supersolvus and subsolvus solution heat treatments. As expected, the oil-quenched subsolvus heat treatment produced much faster average cooling rates of 275 to 730 °F/min. than the fan air quenched supersolvus heat treatment of 65 to 165 °F/min. The temperature-time data recorded from the thermocouples during fan air and oil quenching cycles were analyzed using a commercial heat transfer computer code in order to assign approximate cooling rates, averaged over the temperature range of solution temperature to 1600 °F, for each specimen.

Thermophysical properties were measured on duplicate samples from supersolvus and subsolvus disks by Thermophysical Properties Research Laboratory, Inc. (TPRL) and GRC. Thermal diffusivity (α) was measured at TPRL using the laser flash technique according to ASTM E1461. Specific heat (C_p) was measured at TPRL using a differential scanning calorimeter according to ASTM E1269. Density (d) was measured at GRC using the immersion technique with a methyl ethyl ketone solution, in general accordance with ASTM B311. Thermal conductivity (λ) values were calculated using the equation:

$$\lambda = \alpha\, C_p\, d.$$

Thermal expansion was measured at TPRL using a push-rod dilatometer according to ASTM E228. The mean coefficient of thermal expansion was calculated using the change in length from that at a reference temperature (T_0) of 70 °F using the equation:

$$\text{Mean CTE} = ((L_T - L_0)/L_0)/(T - T_0).$$

Elastic modulus was measured at GRC using the impulse excitation technique according to ASTM E1875. Young's modulus was measured from 70 to 2000 °F. Shear modulus was measured at 70 °F. Poisson's ratio (μ) was then calculated for 70 °F using the equation:

$$\mu = (E/2G) - 1\ .$$

An extensive mechanical testing matrix was employed for the scaled-up disks included tensile, notched tensile, creep, low cycle fatigue, and fatigue crack growth tests. Tests were performed on specimens from both supersolvus and subsolvus heat treated disks. Tensile tests were performed at temperatures of 75 to 1500 °F. Creep tests were performed from 1200 to 1500 °F. Low cycle fatigue tests were performed at 800 and 1300 °F. Cyclic crack growth tests were performed from 75 to 1300 °F, while dwell crack growth tests were performed at 1200 and 1300 °F.

Tensile Tests

Tensile tests were performed at Westmoreland Mechanical Testing & Research, Inc. (WMTR) and GRC on specimens machined by WMTR having a gage diameter of 0.16 in. and gage length of 1 in. in uniaxial test machines employing a resistance heating furnace and axial extensometer. The tests were performed according to ASTM E21, using an initial test segment with strain increased at a uniform rate of 0.2 percent/min., followed by a segment with displacement increased at a uniform rate of 0.2 in./min. Notched tensile specimen machining and testing were performed using specimens having a minimum gage diameter of 0.16 in. and stress concentration factor $K_t = 3.5$ in a uniaxial test machine. Notch tensile tests were performed according to ASTM E602.

Creep Tests

Machining and testing of scaled-up disk creep specimens were performed by WMTR. Specimens having a gage diameter of 0.25 in. and gage length of 1.5 in. were machined and tested in uniaxial lever arm constant load creep frames using resistance heating furnaces and shoulder-mounted extensometers. The creep tests were performed according to ASTM E139.

Fatigue Tests

Machining and testing of low cycle fatigue specimens having a uniform gage diameter of 0.25 in. across a gage length of 0.75 in. were performed by WMTR. The low cycle fatigue (LCF) specimens were tested using uniaxial closed-loop servo-hydraulic testing machines with resistance heating furnaces and axial extensometers. Tests were performed according to ASTM E606. A frequency of 0.33 hertz was employed in strain-controlled fatigue testing for the first 6 hours of cycling. A strain ratio ($R_\varepsilon=\varepsilon_{min}/\varepsilon_{max}$) of 0 was used. After 6 hours of testing in this manner, surviving specimens were then cycled to the same stabilized stresses using a load-controlled cycle at a faster frequency of 10 hertz until failure.

Machining of a smaller number of cylindrical notched fatigue specimens having a notch diameter of 0.188 in. and geometric stress concentration factor K_t of 2.0 was performed by WMTR. These specimens were tested using a uniaxial closed-loop servo-hydraulic testing machine with a resistance heating furnace at NASA GRC, to screen notch effects on fatigue life. Tests were performed according to ASTM E466. A frequency of 10 hertz was employed in load-controlled cycles with a stress ratio ($R_\sigma=\sigma_{min}/\sigma_{max}$) of 0.05 in most tests. Several additional tests were performed at GRC with a superimposed dwell of 90 s at maximum stress in each cycle.

Fatigue Crack Growth Tests

Machining of fatigue crack growth specimens from scaled-up disks was performed by WMTR. All specimens had a rectangular gage section 0.4 in. wide and 0.18 in. thick, with a surface flaw (ref. 2) on one side of the gage section about 0.014 in. wide and 0.007 in. deep, produced by electro-discharge machining. The fatigue crack growth specimens were then tested at GRC in general accordance with ASTM E647. Tests were performed in a closed-loop servohydraulic test machine using resistance heating and potential drop measurement of crack growth. Precracking was performed at room temperature. Tests were then performed at elevated temperatures using a maximum stress of 90 ksi. Cyclic tests were performed at a frequency of 0.33 hertz. Dwell tests were performed with a 90 s dwell at maximum stress in each cycle. A stress ratio ($R_\sigma = \sigma_{min}/\sigma_{max}$) of 0.05 was used in all crack growth tests.

Fracture surfaces of selected specimens were evaluated by scanning electron microscopy. Cracking modes and grain sizes were also examined on metallographically prepared sections. Grain sizes were determined from grip sections of tensile specimens according to ASTM E112 linear intercept procedures using circular grid overlays, and As-Large-As (ALA) grain sizes were determined using E930. Precipitate and carbide microstructures and phase chemistries were also inspected from these specimens using field emission scanning electron microscopy (FESEM) with energy dispersive X-ray spectroscopy (EDS). Phase extractions were employed on tensile specimen grip sections to enable determination of γ' and γ phase chemistries using inductively coupled plasma mass spectrometry. X-ray diffraction was used on filtered extraction residues to verify γ' and carbide phase identities and lattice parameters. The electrolyte for γ/γ' phase extraction was 10 g per liter of citric acid and 10 g per liter of ammonium sulfate in deionized water. The electrolyte for carbide phase extraction was 90 percent methanol and 10 percent HCl by volume with 10 grams per liter of tartaric acid. Transmission electron microscopy on thinned foils was employed where necessary to confirm minor phase chemistry and crystal structure, using EDS and selected area diffraction patterns.

Results and Discussion

Material and Microstructures

The actual chemistry in weight percent of the LSHR alloy is listed in table 1. Typical grain microstructures in optical images of etched metallographic sections of tensile specimen grip sections are shown in figure 1. These tensile specimens were from the disks' bore regions cooled more slowly during quenching, and rim regions cooled more quickly. Supersolvus specimens had ASTM mean grain sizes (G) of 7.1 (31 μm) for the bore and 6.8 (34 μm) for the rim. The bore and rim specimens had ALA grain sizes of 3.5 (105 μm) and 2.5 (150 μm), respectively. Subsolvus specimens had a mean grain size of 11.3 (7.3 μm) for the bore and 11.0 (8 μm) for the rim, with ALA grain sizes of 7.5 (27 μm) and 8.5 (19 μm). Subsolvus specimens had coarse, undissolved "primary" γ' particles spaced along grain boundaries and sometimes widely scattered within grains.

The typical minor phases observed are shown in the FESEM images of figure 2. Relatively large, angular precipitates between 0.3 and 1.5 μm in diameter were observed within grains and sometimes at grain boundaries. They were determined by energy dispersive x-ray spectroscopy (EDS) analyses to contain tungsten, molybdenum, chromium, and boron. FESEM EDS and TEM selected area diffraction patterns indicated they were $(W,Mo,Cr)_3B_2$ particles, as shown in figure 3. Smaller MC carbides between 0.2 and 0.5 μm in diameter were also scattered within the grains. They were determined by EDS analyses to also contain tantalum, niobium, and titanium. FESEM EDS and TEM microdiffraction patterns indicated they were (Ta,Nb,Ti)C particles, as shown in figure 3. Very fine $M_{23}C_6$ carbides between 0.05 and 0.2 μm in thickness were observed along many grain boundaries. EDS was more difficult for these very fine carbides due to background γ–γ' peak interferences, but these carbides appeared to contain Cr, W, and Mo.

Typical γ' precipitate microstructures from tensile specimen grip sections are also shown in field emission microscopy images of figure 4. Within the grains of the supersolvus specimen from the disk bore, three populations of γ' precipitates were evident. Scattered large precipitates (0.3 to 0.5 μm wide) appeared to have preferentially grown at the cube corners, giving consistently oriented star shapes. Such large precipitates have been observed in previous work (ref. 3), including for bore sections of disk superalloys (ref. 4). Intermediate size precipitates (0.15 to 0.3 μm wide) had a rounded cube shape. They sometimes appeared to be sectioned lobes of the large precipitates, but in other instances appeared to be isolated precipitates. Small quantities of fine, spherical precipitates (0.02 to 0.05 μm wide) were also

observed scattered throughout the microstructure. The supersolvus rim specimen only had simpler, rounded cuboid precipitates 0.1 to 0.25 μm wide, and fine spherical precipitates 0.02 to 0.05 μm wide.

Subsolvus specimens had less distinct differences in γ′ precipitates between the bore and rim locations. Bore specimens had rounded cuboid precipitates 0.1 to 0.25 μm wide, with minor preferential growth of some corners for scattered large particles. Rim specimens had round cuboid precipitates 0.08 to 0.15 μm wide. Both bore and rim specimens had fine spherical precipitates 0.01 to 0.03 μm wide scattered between larger precipitates, and surrounding primary γ′ particles. Coarse, undissolved "primary" γ′ particles (0.6 to 3 μm wide) were spaced along grain boundaries and sometimes widely scattered within grains.

Both γ′ and carbide phase extractions were performed. Averaging over four γ′ extractions, 50.8 ± 0.4 weight percent of γ′ phase was extracted. However, the 0.1 μm filter employed would be expected to allow the fine precipitates at smaller diameter to pass through. Therefore, the total weight percent of γ′ phase was estimated to be between 52 and 54 percent. Chemistries of the extracted γ and γ′ phases are listed in table 1, along with the associated γ partitioning ratios defined as:

$$\gamma \text{ partitioning ratio of element E} = (\text{at. \% E in } \gamma)/(\text{at. \% E in } \gamma')$$

Cr, Fe, Mo, and Co strongly partitioned to γ, while Ta, Ti, Nb, and Al strongly partitioned to γ ′, as observed in previous studies of superalloys (ref. 5, 6). W partitioned somewhat more to γ than γ ′, but was present in both phases.

The unconstrained γ′ lattice parameter was measured by X-ray diffraction to be 3.596 ± 0.001 Angstroms. X-ray diffraction of carbide extractions indicated the presence of MC carbides and M_3B_2 borides, along with residual γ′. However, $M_{23}C_6$ carbides were not detected in the carbide extractions. It was again expected that these very fine $M_{23}C_6$ carbides passed through the 0.1 μm filter, and were therefore not successfully isolated. These results were typical of other disk superalloys (ref. 6).

Physical and Thermal Properties

Thermal diffusivity is shown as a function of temperature in figure 5. Thermal diffusivity increased linearly from 0.102 ft^2/h at 70 °F to 0.18 ft^2/h at 1500 °F, then was relatively stable to 2100 °F. Specific heat results are shown as a function of temperature in figure 6. Specific heat increased from about 0.10 BTU/(lb F) at 70 °F to 0.28 BTU/(lb-F) at 2030 °F for subsolvus specimens, then dropped off. Specific heat increased to about 0.30 BTU/(lb-F) at 2080 °F for supersolvus specimens, then dropped off. The density of subsolvus and supersolvus disk specimens was measured to be 0.302 ± 0.0005 lb/in^3, as given in table 2. Calculated thermal conductivity values are shown as a function of temperature in figure 7. Thermal conductivity increased approximately linearly from 5.4 BTU/(h-ft-F) at 70 °F to 16.3 BTU/(h-ft-F) at 2200 °F, with slight positive divergence near 1500 °F. Thermal expansion, instantaneous CTE, and mean CTE are shown as functions of temperature in figure 8. Mean CTE increased from 6.8 μin/(in.-F) at 70 °F to a plateau at 10.6 μin/(in.-F) near 2100 °F. Young's modulus is shown as a function of temperature in figure 9. Young's modulus (E) decreased from about 32.8 Msi at 70 °F to about 17.5 Msi at 2000 °F. Shear modulus (G) and Young's modulus at 70 °F were measured to be 12.73 and 32.74 Msi, and Poisson's ratio (μ) was then calculated to be 0.286 at this temperature, table 3. These results were in general agreement with those obtained from other similar nickel-base superalloys (ref. 7). The test results are tabulated in appendixes 1 through 8.

Tensile Stress-Strain Response

Yield strengths at 0.2 percent offset, ultimate strengths, notched strength, percent elongation after failure, and percent reduction in area after failure are compared as functions of temperature in figures 10 and 11. Polynomial regression was performed on these responses using temperature (T), T^2, and T^3 as the independent variables. The resulting equations and correlation coefficients are listed in the figures, for use in estimating mean strengths and ductilities. Supersolvus yield strength was sustained up to a temperature of 1400 °F, then dropped off with increasing temperature. Subsolvus yield strength was 20 to 30 ksi higher than supersolvus levels, but began dropping at 1300 °F. A similar strength differential between supersolvus and subsolvus specimens applied to ultimate strength. Ultimate strength began dropping off above 1200 °F for supersolvus material, and above 1100 °F for subsolvus material. Notched tensile strengths ran 30 to 50 ksi higher than ultimate strength, with ratios of notched over ultimate strength always exceeding 1.1. Elongation and reduction in area had more variability than strengths, but averaged relatively constant as functions of temperature up to 1300 °F for supersolvus specimens, and up to near 1100 °F for subsolvus specimens. Both then decreased with increasing temperature. Test results of specimens from scaled-up disks are also compared to previously published (ref. 1) subscale LSHR disk results in figures 10 and 11. The scaled-up disks had comparable tensile strength and ductility compared to the subscale disks. These results were also typical of similar disk alloys tested in that study. Tensile strengths often exceeded those reported from powder metallurgy disks of Udimet 720 (refs. 8 to 10) and ME3 (ref. 11). The test results are tabulated in appendixes 8 and 9.

The variabilities of elongation and reduction in area observed in the tensile tests were largely due to cooling rate variations among the test specimens. Strengths and ductilities of full-scale disk specimens are shown versus approximate cooling rate in figures 12 and 13. For the cooling rates encompassed by the disks and associated test specimens, increasing cooling rate sometimes slightly increased yield strength, while ultimate strength was not consistently affected. However, increasing cooling rate significantly decreased elongation and reduction in area at test temperatures of 1300 °F and higher. This was more consistently observed in the elongation measurements, where regression lines are included in the figure. It should be noted that elongation measurements on failed specimens were inherently less difficult to perform and more reproducible than reduction in area measurements, which required final diameter measurements across fracture surfaces of varying irregularity.

Typical tensile fracture surfaces at various temperatures are compared for supersolvus specimens in figure 14 and for subsolvus specimens in figure 15. Supersolvus and subsolvus tensile specimens had predominantly transgranular failure modes by microvoid coalescence in tests from room temperature to 1200 °F. At these temperatures, scattered slip “facet” grain failures were also observed. At higher temperatures of 1300 to 1500 °F, oxidized intergranular surface cracks appeared to first occur, followed by transgranular microvoid coalescence failure in the center of the specimens. Evidently, environmental attack weakened grain boundaries in comparison to grain interiors with increasing temperature. No large differences were observed in general failure modes between low cooling rate specimens exhibiting high ductility and high cooling rate specimens exhibiting low ductility in tests at 1300 to 1500 °F. However, the supersolvus grain surfaces exposed in intergranular surface cracks for low cooling rate specimens did show larger perturbations than for high cooling rate specimens. These perturbations are attributable to the selectively coarsened large γ' precipitates spaced along many grain boundaries in slow cooling rate specimens, producing serrated grain boundaries for the bore specimen as shown in figure 1.

Creep Properties

Time to 0.2 percent creep (t) and rupture of creep tests at temperatures (T) of 1200, 1300, 1400, and 1500 °F were analyzed using the Larson-Miller approach commonly employed for disk alloys. Creep

results were used to generate conventional Larson-Miller curves of stress versus Larson-Miller parameter (LMP) using the equation:

$$LMP = (T + 460\ °R)(\log t + C)/1000$$

The resulting plots are shown in figures 16 and 17. It can be seen that the LMP constant C = 20 did not fully account for test temperature in modeling the time to produce low creep strains of 0.2 percent, but worked reasonably well for rupture life. Regressions indicated a constant of 28 gave the highest correlations for 0.2 percent creep lives in both supersolvus and subsolvus material. Polynomial regression equations using the variables LMP and LMP^2 are included with correlation coefficients in the figures, for use in estimating mean life responses as functions of temperature and stress using this Larson-Miller approach. Test results previously generated from specimens of subscale LSHR disks are also compared to the scaled-up results in figures 16 and 17. The scaled-up material had equal or higher creep lives compared to the sub-scale disks. Supersolvus creep results slightly exceeded that observed for ME3 (ref. 11), while subsolvus creep results significantly exceeded that reported for Udimet 720 (ref. 9).

Times to 0.2 percent creep of the scaled-up disk specimens are shown versus approximate cooling rate in figure 18. Increased cooling rate improved creep life at low temperatures of 1200 to 1300 °F, but reduced creep life at higher temperatures of 1500 °F for supersolvus material and 1400 °F for subsolvus material. The cooling rate effects on creep life were less than 2X for supersolvus material, but could exceed 3X for subsolvus material over the range of cooling rates evaluated. The test results are tabulated in appendix 10.

Supersolvus and subsolvus creep specimens tended to fail from intergranular, surface-initiated cracks at the creep test temperatures of 1200 to 1500 °F, as shown in figures 19 and 20. This was apparently due to environmental attack at grain boundaries. At higher temperatures of 1400 to 1500 °F, exposed grain surfaces on the surface cracks had a more rough, dimpled morphology and more secondary cracking, with evident grain boundary cavitation. The final overload failure occurred by transgranular microvoid coalescence with scattered “facet” crystallographic grain failures at 1200 °F. At increasing temperatures of 1300 to1500 °F, the final overload regions had increasing area fractions of intergranular failure by cavitation at grain boundaries, increasing from 25 percent at 1300 °F to 80 percent at 1500 °F.

Several failed creep specimens with rupture lives of over 3000 hours at 1300 °F were sectioned and metallographically prepared. FESEM evaluations could find no deleterious topologically close packed phases had yet formed. Additional creep tests with test conditions designed for longer rupture lives are currently in test and will be evaluated in a like manner after failure.

Fatigue Properties

Uniform gage tests.—Total strain range versus fatigue life is compared at the test temperatures of 800 and 1300 °F for supersolvus and subsolvus materials with uniform gage specimens in figure 21. Subsolvus material had 2 to 5x higher lives than supersolvus material at 800 °F, with larger differences apparent at low strain ranges. At 1300 °F, subsolvus and supersolvus lives were nearly comparable at high strain ranges, but subsolvus exceeded supersolvus lives by nearly 3x at low strains. This could be due to the higher yield strength of subsolvus over supersolvus materials, allowing less plastic strain and associated damage in each fatigue cycle of a given strain range.

At high strain ranges, fatigue life was higher in tests at 800 °F than at 1300 °F, for both subsolvus and supersolvus materials. This could be due to the higher yield strengths of both materials at 800 °F than 1300 °F, which allowed less plastic strain and associated damage in each fatigue cycle of a given strain range than at 1300 °F. The higher ductilities observed at 800 °F than 1300 °F could also allow more accumulated strain damage before failure initiation. However, at low strain ranges near 0.6 percent, fatigue life was higher in tests at 1300 °F than at 800 °F, for both subsolvus and supersolvus material.

This could be mainly due to the lower yield strength at 1300 °F, which can allow more reductions in positive stresses by way of yielding in tension, both for initial stresses and after repeated cycling or "cyclic shakedown." This could also be related to a higher tolerance of fatigue defects such as large grains and inclusions at the higher temperature, where plastic deformation within grains appeared to be more uniform with no observable slip offsets. The supersolvus material fatigue results were generally comparable to those obtained for ME3 (ref. 11), while the subsolvus fatigue results were generally comparable to that obtained for Udimet 720 (refs. 8 to 10).

A substantial variation in lives is sometimes evident for multiple tests performed at the same strain range. While some scatter is to be expected in fatigue lives, this scatter was also often found to be related to the effects of increasing yield strength with increasing cooling rate, and resulting differences in maximum and minimum stresses generated in strain-controlled tests at the same strain and stress range of different specimens. Maximum stress and stress range as functions of cycles are compared for subsolvus rim and bore specimens both tested at a total strain range of 0.8 percent and 1300 °F in figure 22. These comparative specimens run at the same conditions were purposefully chosen from different locations in the disks, to encompass a wide range of cooling rates. The specimen from the faster cooling rim had more positive maximum stresses than the specimen from the slower cooling bore in tests producing comparable stress ranges, and lower fatigue life. This was the case both for initial stresses generated as the strain range was gradually increased to 0.8 percent, and after cyclic shakedown. Such differences in maximum stresses (σ_{max}) and minimum stresses (σ_{min}), in tests at about the same stress range ($\Delta\sigma$) and strain range ($\Delta\varepsilon$) could be accounted for using an approach of Smith-Watson-Topper (ref. 12):

$$\sigma_{SWT} = (\sigma_{max}\Delta\sigma/2)^{0.5}$$

This relationship accounts for differences in maximum stress as well as stress range. Resulting plots of σ_{swt} versus fatigue life are compared at the test temperatures of 800 and 1300 °F for supersolvus and subsolvus materials with uniform gage specimens in figure 23. Usage of this σ_{swt} parameter or similar approaches to account for differences in maximum and minimum stresses is seen to reduce scatter, and allowed improved correlations in polynomial regressions. The test results are tabulated in appendix 11.

Supersolvus low cycle fatigue specimens predominantly failed from cracks initiated by planar failure of relatively large grains on the specimen surface at 800 °F, as shown in figure 24. These "faceted" grain failures (refs. 11 and 13) appeared to be due to concentrated slip on crystallographic planes, which sometimes produced noticeable slip offsets on the surfaces of large grains, as shown in figure 25. The grain facets were mostly flat with least texture in tests at 800 °F. At 1300 °F, a majority of specimens tested at low strain ranges of 0.6 to 0.8 percent again failed from grain facets. At the lowest strain range of 0.6 percent, the failure initiation sites shifted to internal grains rather than surface grains. The grain facets had more texture in tests at 1300 °F. At higher strain ranges of 0.8 to 1.2 percent, more specimens failed from oxidized surface cracks. These surface cracks were often, but not always intergranular. At both temperatures, more cracks were initiated in tests at higher strain ranges. A much smaller minority of supersolvus specimens failed at 1300 °F from ceramic inclusions. The inclusions initiating failures were evenly segregated between angular, silicon or calcium-rich oxide inclusions broken up into several pieces, often referred to as Type 1 inclusions, and granulated, reactive aluminum-rich oxide Type 2 inclusions (refs. 14 and 15).

Subsolvus low cycle fatigue specimens failed either from grain facets, pores, or inclusions at 800 °F, as shown in figure 26. The grain facets were much smaller than for supersolvus specimens, due to the finer grain size. At 1300 °F, a majority of specimens tested at all strain ranges again failed from inclusions. Several specimens had grain facet initiated failures. At both temperatures, more cracks were again initiated in tests at higher strain ranges. Failures initiated exclusively at the specimen surfaces for strain ranges of 0.8 to 1.2 percent, but often shifted to internal locations at 0.6 percent.

Notched fatigue tests.—Maximum stress across the notched diameter is compared versus fatigue life at the test temperatures of 800 and 1300 °F for supersolvus and subsolvus notched fatigue specimens in

figure 27. Subsolvus material had longer cyclic lives than supersolvus material at low applied stresses at 800 °F, and for all applied stresses at 1300 °F.

At highest stresses, cyclic fatigue life was again higher in tests at 800 °F than at 1300 °F, for both subsolvus and supersolvus material. Here also, this could be due to the higher strengths and ductilities of both materials at 800 °F, which allowed less plastic strain and associated damage in each fatigue cycle at a given stress and more damage accommodation than at 1300 °F. However, at lower stresses, fatigue life was again higher in tests at 1300 °F than at 800 °F, for both subsolvus and supersolvus material. As for unnotched specimens, the lower yield strength at 1300 °F could allow more reductions in positive stresses by way of yielding in tension than at 800 °F, both for initial stresses and after cyclic shakedown. It would be expected that these reductions would be localized near the notch tip where concentrated stresses can exceed the yield strength. This local region of yielding, or plastic zone, near the notch tip would be constrained by surrounding material which is only elastically loaded. Therefore, accounting for these differences in stresses is more difficult than for uniform gage specimens and beyond the scope of this study, requiring elastic-plastic finite element modeling of the notched specimen during fatigue cycling. Yet, it could be possible to employ the stress-strain data generated in the uniform gage tests within such a model, to estimate notched specimen stresses for comparison of the notched and smooth gage fatigue lives.

The results of several additional tests performed at 1300 °F with a superimposed dwell of 90 s at maximum stress in each cycle are also shown in figure 27. Supersolvus life was reduced by about 10X in the two dwell tests performed. Subsolvus life was reduced even more, ranging from 10X to 1000X in the two dwell tests performed on this material. Additional tests are necessary to fully quantify the effects of dwells on notched fatigue life as functions of maximum stress in the two materials, but it is clear that dwells at maximum stress can substantially degrade fatigue life at 1300 °F. Understanding the notch-stress response in these tests would require elastic-viscoplastic finite element modeling of both plastic flow and time-dependent relaxation of stresses near the notch during the dwell fatigue cycling. The test results are tabulated in appendix 12.

Supersolvus and subsolvus notched fatigue specimens invariably had failure initiations at the notch tip. Supersolvus and subsolvus specimens tested in cyclic fatigue at 800 °F had multiple transgranular crack initiations at the notch root, and subsequent transgranular crack growth, as shown in figures 28 and 29. At 1300 °F, supersolvus specimens tested in cyclic fatigue again had multiple transgranular crack initiations at the notch root, and subsequent transgranular crack growth. Subsolvus specimens tested in cyclic fatigue at 1300 °F had transgranular crack initiations at the notch root, then mixed intergranular and transgranular crack growth. Both supersolvus and subsolvus specimens tested at 1300 °F with the superimposed 90 s dwells at maximum stress had intergranular crack initiations along the notch tip and subsequent intergranular crack growth, figures 28 and 29. It appears the intergranular crack initiation mode accounted in part for the lower lives of specimens tested at 1300 °F with the superimposed 90 s dwells.

Fatigue Crack Growth Properties

Cyclic crack growth rate versus stress intensity factor range is compared for all test temperatures in figure 30. Crack growth rates at 25 ksi*in$^{0.5}$ are shown versus temperature in figure 31. Crack growth rates increased with temperature, and were consistently lower for supersolvus specimens than for subsolvus specimens. The increase in crack growth rates with temperature was quite modest, increasing roughly 10X in going from 75 to 1300 °F. Supersolvus crack growth rates were 50 to 70 percent of subsolvus crack growth rates at constant temperature. Linear regression equations modeling cyclic crack growth rates versus temperature are included in these figures, for use in estimating mean crack growth responses as a function of temperature.

Dwell crack growth rate versus stress intensity factor range is compared for test temperatures of 1200 and 1300 °F in figure 32. Crack growth rates at 25 ksi*in$^{0.5}$ are shown versus temperature in figure 33. Supersolvus crack growth rates were more substantially lower than subsolvus rates in the dwell tests compared to 0.33 hertz cyclic tests, with supersolvus rates at about 20 percent of subsolvus rates for a given temperature. Linear regression equations modeling dwell crack growth rates at maximum stress intensities of 25 ksi*in$^{0.5}$ versus temperature are included in these figures, for use in estimating mean crack growth responses as a function of temperature. Dwell crack growth rates increased about 10x when increasing temperature from 1200 to 1300 °F. The test results are tabulated in appendix 13.

The cracking modes observed in cyclic fatigue crack growth tests of supersolvus specimens are compared for various temperatures in figure 34. Supersolvus cyclic crack growth specimens had predominantly transgranular cracking at all test temperatures. While the proportion of transgranular cracking was essentially 100 percent at 75 °F, a small percentage of intergranular cracking became apparent at temperatures of 1200 °F (about 5 percent) and 1300 °F (about 10 percent). Specimens tested from 75 to 1200 °F displayed planar cracking of some individual grains by facet failure, possibly related to concentrated slip on crystallographic planes as for the low cycle fatigue specimens. At higher temperatures a more textured fracture morphology was observed which was more nearly Mode 2.

Supersolvus specimens tested in dwell crack growth had predominantly intergranular cracking at the temperatures tested, figure 35. The intergranular cracking mode was mixed with minor transgranular cracking in tests at 1200 °F. The exposed crack growth surfaces were relatively flat, with little secondary cracking. However, the intergranular failure became highly prevalent in tests at 1300 °F, with considerable secondary grain boundary cracks obvious. A metallographic section of the crack growth region was prepared parallel to the loading axis to determine the extent of secondary cracking. As shown in figure 36, the secondary cracks extended down at least one layer of grains.

The cracking modes observed in cyclic fatigue crack growth tests of subsolvus specimens are compared for various temperatures in figure 37. Subsolvus cyclic crack growth specimens had predominantly transgranular cracking in tests at 75 to 800 °F. A much larger percentage of intergranular cracking became apparent than for supersolvus material at temperatures of 1200 °F (about 25 percent) and 1300 °F (about 60 percent). A significant number of secondary intergranular cracks were also observed at these higher test temperatures.

Subsolvus specimens tested in dwell crack growth had predominantly intergranular cracking at 1200 and 1300 °F, figure 38. The intergranular failure was highly prevalent in tests at both 1200 and 1300 °F, with considerable secondary grain boundary cracks obvious. A metallographic section of the crack growth region was prepared parallel to the loading axis to determine the extent of secondary cracking. As shown in figure 39, the secondary cracks extended down several layers of grains.

The crack growth results are in general agreement with previous findings on powder metallurgy disk superalloys. The effects of dwells in accelerating fatigue crack growth have been observed in Rene 95 (ref. 16), Udimet 720 (refs. 8 and 17), and ME3 (ref. 11). Coarser grain microstructures also have been shown superior for dwell fatigue crack growth (refs. 8, 16, and 17).

Additional Evaluations of LSHR

Several additional investigations of this alloy are currently underway, based on the results of these evaluations of scaled-up disks. The effects of cooling rate and aging heat treatments on tensile, creep, stress relaxation, dwell fatigue crack growth, and dwell notched fatigue properties at 1300 °F are being evaluated. Results have indicated that these properties are strongly influenced by varying solution heat treatment cooling rate as well as aging heat treatments. Different balances among these properties are thereby possible with this alloy, including much higher tensile ductility at high temperatures. Advanced dual microstructure heat treatments (DMHT) have also been applied to LSHR. The low solvus temperature of this alloy combined with its high refractory element levels allow very attractive

combinations of properties to be easily attained, giving high strength and fatigue resistance in the fine grain bore, and high creep and dwell crack growth resistance in the coarse grain rim (ref. 18). This advanced solution heat treatment is now being used with subsequent "supercooling" i.e., computer-controlled air quenching technology which carefully controls cooling rate as a function of location on a disk. This control of grain size and cooling rate can be combined with optimal aging heat treatments to produce highly favorable balances of mechanical properties at key disk locations (ref. 19).

Summary and Conclusions

Scaled-up LSHR disks were processed, sectioned, machined into specimens, and mechanically tested. The measured mechanical properties closely matched those previously determined from subscale disks. The mechanical properties of LSHR can be summarized as follows:

1) Tensile: Scaled-up LSHR had stable tensile strength and ductility to at least 1200 °F with a coarse grain, supersolvus heat treatment, and 1100 °F with fine grain, subsolvus heat treatment. Strength and ductility then gradually decreased with increasing temperature at higher temperatures. Ductility at high temperatures decreased with increasing cooling rate. Strength values usually exceeded those reported for ME3 and Udimet 720. Microvoid coalescence within grains produced failure at 75 to 1300 °F, but surface cracking interceded at 1300 to 1500 °F.
2) Creep: Supersolvus and subsolvus LSHR had comparable creep resistances at 1200 to 1300 °F, sustaining stresses of up to 100ksi with 0.2 percent creep lives of at least 100 h. At 1400 °F and 1500 °F, this applied stress dropped drastically to about 75 ksi and 50 ksi, respectively. This creep response exceeded those reported for ME3 and Udimet 720. Creep response could be modeled versus temperature and stress using a Larson-Miller Parameter approach, where a Larson Miller constant of 28 worked reasonably well for 0.2 percent creep and constant of 20 for creep rupture. Surface cracking limited rupture life at all test temperatures.
3) Low cycle fatigue: At strain ranges of 0.7 percent or less typically encountered in applications, LSHR had good LCF resistance at both 800 and 1300 °F. However, at higher strain ranges, life decreased at 1300 °F compared to 800 °F due to lower strength. Fatigue life response of LSHR was comparable to that reported for ME3 and Udimet 720 at equivalent grain sizes. Crystallographic slip failures of large grains usually initiated failure in supersolvus material in tests at both 800 and 1300 °F. However, at 1300 °F and high strain ranges failures were often produced by crack initiation modes at surface oxidation. Failures of subsolvus material were often initiated by inclusions at both temperatures, though several failures were also initiated by grain facets or pores at 800 °F. Limited tests of notched specimens indicated dwells at maximum stresses significantly degrade fatigue resistance at 1300 °F.
4) Crack growth: Cyclic crack growth rates only increased by 10X between 75 and 1300 °F. However, dwell crack growth rates were significantly higher than cyclic rates and increased much more strongly with temperature from 1200 to 1300 °F, by about 10X. Supersolvus material consistently had lower cyclic and dwell crack growth rates than subsolvus material. Crack growth response of LSHR was typical of that reported for ME3 and Udimet 720 at equivalent grain sizes. Dwells at maximum stress promoted intergranular crack growth for both materials.

It can be concluded from this evaluation that LSHR should have at least 1300 °F general capabilities. Subsolvus, fine grain material could be preferred for superior strength, fatigue, and creep resistance at temperatures up to 1200 °F. Supersolvus, coarse grain material should be selected for superior creep and dwell crack growth resistance at higher temperatures. In both cases, LSHR appears to have improved strength and creep resistance over many existing powder metallurgy disk superalloys. More detailed

assessments of mechanical properties versus component design needs would be necessary to determine specific temperature limits for specific potential applications.

References

1. T.P. Gabb, J. Gayda, J. Telesman, P.T. Kantzos, W.A. Konkel, "Realistic Subscale Evaluations of the Mechanical Properties of Advanced Disk Superalloys," NASA/TM—2003-212086, NASA, Washington, D.C., Jan. 2003.
2. R.H. Vanstone, T.L. Richardson, "Potential-Drop Monitoring of Cracks in Surface-Flawed Specimens," ASTM STP 877, American Society for Testing and Materials, West Conshohocken, PA, 1985, pp. 148–166.
3. R.A. Ricks, A.J. Porter, R.C. Ecob, "The Growth of γ′ Precipitates in Nickel-base Superalloys," Acta Met., vol. 31, 1983, pp. 80–81.
4. T.P. Gabb, A. Garg, D.L., Ellis, K.M. O'Connor, "Detailed Microstructural Characterization of the Disk Alloy ME3," NASA/TM—2004-213066, NASA, Washington, D.C., May 2004.
5. O.H. Kriege, J.M. Baris, "The Chemical Partitioning of Elements in Gamma Prime Separated From Precipitation-Hardened, High-Temperature Nickel-Base Alloys," Trans. ASM, vol. 62, 1969, pp. 195–200.
6. T.P. Gabb, A. Garg, D.L. Ellis, "Microstructural Evaluations of Baseline HSR/EPM Disk Alloys", NASA/TM—2004-213123, Washington, D.C., August 2004.
7. C.T. Sims, N.S. Stoloff, W.C. Hagel, Superalloys II, John Wiley & Sons, New York, NY, 1987, pp. 583–585.
8. K.A. Green, J.A. Lemsky, R.M. Gasior, "Development of Isothermally Forged P/M Udimet 720 for Turbine Disk Applications," Superalloys 1996, ed. R.D. Kissinger, K.J. Deye, D.L. Anton, A.D. Cetel, M.V. Nathal, T.M. Pollock, D.A. Woodford, The Minerals, Metals, & Materials Society, Warrendale, PA, 1996, pp. 697–704.
9. H. Hattori, M. Takekawa, D. Furrer, R.J. Noel, "Evaluation of P/M U720 for Gas Turbine Engine Disk Application", Superalloys 1996, ed. R.D. Kissinger, K.J. Deye, D.L. Anton, A.D. Cetel, M.V. Nathal, T.M. Pollock, D.A. Woodford, The Minerals, Metals, & Materials Society, Warrendale, PA, 1996, pp. 705–711.
10. Banik, K.A. Green, "The Mechanical Property Response of Turbine Disks Produced Using Advanced PM Processing Techniques," Superalloys 2000, Ed. T.M. Pollock, R.D. Kissinger, R.R. Bowman, K.A. Green, M. McLean, S. Olson, J.J. Schirra, The Minerals, Metals & Materials Society, Warrendale, PA, 2000, pp. 69–74.
11. T.P. Gabb, J. Telesman, P.T. Kantzos, K. O'Connor, "Characterization of the Temperature Capabilities of Advanced Disk Alloy ME3," NASA/TM—2002-211796, NASA, Washington, D.C., August 2002.
12. K.N. Smith, P. Watson, T.H. Topper, "A Stress-Strain Function for the Fatigue of Metals," Journal of Metals, vol. 5, no. 4, 1970, pp. 767–778.
13. T.P. Gabb, J. Gayda, J. Sweeney, "The Effect of Boron on the Low Cycle Fatigue Behavior of Disk Alloy KM4," NASA/TM—2000-210458, NASA, Washington, D.C., 2000.
14. D.R. Chang, D.D. Krueger, R. A. Sprague, "Superalloy Powder Processing, Properties, and Turbine Disk Applications", Superalloys 1984, ed. M. Gell, C.S. Kortovich, R.H. Bricknell, W.B. Kent, J.F. Radavich, The Minerals, Metals & Materials Society, Warrendale, PA, 1984, pp. 245–252.
15. E.S. Huron, P.G. Roth, "The Influence of Inclusions on Low Cycle Fatigue Life in a P/M Nickel-Base Disk Superalloy", Superalloys 1996, ed. R.D. Kissinger, K.J. Deye, D.L. Anton, A.D. Cetel, M.V. Nathal, T.M. Pollock, D.A. Woodford, The Minerals, Metals, & Materials Society, Warrendale, PA, 1996, pp. 359–367.

16. J. Gayda, T P. Gabb, R.V. Miner, “Fatigue Crack Propagation of Nickel-Base Superalloys at 650 °C,” Low Cycle Fatigue, ASTM STP 942, ed. H.D. Solomon, G.R. Halford, L.R. Kais, and B.N. Leis, American Society for Testing and Materials, Philadelphia, PA, 1988, pp. 293–309.
17. K.R. Bain, M.L. Gambone, J.M. Hyzak, M.C. Thomas, “Development of Damage Tolerant Microstructures in Udimet 720,” Superalloys 1988, ed. S. Reichman, D.N. Duhl, G. Maurer, S. Antolovich, C. Lund, The Minerals, Metals & Materials Society, Warrendale, PA, 1988, pp. 13–22.
18. J. Gayda, T.P. Gabb, P.T. Kantzos, “The Effect of Dual Microstructure Heat Treatment on an Advanced Nickel Base Disk Alloy,” Superalloys 2004, ed. K.A. Green, T.M. Pollock, H. Harada, T.E. Howson, R.C. Reed, J.J. Schirra, S. Walston, The Minerals, Metals & Materials Society, Warrendale, PA, 2004, pp. 323–329.
19. J. Gayda, D.U. Furrer, “Dual Microstructure Heat Treatment,” Advanced Materials & Processes, July, 2003, pp. 36–39.

Table 1.—Measured composition in weight percent of LSHR alloy disks, and measured compositions of extracted γ′ and γ phases.

Wt%	Al	B	C	Co	Cr	Fe	Mo	Nb	Ta	Ti	W	Zr	Ni
LSHR Composition	**3.46**	**0.028**	**0.029**	**20.7**	**12.52**	**0.07**	**2.73**	**1.45**	**1.6**	**3.5**	**4.33**	**0.049**	**49.534**
γ′ phase	5.48			12.27	1.99	0.02	1.1	2.49	3.02	6.36	3.59	0.094	63.586
γ phase	1.16	0.019		30.34	23.34	0.095	4.24	0.38	0.19	0.56	4.99	0.002	34.684
γ Partitioning Ratio	0.22			2.55	12.10	4.90	3.98	0.16	0.06	0.09	1.43	0.02	0.56
=(at. % γ)/(at. % γ′)													

Table 2. —Measured densities of supersolvus and subsolvus samples.

Sample	Dry weight	Wet weight	Buoyancy	Density	Density
	g	g		g/cc	lb/in^3
Subsolvus 1	8.2292	7.4363	0.7929	8.3589	0.3020
Subsolvus 2	8.1743	7.3862	0.7881	8.3537	0.3018
Subsolvus 3	8.5936	7.7653	0.8283	8.356	0.3019
Subsolvus 4	8.5236	7.7026	0.821	8.3616	0.3021
Subsolvus 5	7.9164	7.1536	0.7628	8.3585	0.3020
Supersolvus	4.0359	3.6481	0.3878	8.3819	0.3028
Supersolvus	4.0295	3.6399	0.3896	8.3300	0.3009
Supersolvus	4.0459	3.6563	0.3896	8.3639	0.3022
Supersolvus	4.0241	3.6364	0.3877	8.3596	0.3020
			MEAN	**8.358**	**0.3020**
			STDEV	**0.013**	**0.0005**

Table 3.—Shear and Young's modulus measurements at room temperature, with calculated Poisson's ratio.

	G-Shear Modulus			E-Young's Modulus	
Spec.	GPa	Msi	Spec.	GPa	Msi
A1-BL3	87.97	12.76	T7-2-M1	224.95	32.62
A1-WL1	87.55	12.70	T7-2-M1	228.25	33.10
B1-BL3	88.30	12.81	T7-2-M2	224.85	32.61
B1-RL2	87.21	12.65	T7-2-M2	226.96	32.92
Mean	**87.76**	**12.73**	T7-2-M3	222.56	32.28
StDev	**0.48**	**0.07**	T7-2-M3	226.22	32.81
			T7-2-M4	224.75	32.60
Poisson's Ratio			T7-2-M4	227.17	32.95
=E/(2G)-1			**Mean**	**225.71**	**32.74**
0.286			**StDev**	**1.80**	**0.26**

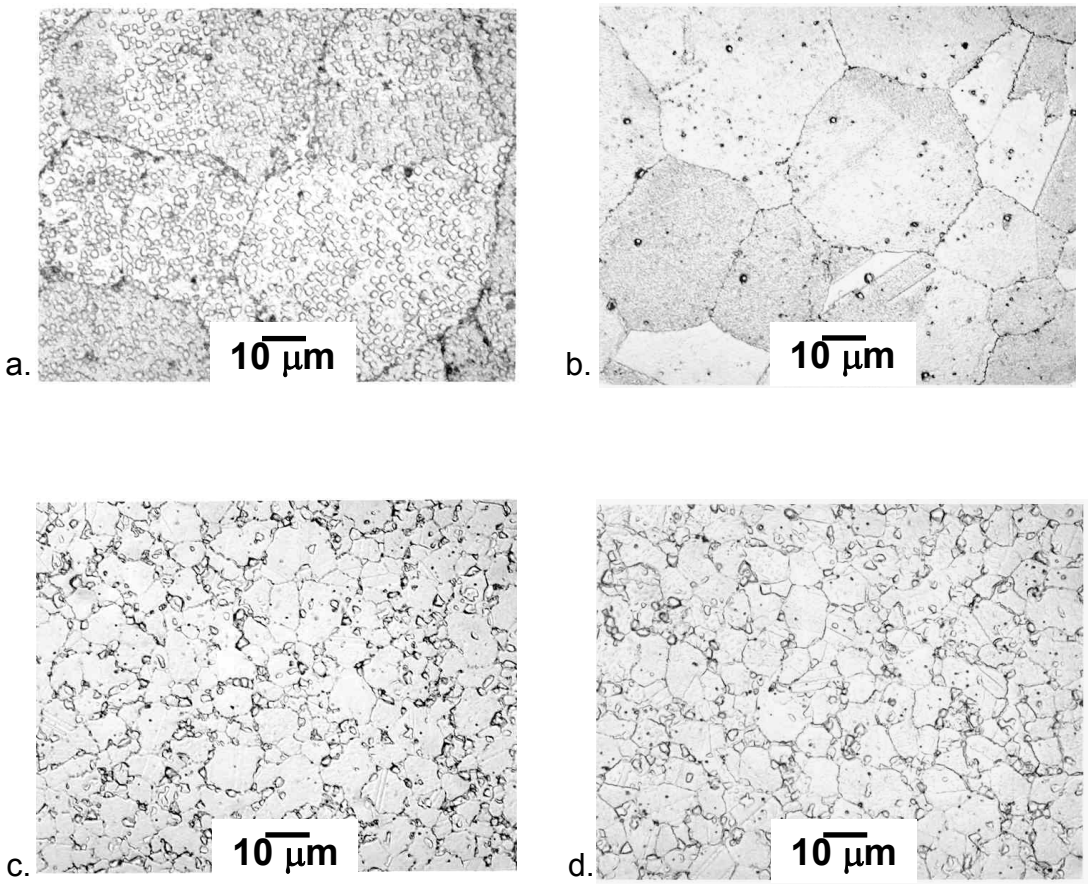

Figure 1.—Optical micrographs of supersolvus and subsolvus disk grain microstructures: a. supersolvus bore, b. supersolvus rim, c. subsolvus bore, d. subsolvus rim.

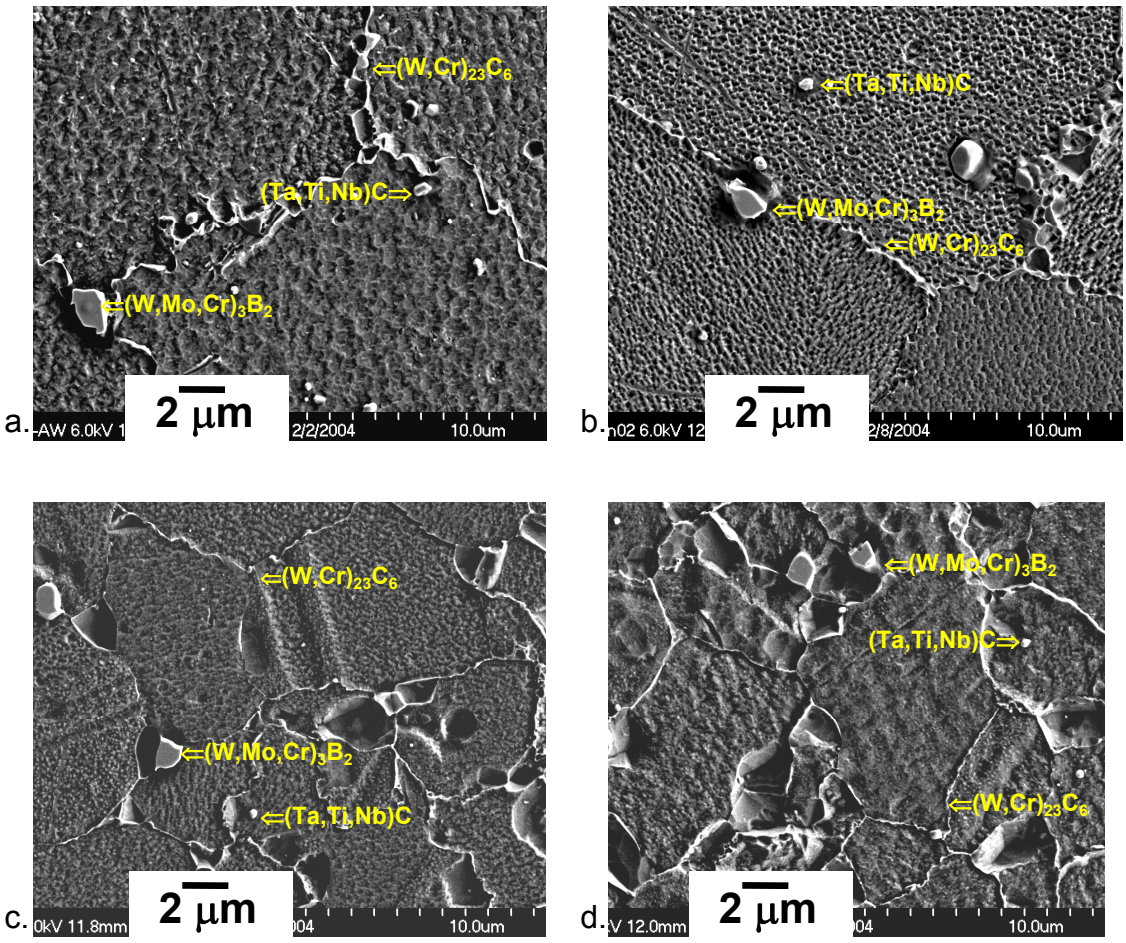

Figure 2.—FESEM micrographs of supersolvus and subsolvus disk microstructures, showing large $(W,Mo,Cr)_3B_2$, medium (Ta,Ti,Nb)C, and fine $(W,Cr)_{23}C_6$ carbides: a. supersolvus bore, b. supersolvus rim, c. subsolvus bore, d. subsolvus rim.

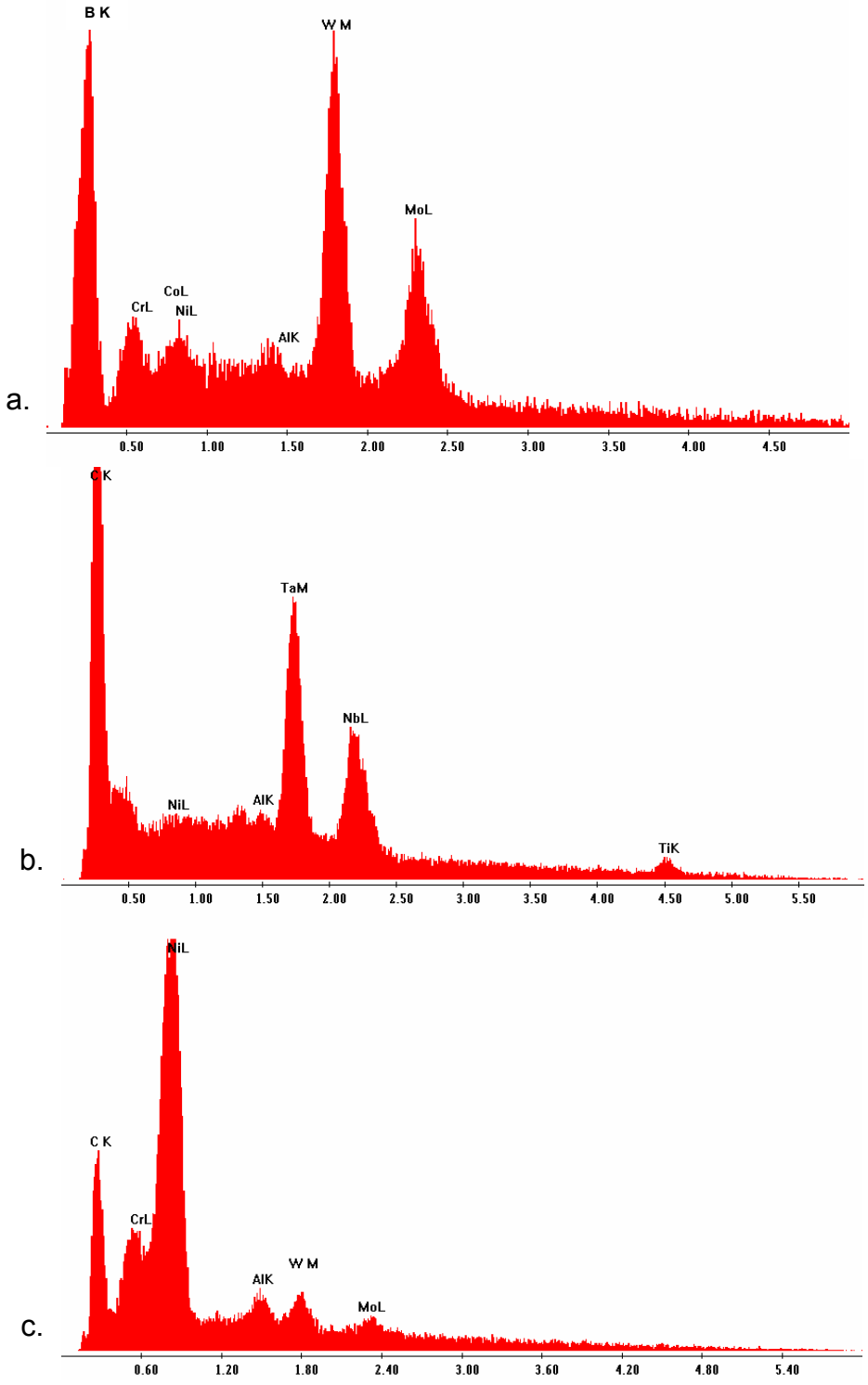

Figure 3.—Energy dispersive x-ray spectra showing carbides:
a. $(W,Mo,Cr)_3B_2$ b. (Ta,Nb,Ti)C, c. $(W,Cr)_{23}C_6$.

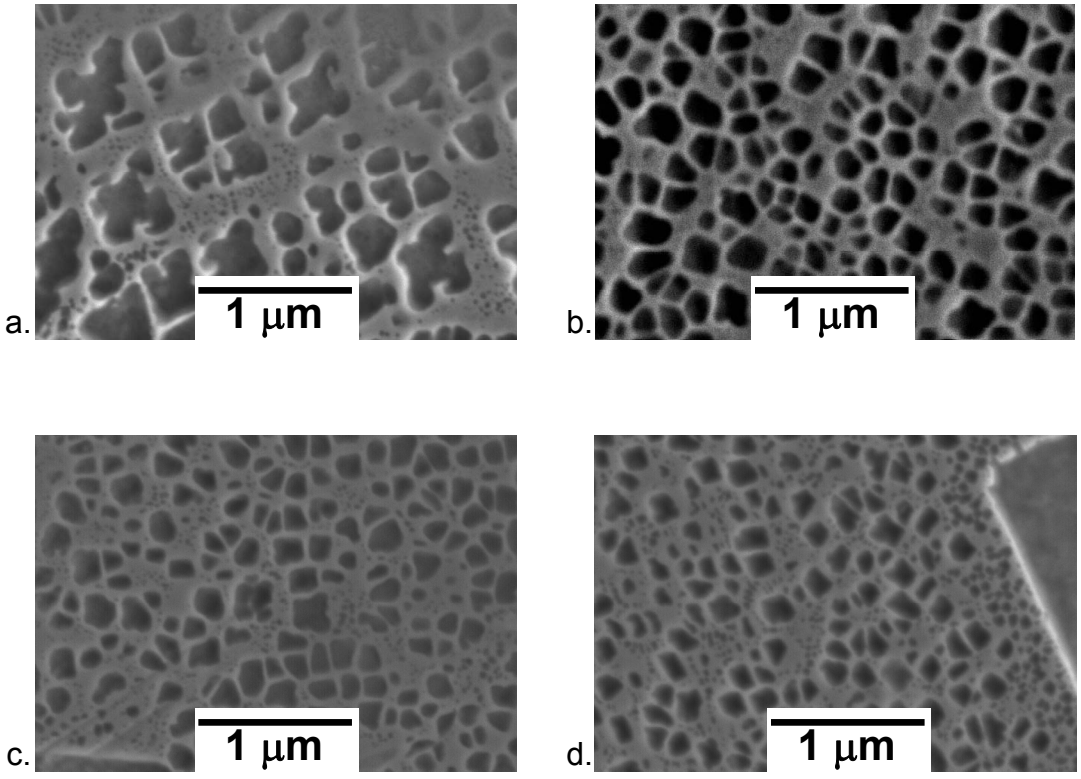

Figure 4.—FESEM micrographs of supersolvus and subsolvus disk γ′ microstructures: a. supersolvus bore, b. supersolvus rim, c. subsolvus bore, d. subsolvus rim.

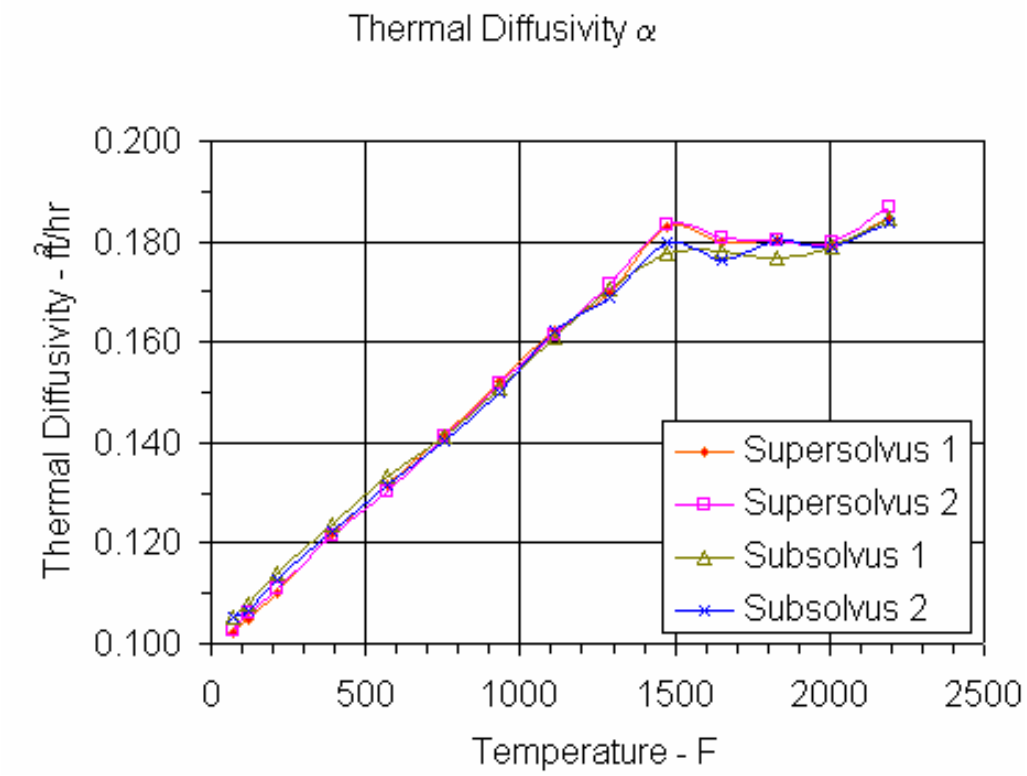

Figure 5.—Thermal diffusivity vs. temperature in supersolvus and subsolvus material.

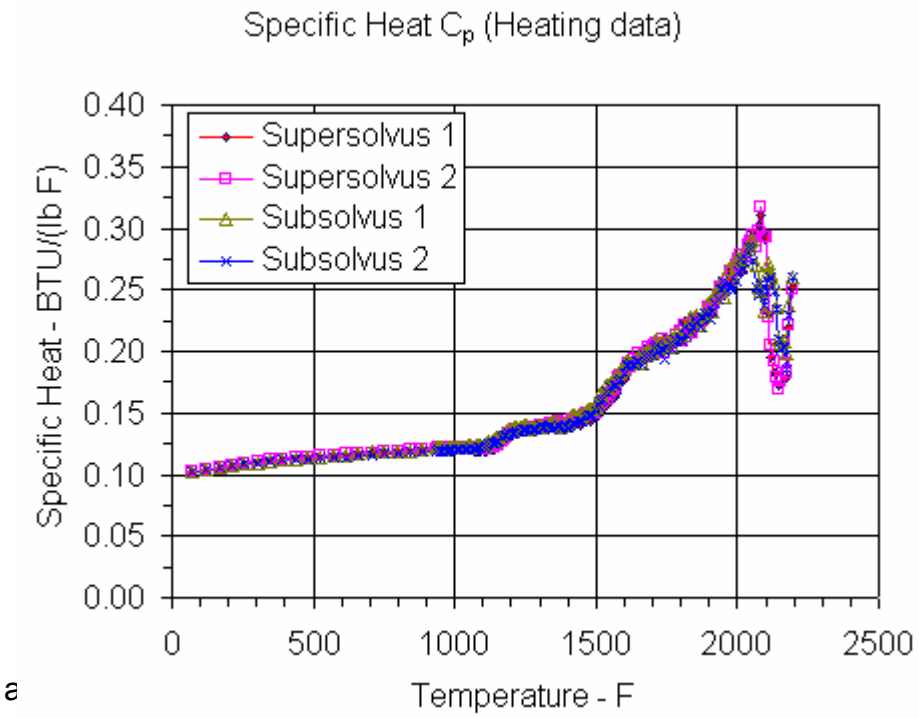

a

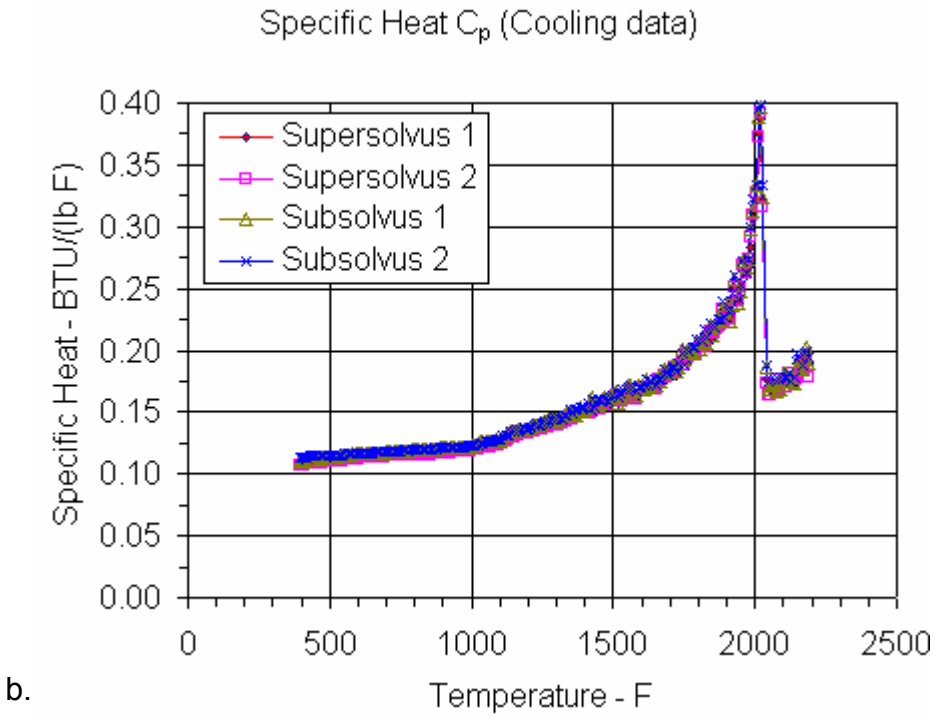

b.

Figure 6.—Specific heat vs. temperature of supersolvus and subsolvus material during a. heating and b. cooling.

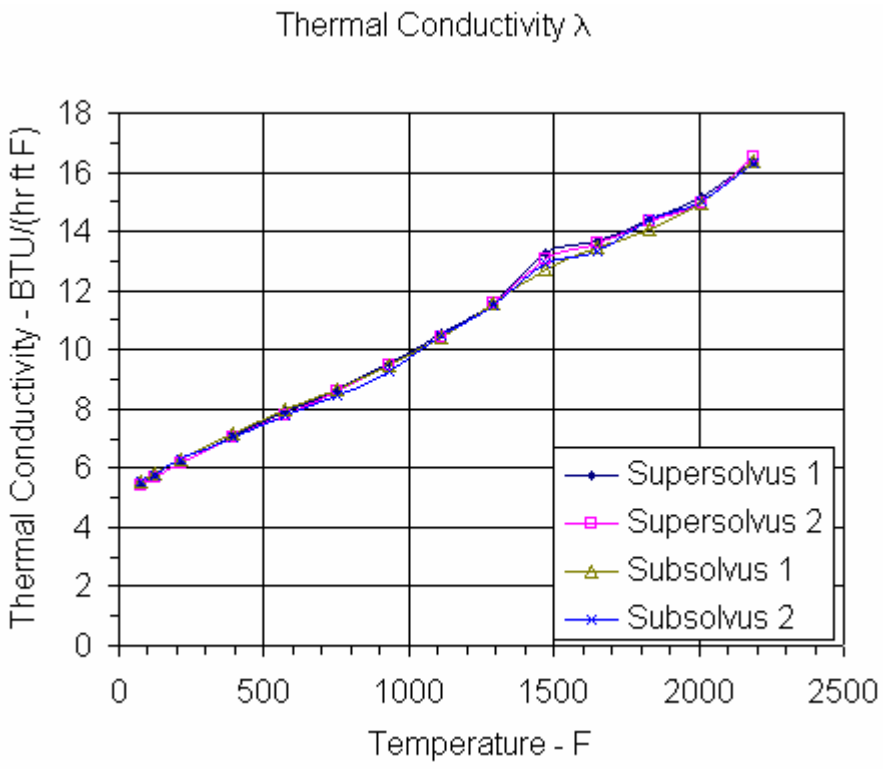

Figure 7.—Thermal conductivity vs. temperature of supersolvus and subsolvus material.

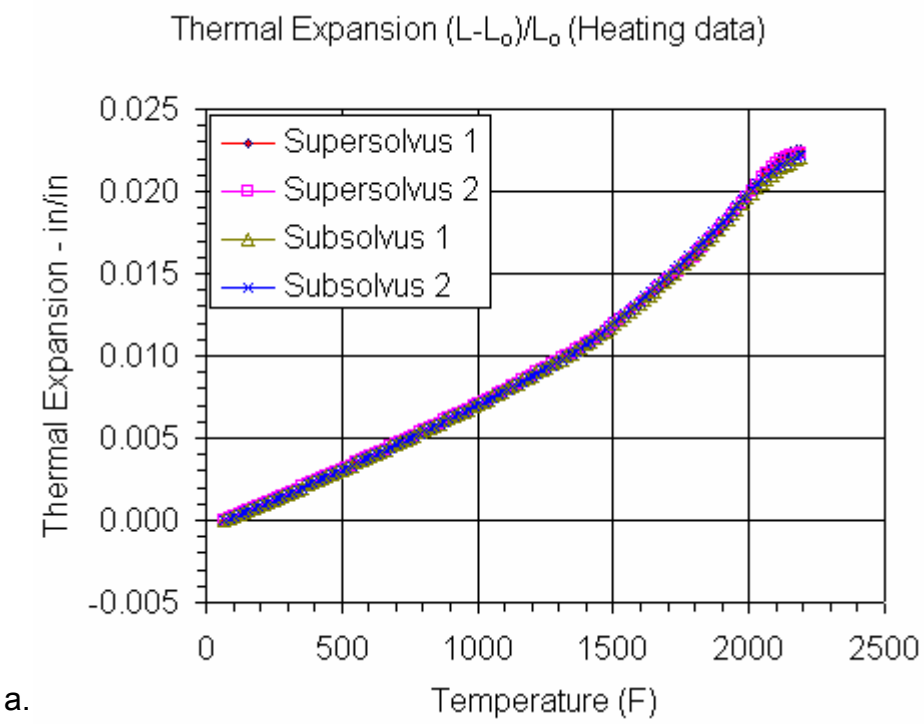

a.

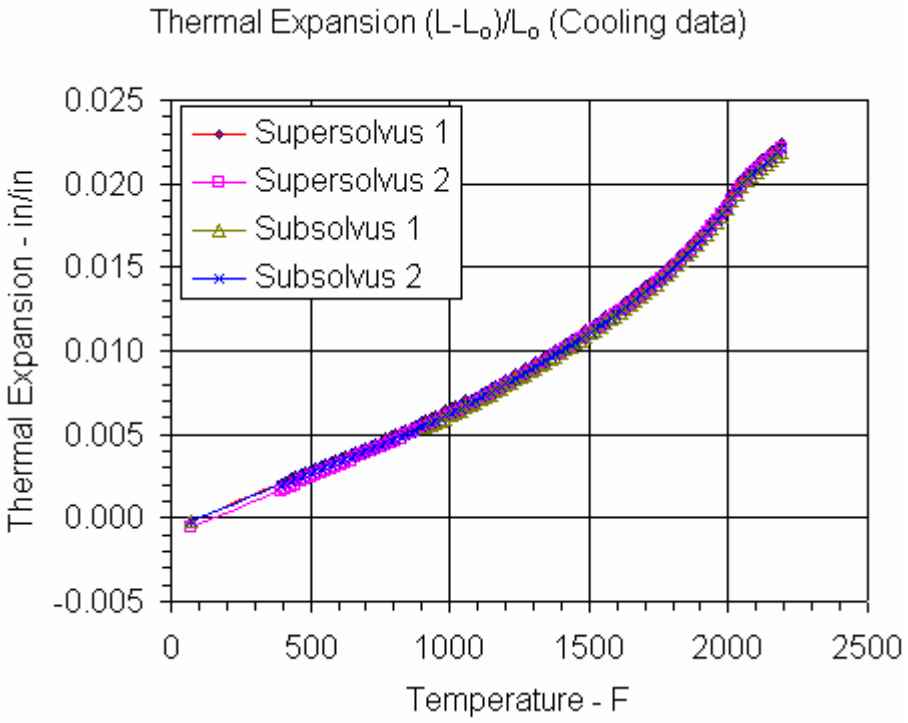

b.

Figure 8.—Thermal expansion vs. temperature of supersolvus and subsolvus material during a. heating and b. cooling.

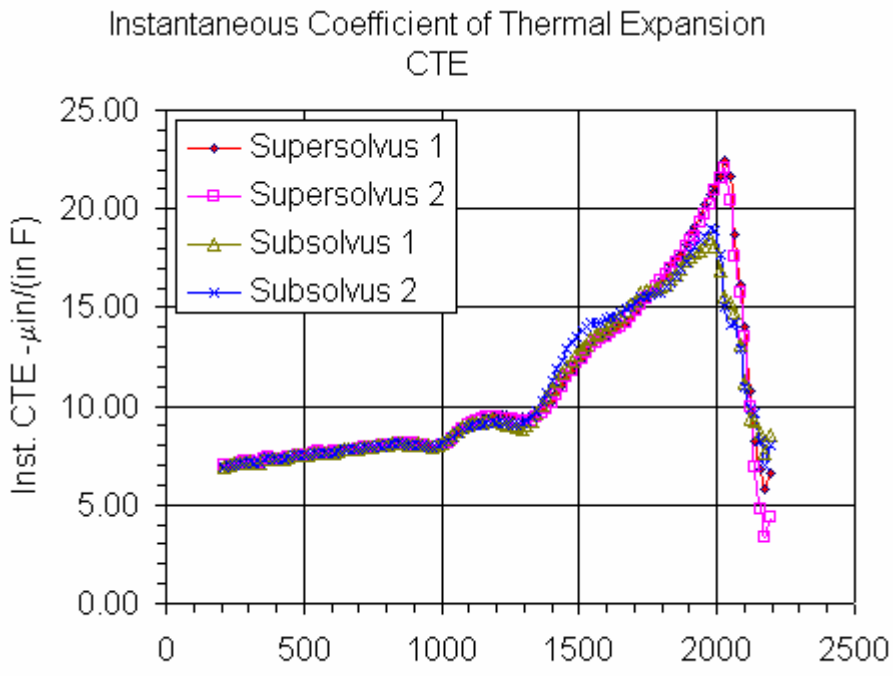

c

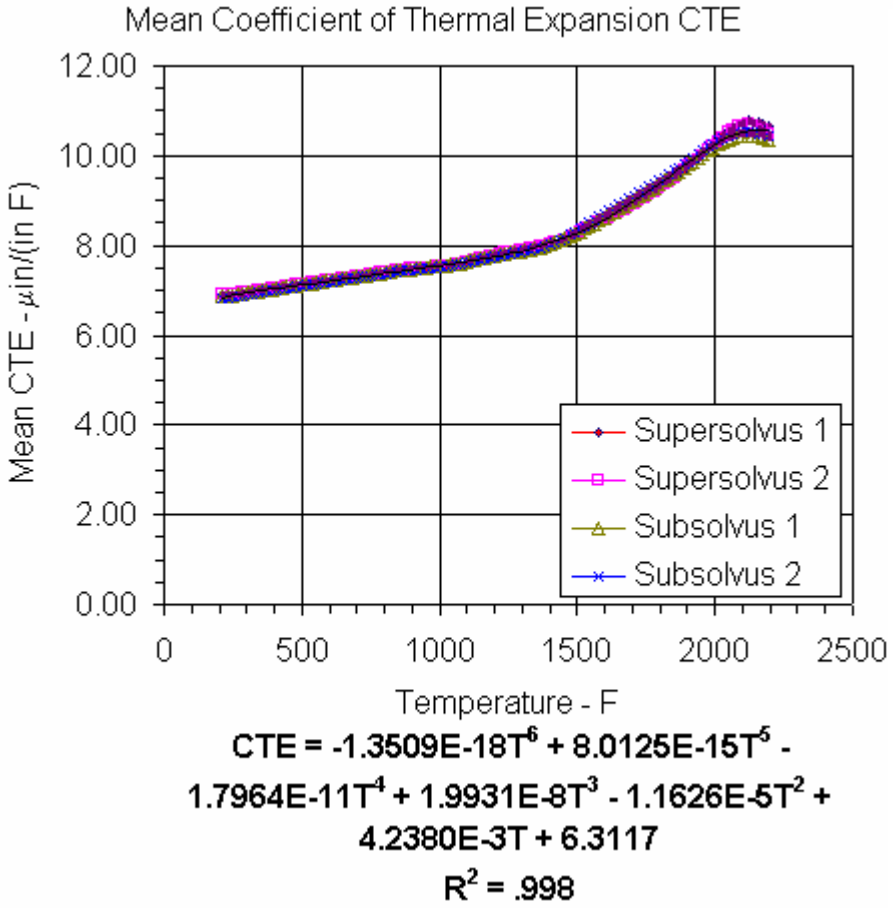

d.

Figure 8.—c. Instantaneous and d. mean coefficient of thermal expansion vs. temperature of supersolvus and subsolvus material.

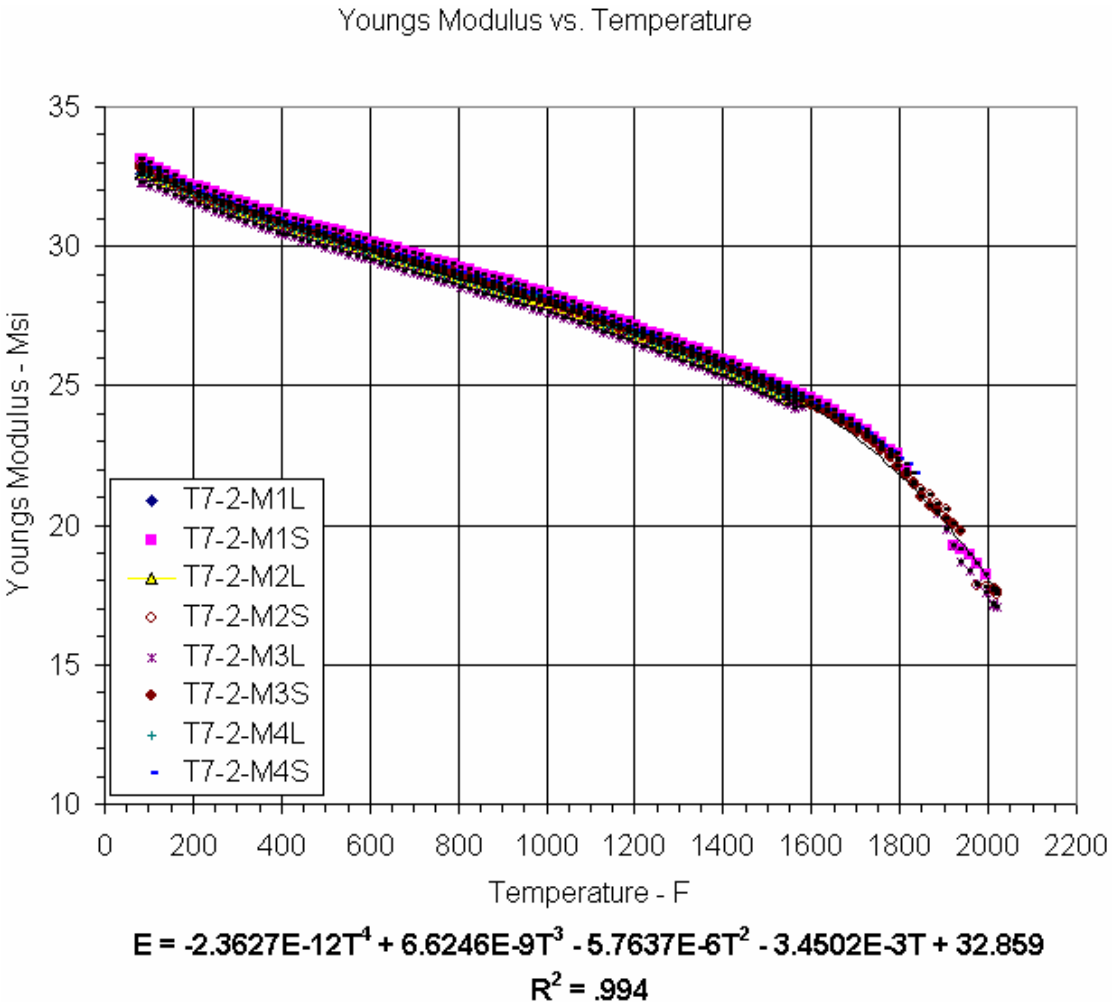

Figure 9.—Young's modulus vs. temperature for supersolvus material.

a.

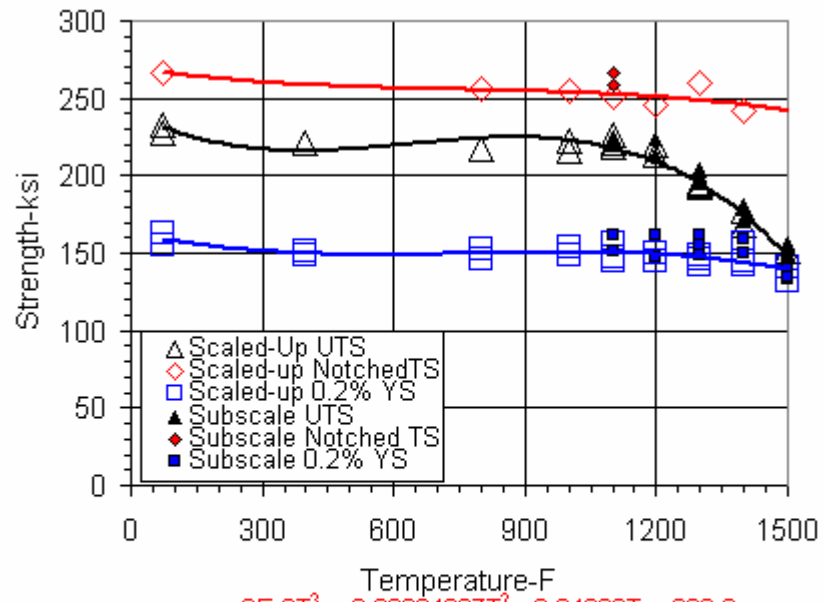

$\sigma_{NTS} = -2E\text{-}8T^3 + 0.00004837T^2 - 0.04322T + 269.6$

$R^2 = 0.617$

$\sigma_{UTS} = -1.5E\text{-}7T^3 + 0.00028240T^2 - 0.15316T + 241.7$

$R^2 = 0.948$

$\sigma_{YS} = -4E\text{-}8T^3 + 0.00008914T^2 - 0.06391T + 163.5$

$R^2 = 0.534$

b.

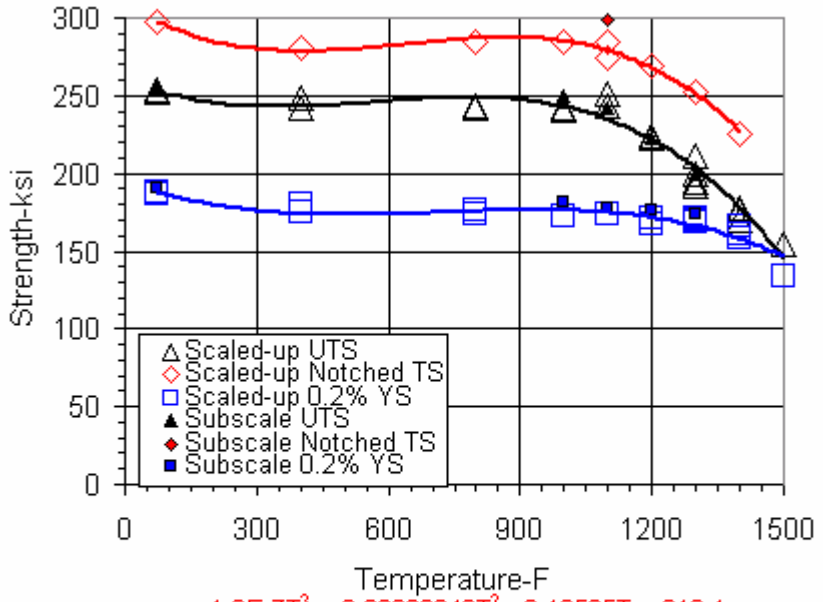

$\sigma_{NTS} = -1.8E\text{-}7T^3 + 0.00033642T^2 - 0.18535T + 310.1$

$R^2 = 0.983$

$\sigma_{UTS} = -1.5E\text{-}7T^3 + 0.00025161T^2 - 0.12165T + 260.8$

$R^2 = 0.954$

$\sigma_{YS} = -8.0E\text{-}8T^3 + 0.00016544T^2 - 0.10778T + 195.4$

$R^2 = 0.828$

Figure 10.—0.2 percent yield strength, ultimate strength, and notched tensile strength of a. supersolvus and b. subsolvus material.

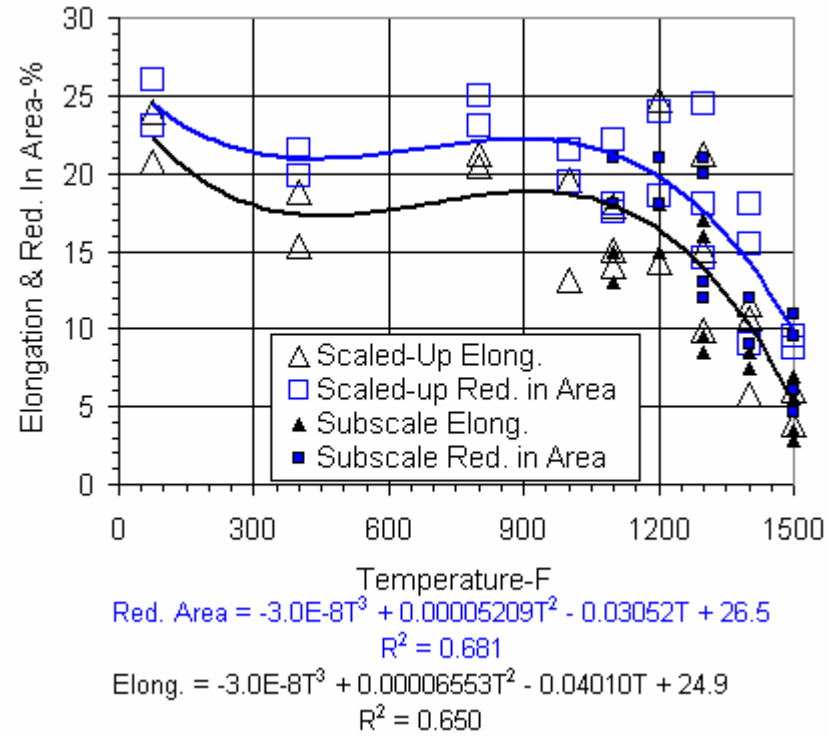

a.

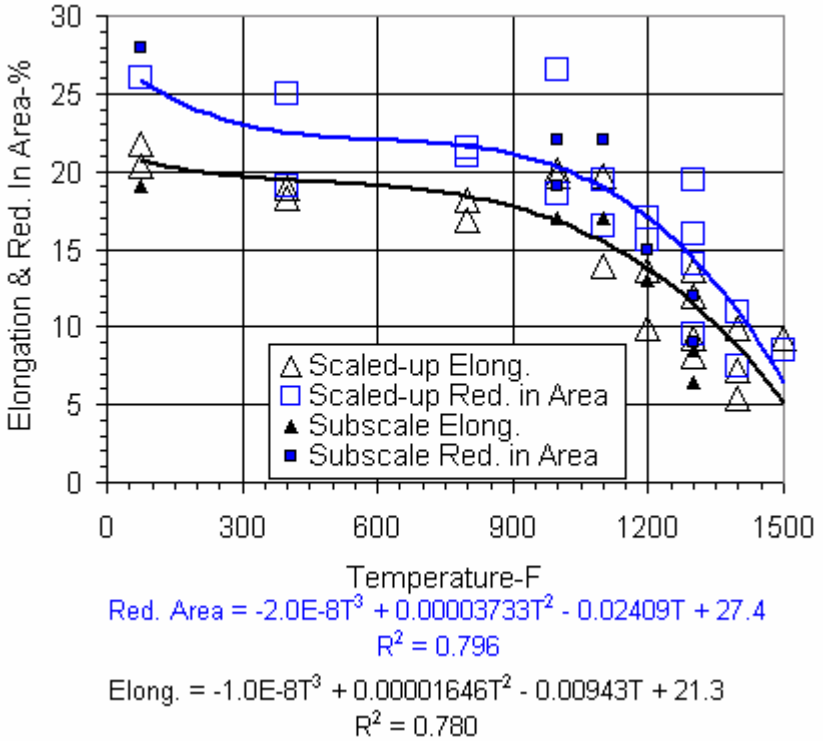

b.

Figure 11.—Elongation and reduction in area of tensile tests for a. supersolvus and b. subsolvus material.

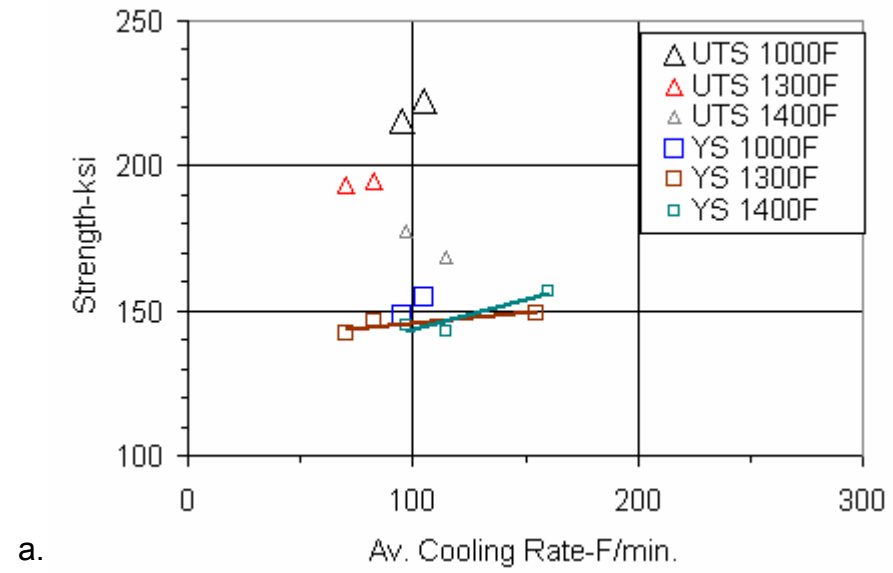

a.

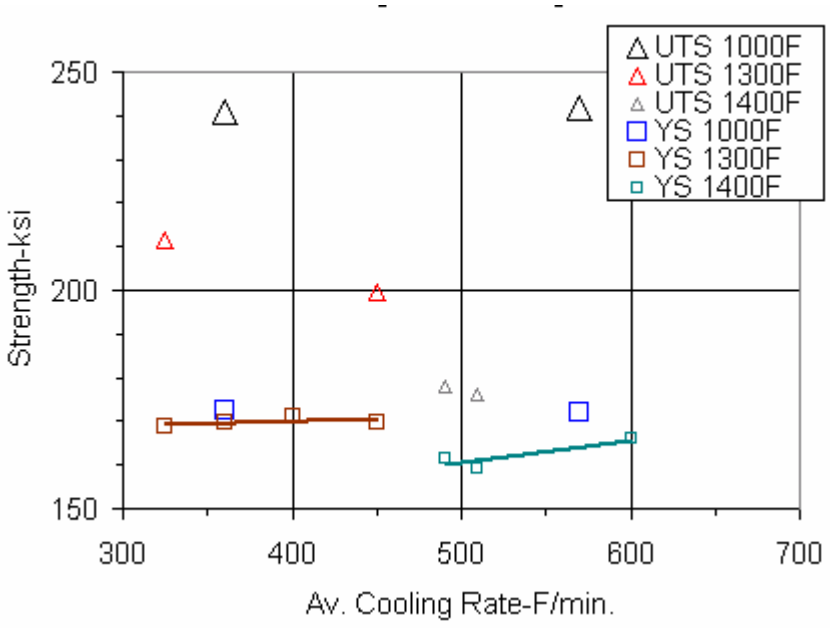

b.

Figure 12.—Yield and ultimate strengths vs. average cooling rate of tensile tests for a. supersolvus and b. subsolvus scaled-up material.

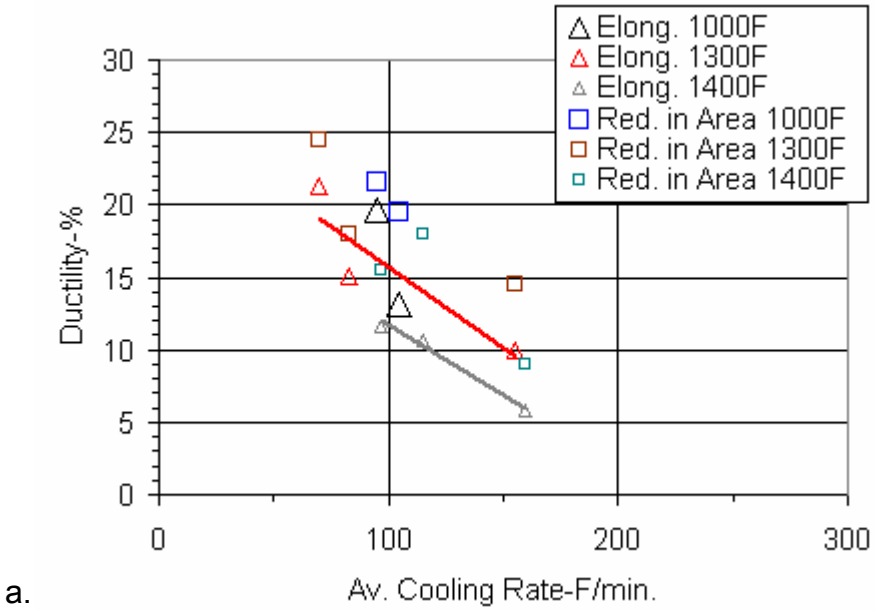

a.

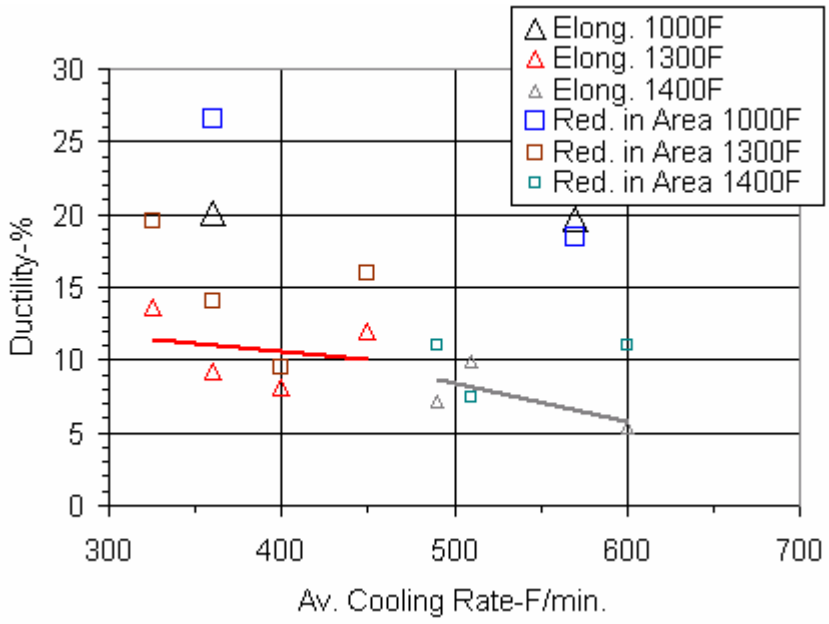

b.

Figure 13.—Elongation and reduction in area vs. average cooling rate of tensile tests for a. supersolvus and b. subsolvus scaled-up material.

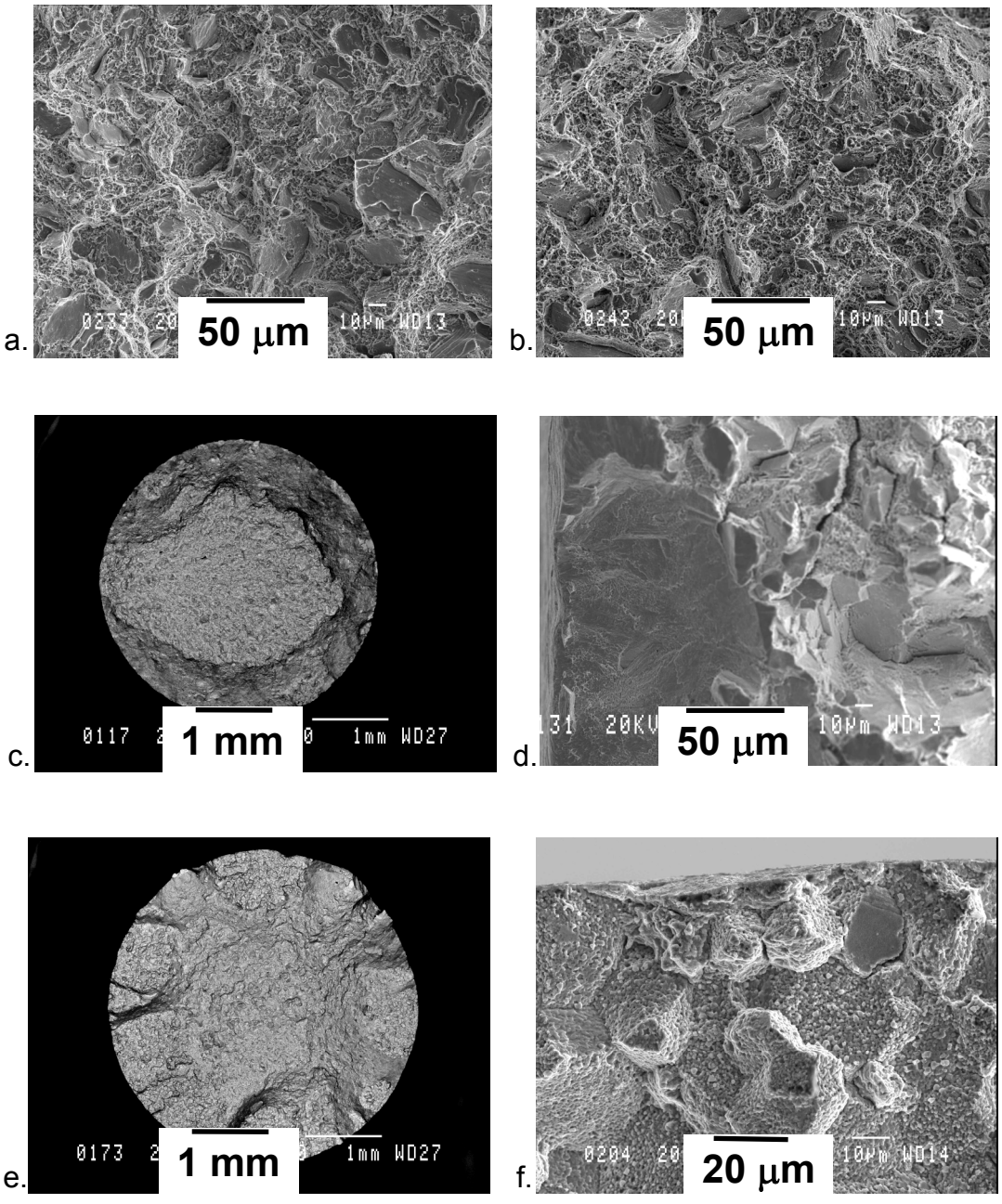

Figure 14.—Fracture surfaces observed for supersolvus tensile specimens tested at a. 75 °F, b. 800 °F, c. and d. 1300 °F, e. and f. 1500 °F.

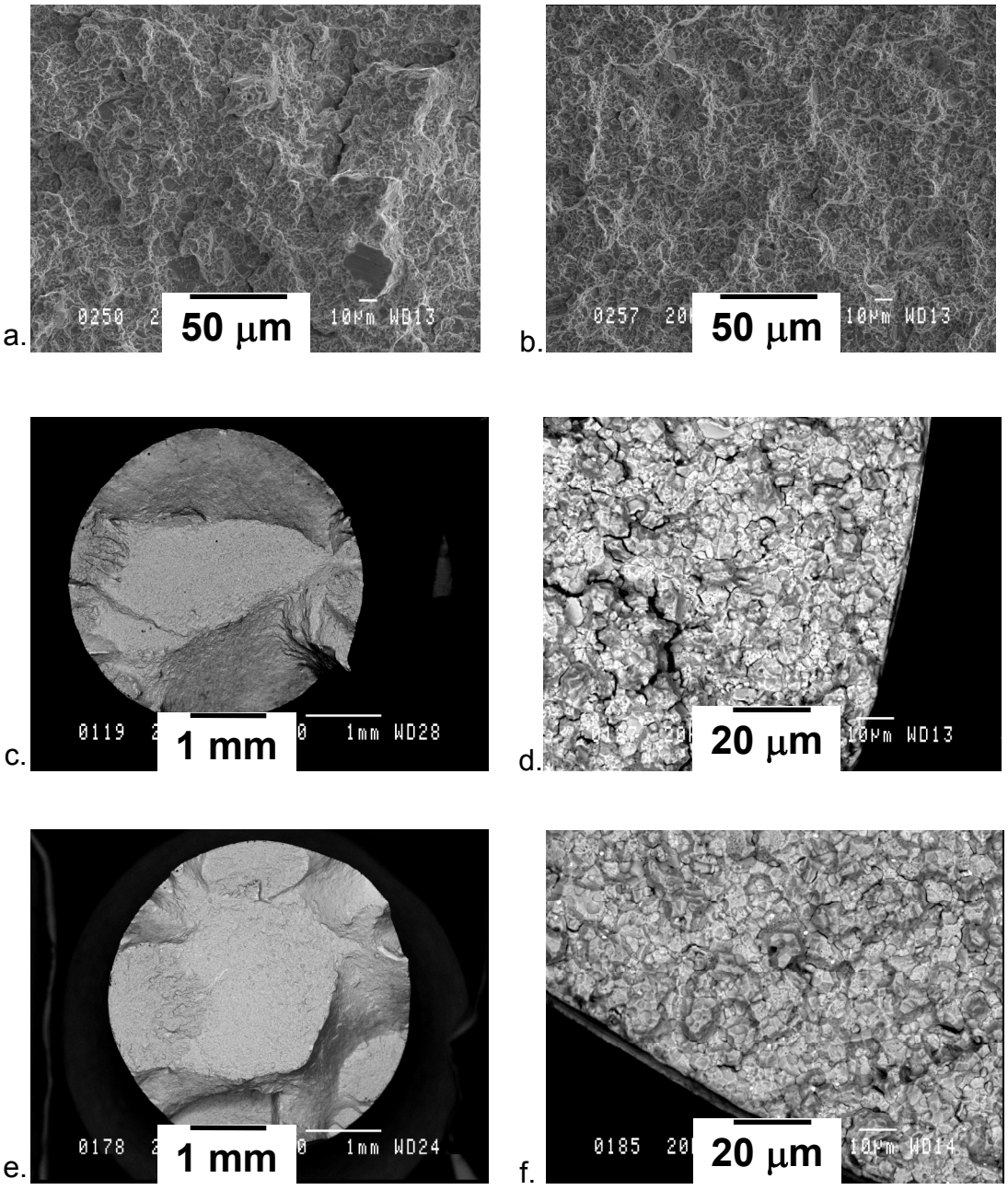

Figure 15.—Fracture surfaces observed for subsolvus tensile specimens tested at a. 75 °F, b. 800 F, c. and d. 1300 ° F, e. and f. 1500 °F.

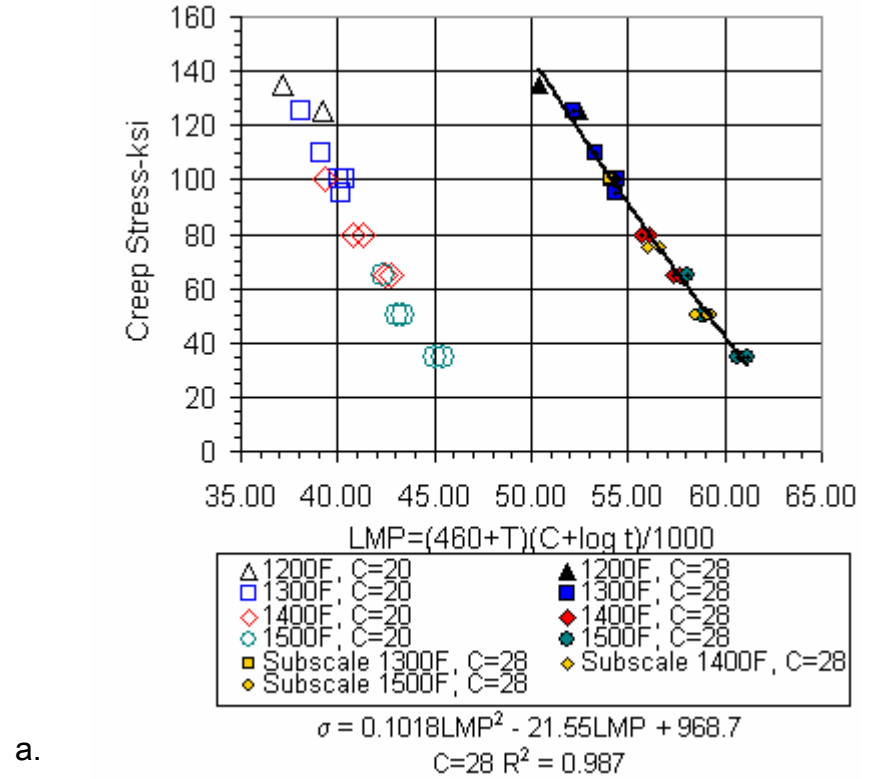

a.

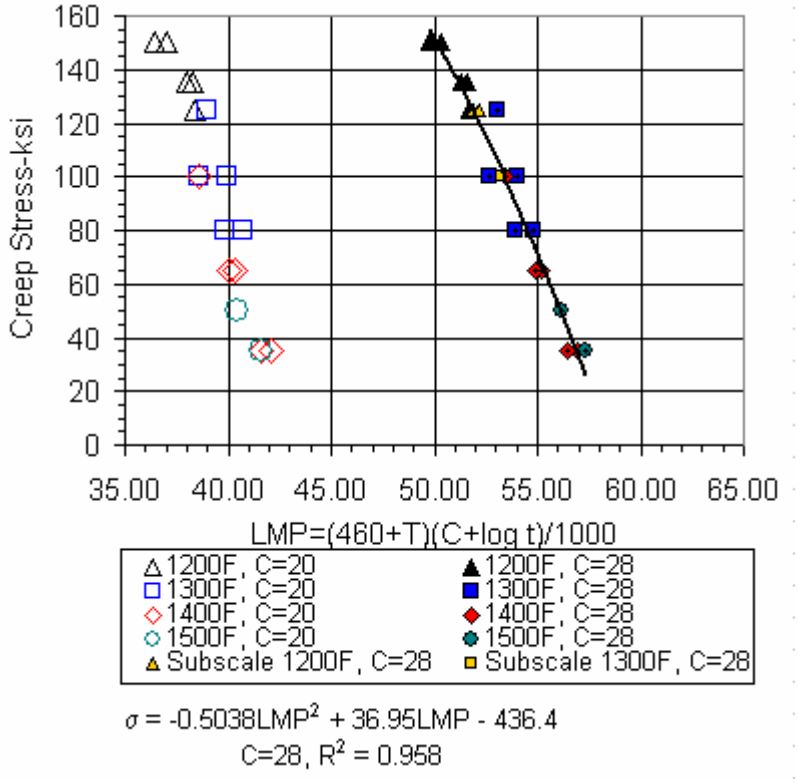

b.

Figure 16.—0.2% creep lives expressed using Larson-Miller parameters for a. supersolvus and b. subsolvus material.

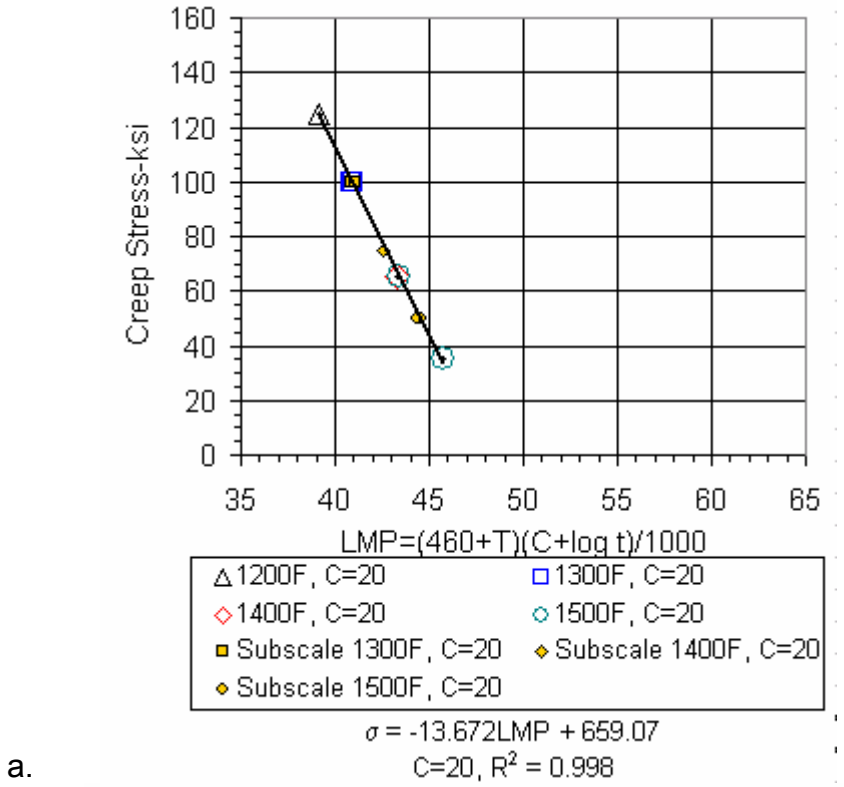

a.

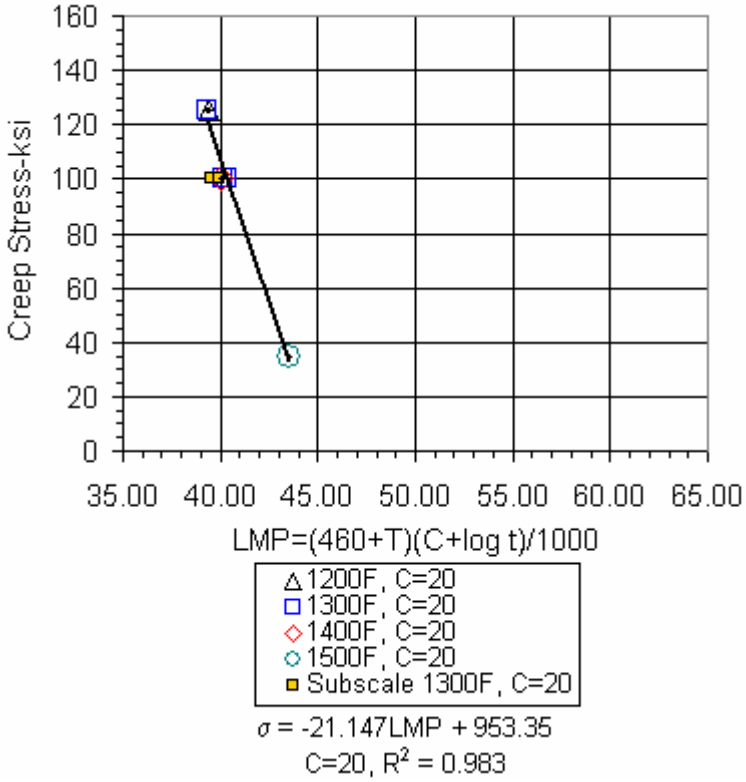

b.

Figure 17.—Rupture lives expressed using Larson-Miller parameters for a. supersolvus and b. subsolvus material.

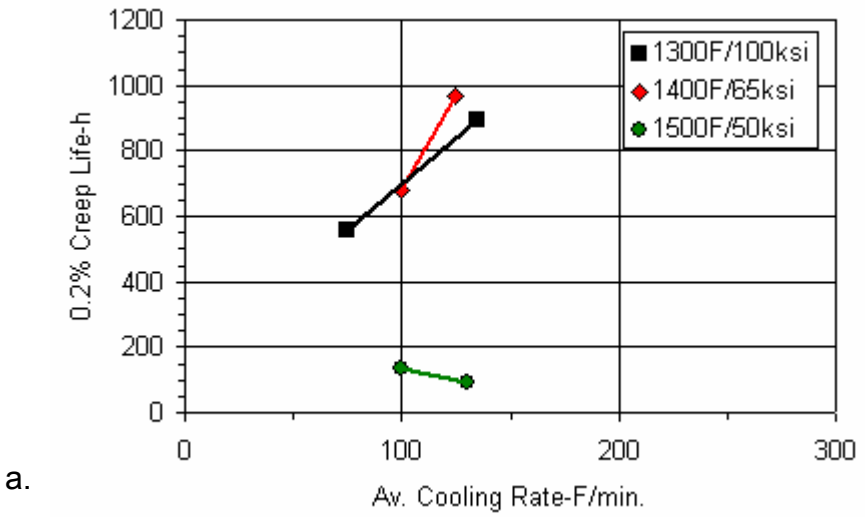

a.

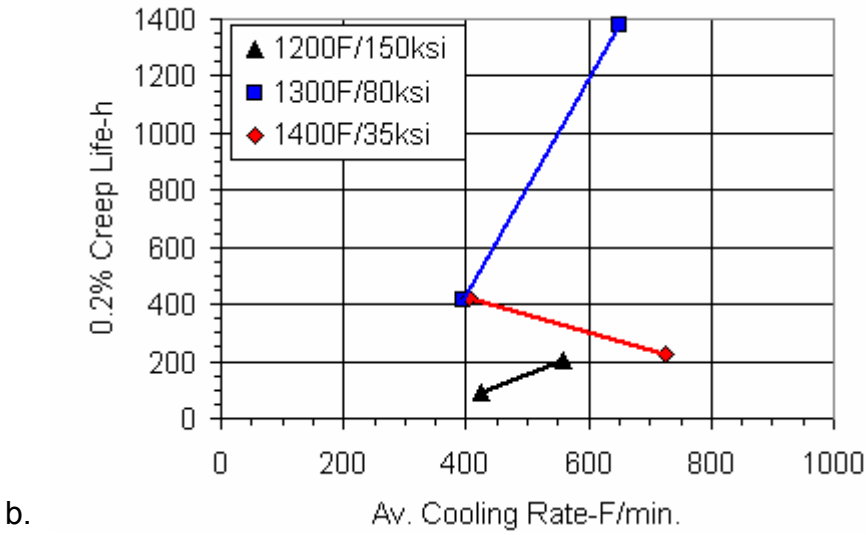

b.

Figure 18.—0.2% creep lives vs. average cooling rate for a. supersolvus and b. subsolvus material.

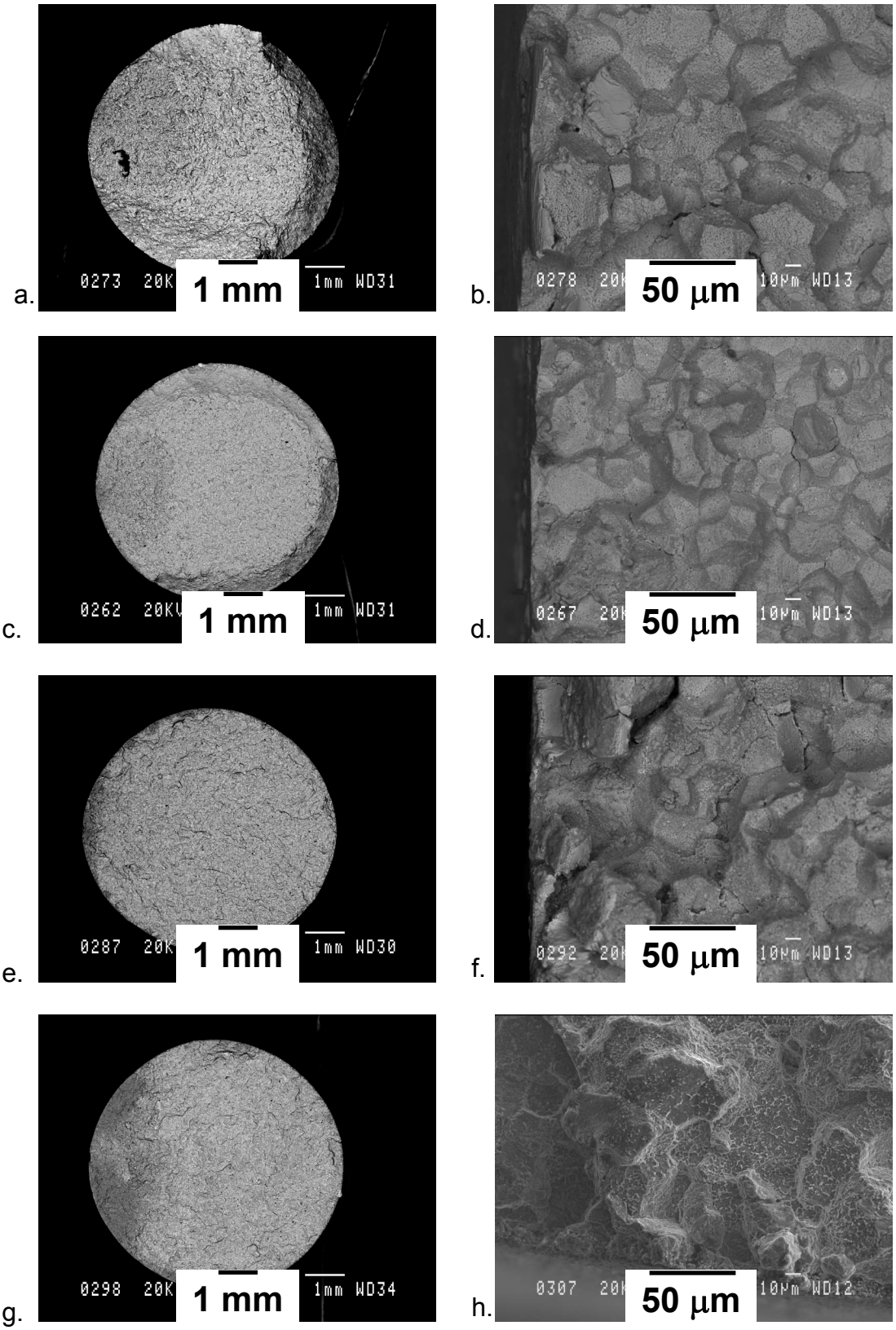

Figure 19.—Fracture surfaces observed for supersolvus creep specimens tested at a. and b. 1200 °F/125 ksi, c. and d. 1300 °F/100 ksi, e. and f. 1400 °F/65 ksi, g. and h. 1500 °F/50 ksi.

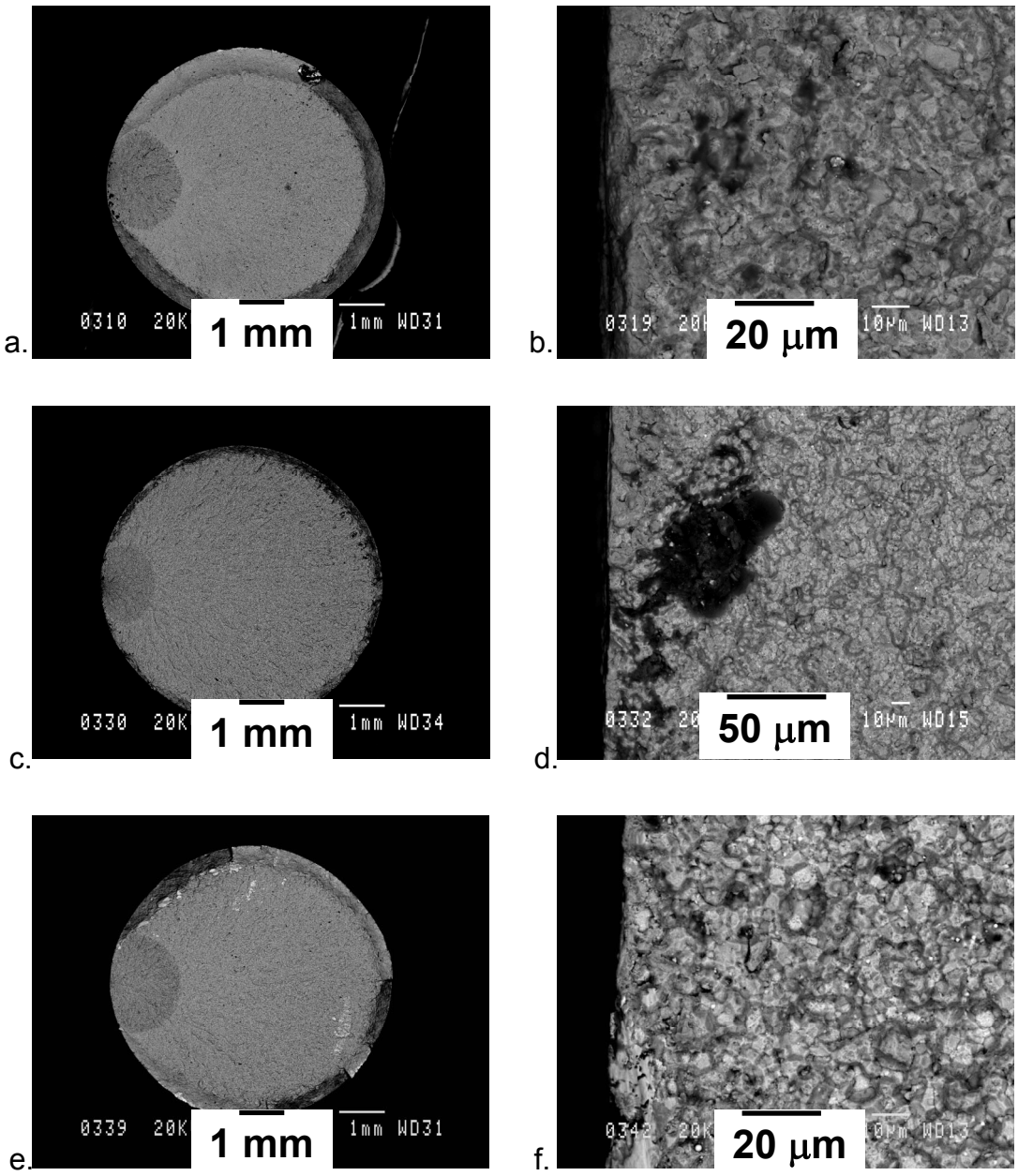

Figure 20.—Fracture surfaces observed for subrsolvus creep specimens tested at a. and b. 1200 °F/125 ksi, c. and d. 1300 °F/100 ksi, e. and f. 1400 °F/65 ksi.

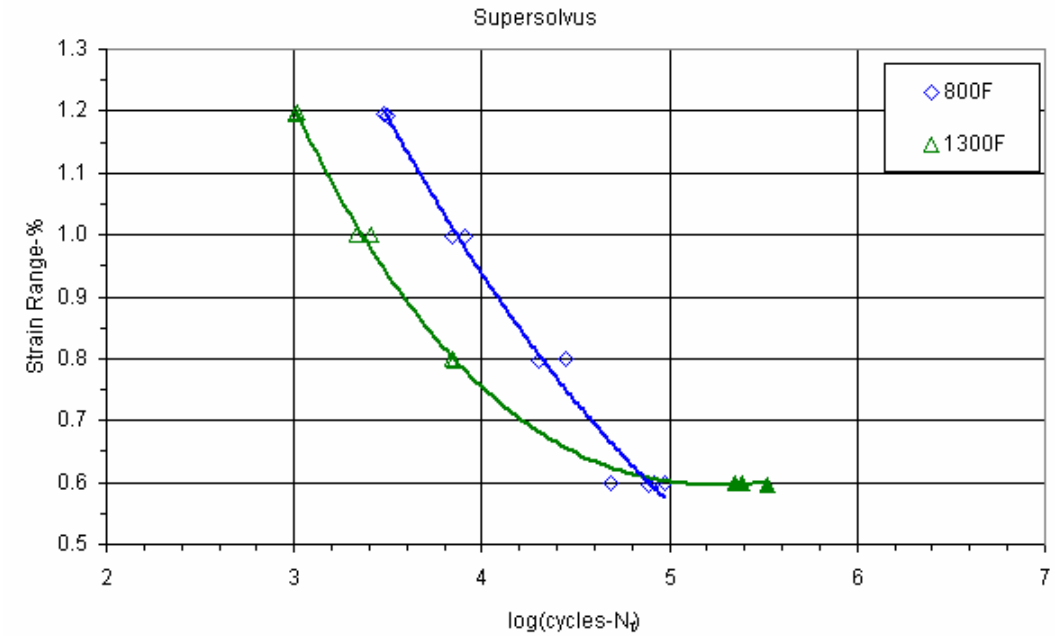

$\Delta\varepsilon_t = 0.089782(\log N_f)^2 - 1.177(\log N_f) + 4.211$

$R^2 = 0.985$

a. $\Delta\varepsilon_t = -0.019580886(\log N_f)^3 + 0.384113(\log N_f)^2 - 2.416(\log N_f) + 5.524$

$R^2 = 0.998$

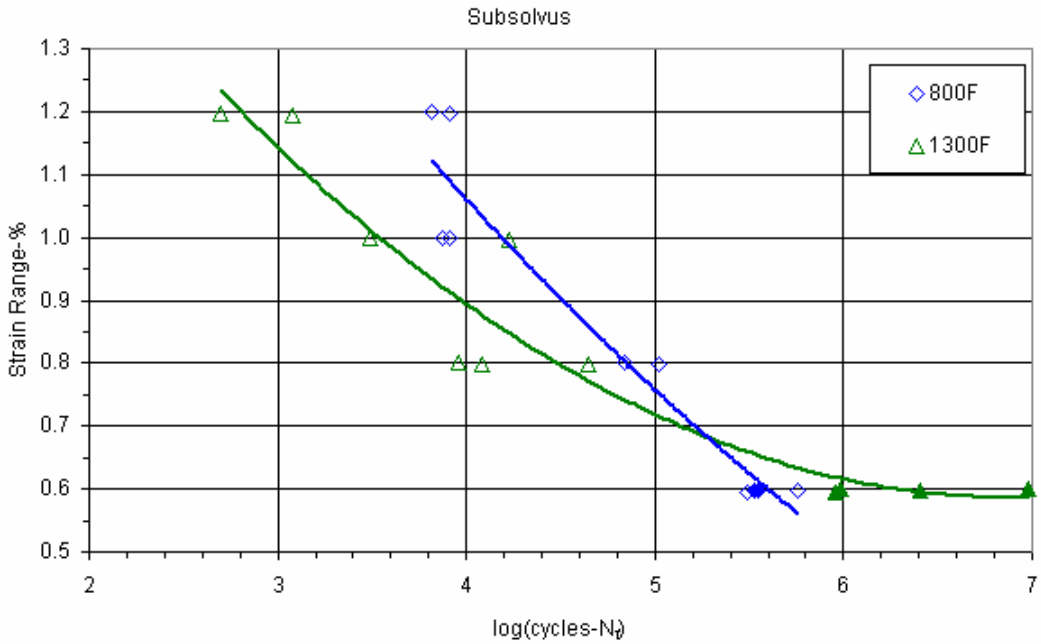

$\Delta\varepsilon_t = 0.024921(\log N_f)^2 - 0.527(\log N_f) + 2.770$

$R^2 = 0.923$

b. $\Delta\varepsilon_t = 0.036536(\log N_f)^2 - 0.505(\log N_f) + 2.328$

$R^2 = 0.912$

Figure 21.—Fatigue lives vs. strain range for a. supersolvus and b. subsolvus material. Open symbols=surface-initiated failures, filled symbols=internal-initiated failures.

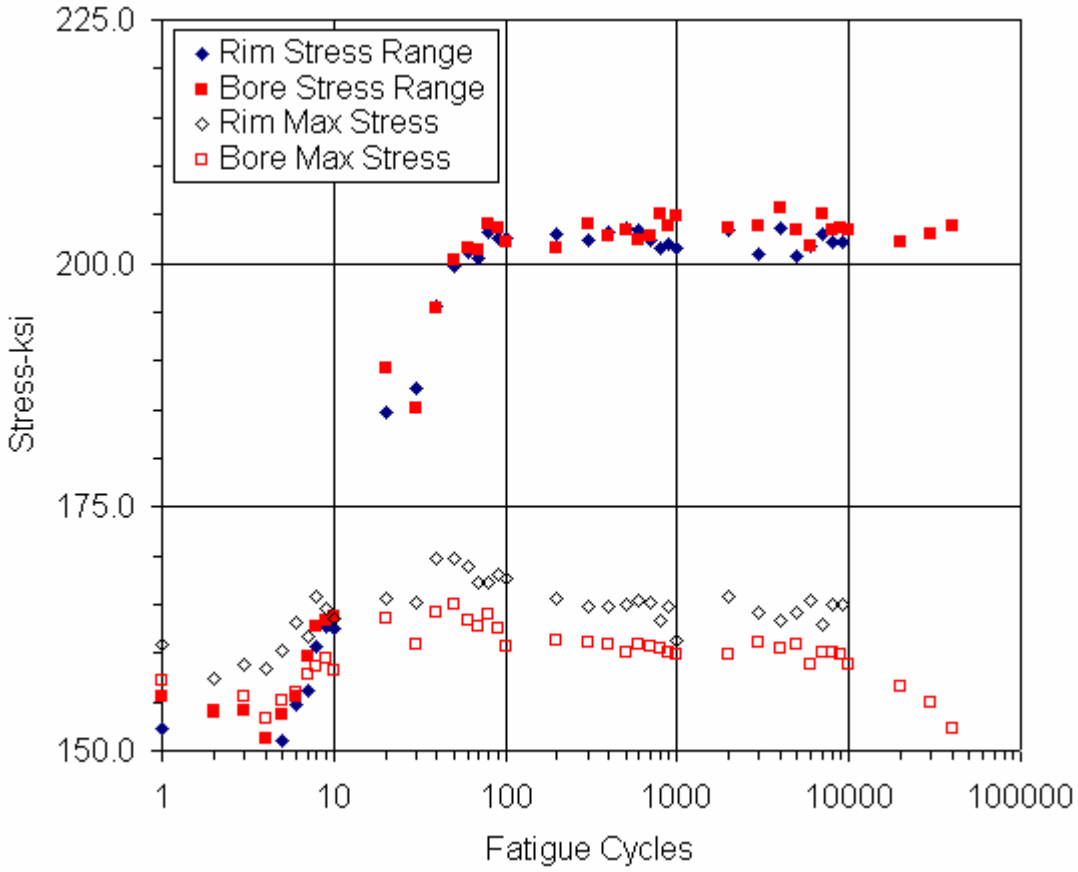

Figure 22.—Maximum stress and stress range as functions of cycles for subsolvus rim and bore specimens both tested at a total strain range of 0.8% and 1300 °F.

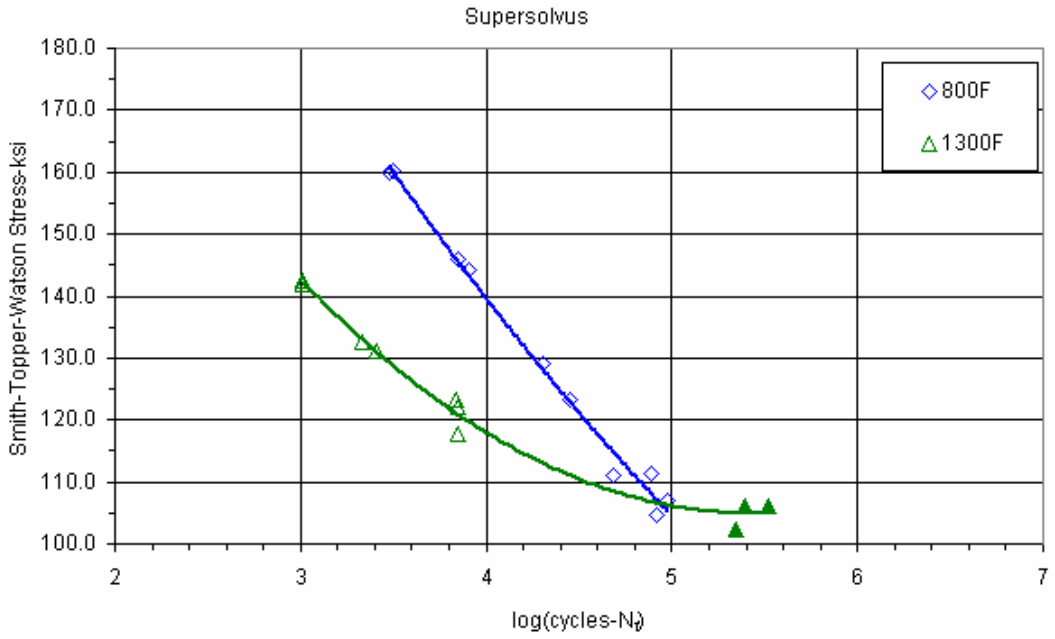

$\Delta\sigma_{SWT} = 3.759529(\log N_f)^2 - 68.865(\log N_f) + 355.0$

$R^2 = 0.992$

$\Delta\sigma_{SWT} = 6.371891(\log N_f)^2 - 69.228(\log N_f) + 293.0$

$R^2 = 0.987$

a.

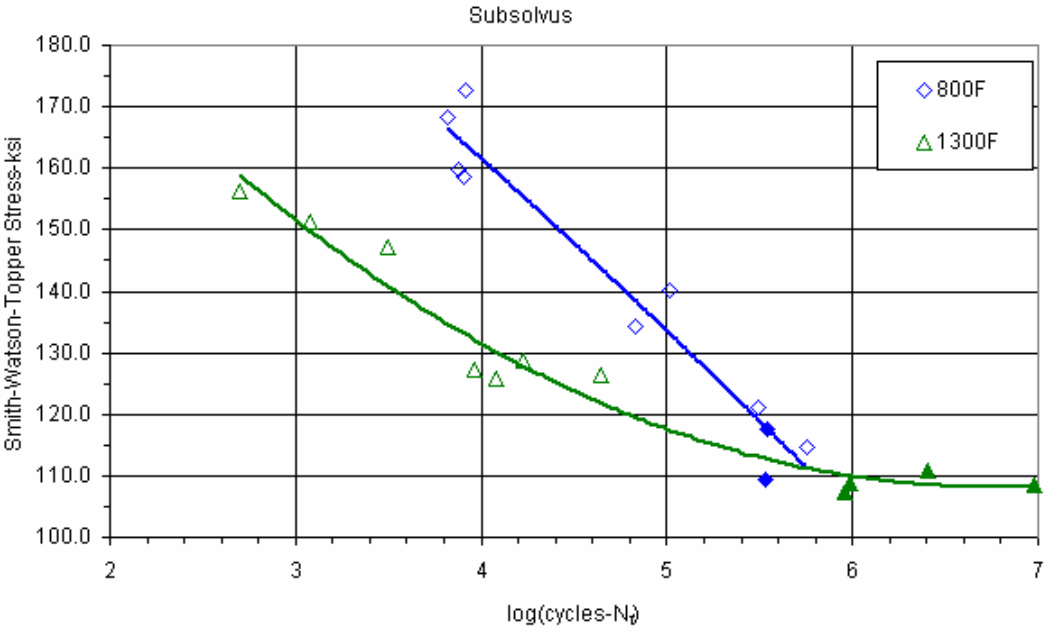

$\Delta\sigma_{SWT} = -0.927606(\log N_f)^2 - 19.646(\log N_f) + 255.0$

$R^2 = 0.943$

$\Delta\sigma_{SWT} = 3.080700(\log N_f)^2 - 41.631(\log N_f) + 248.8$

$R^2 = 0.959$

b.

Figure 23.—Fatigue lives vs. Smith-Watson-Topper stress for a. supersolvus and b. subsolvus material. Open symbols=surface-initiated failures, filled symbols=internal-initiated failures.

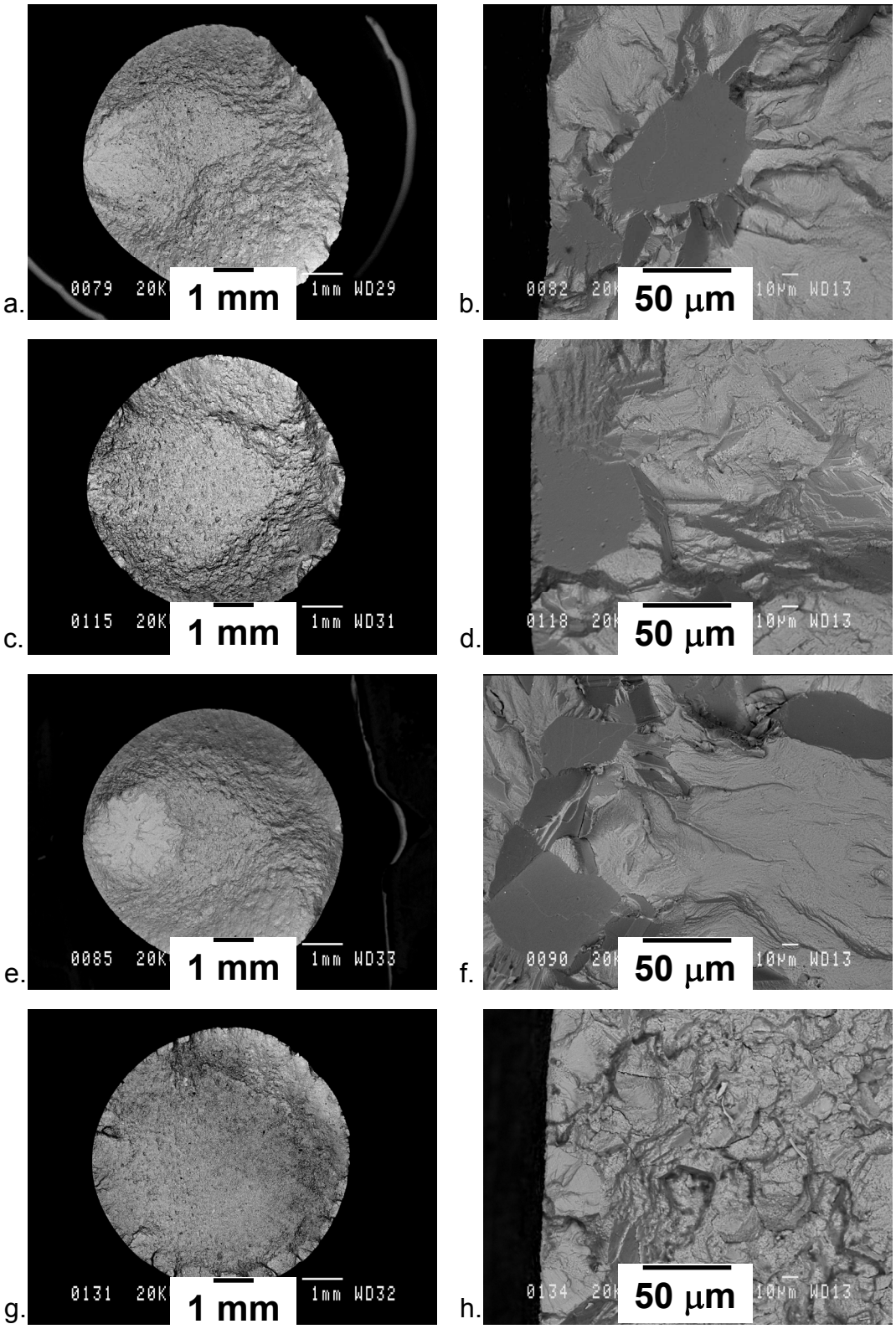

Figure 24.—Failure initiation sites observed for supersolvus LCF specimens tested at a. and b. 800 °F/0.6%, c. and d. 800 °F/1.2%, e. and f. 1300 °F/0.6%, g. and h. 1300 °F/1.2%.

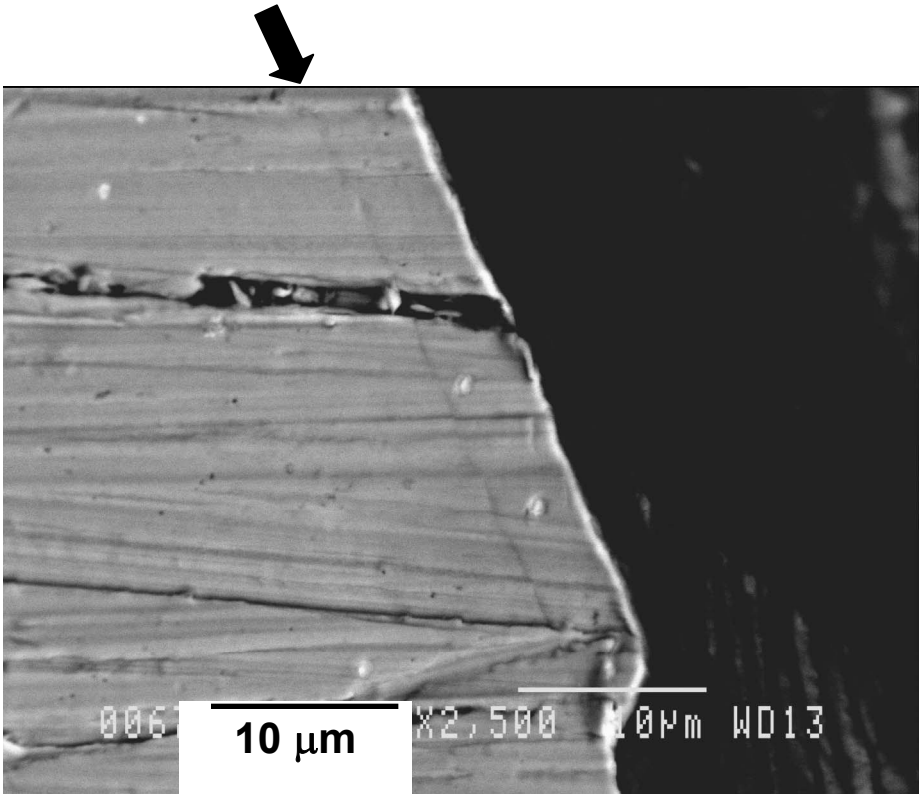

Figure 25.—Slip offset at arrow adjacent to grain facet initiated failure observed for supersolvus LCF specimen tested at 800 °F/0.8%.

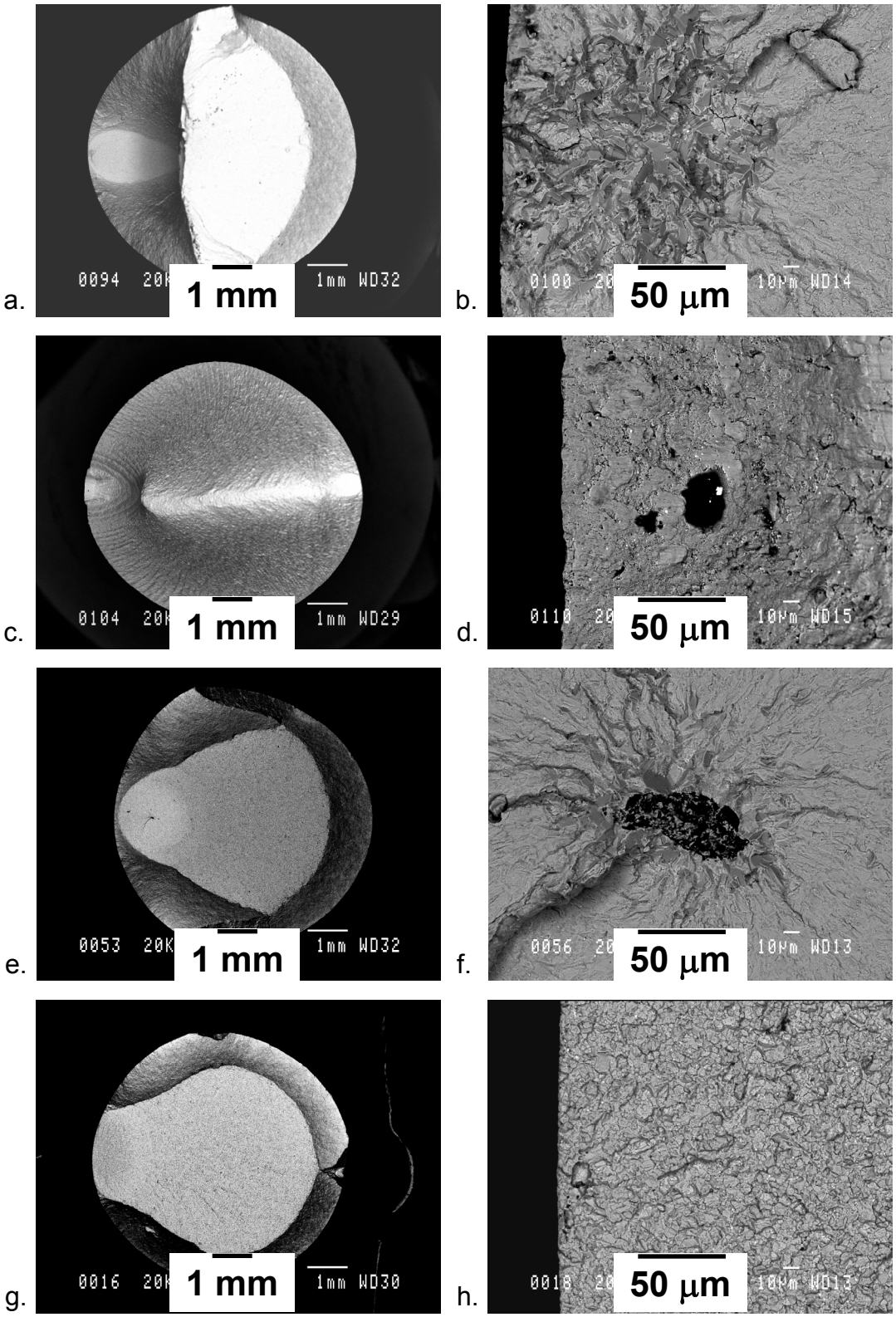

Figure 26.—Failure initiation sites observed for subsolvus LCF specimens tested at a. and b. 800 °F/0/6%, c. and d. 800 °F/1.2%, e. and f. 1300 °F/0.6%, g. and h. 1300 °F/1.2%.

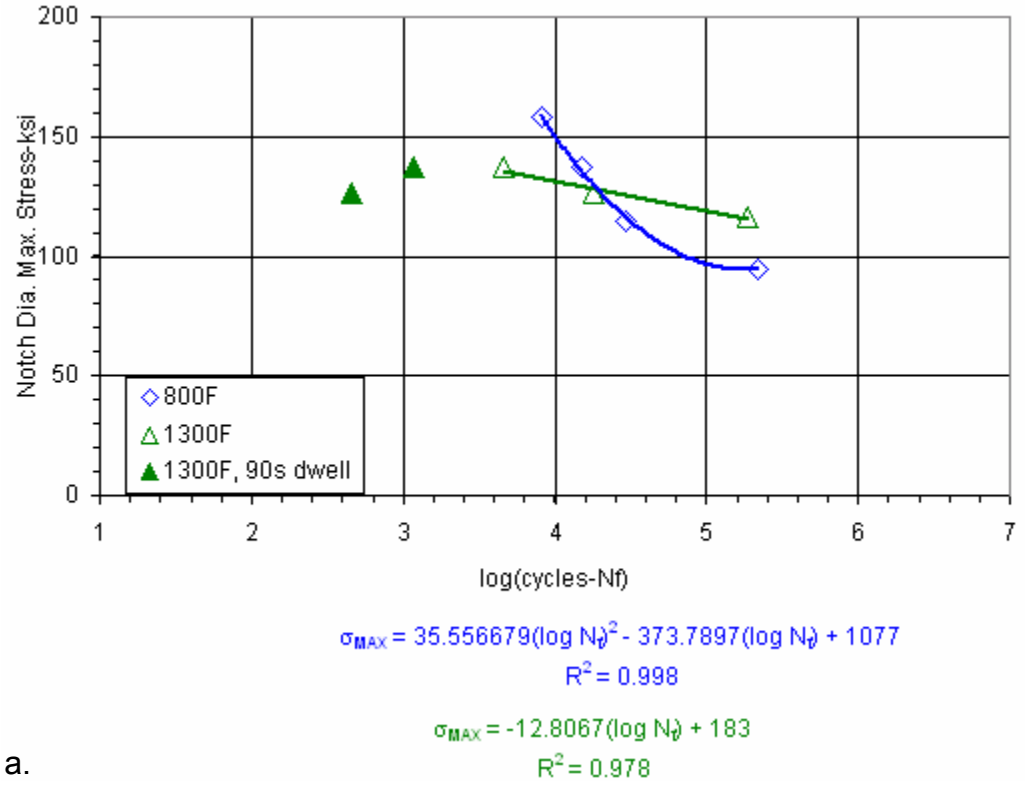

a.

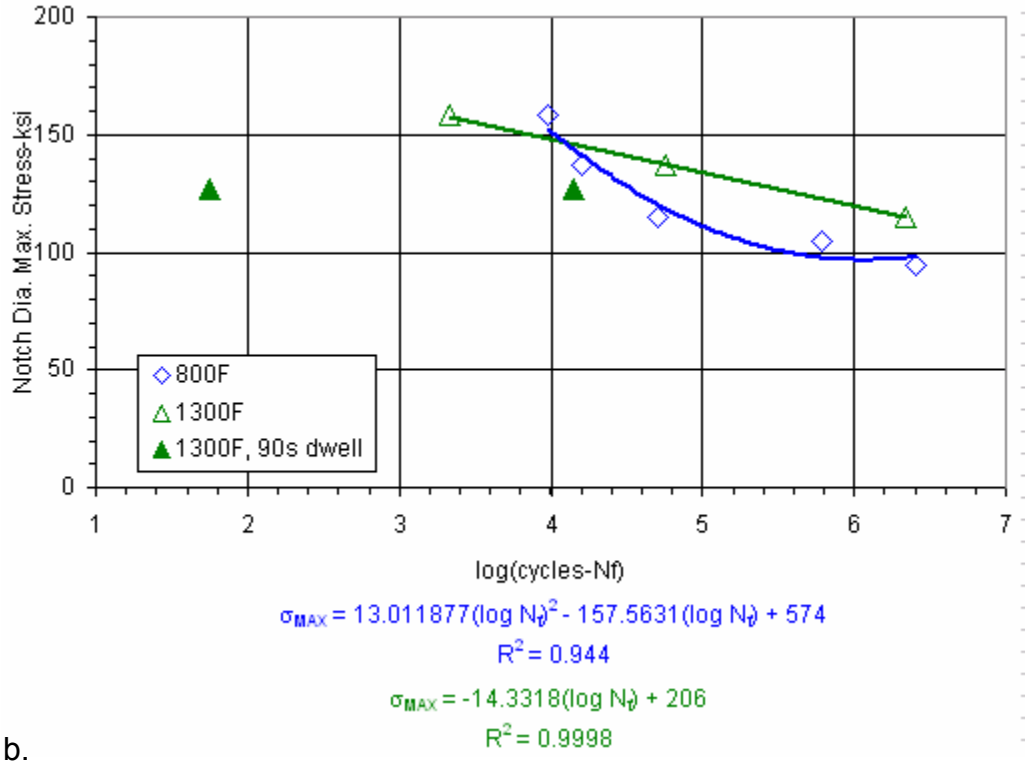

b.

Figure 27.—Fatigue lives vs. notch diameter maximum stress for a. supersolvus and b. subsolvus material.

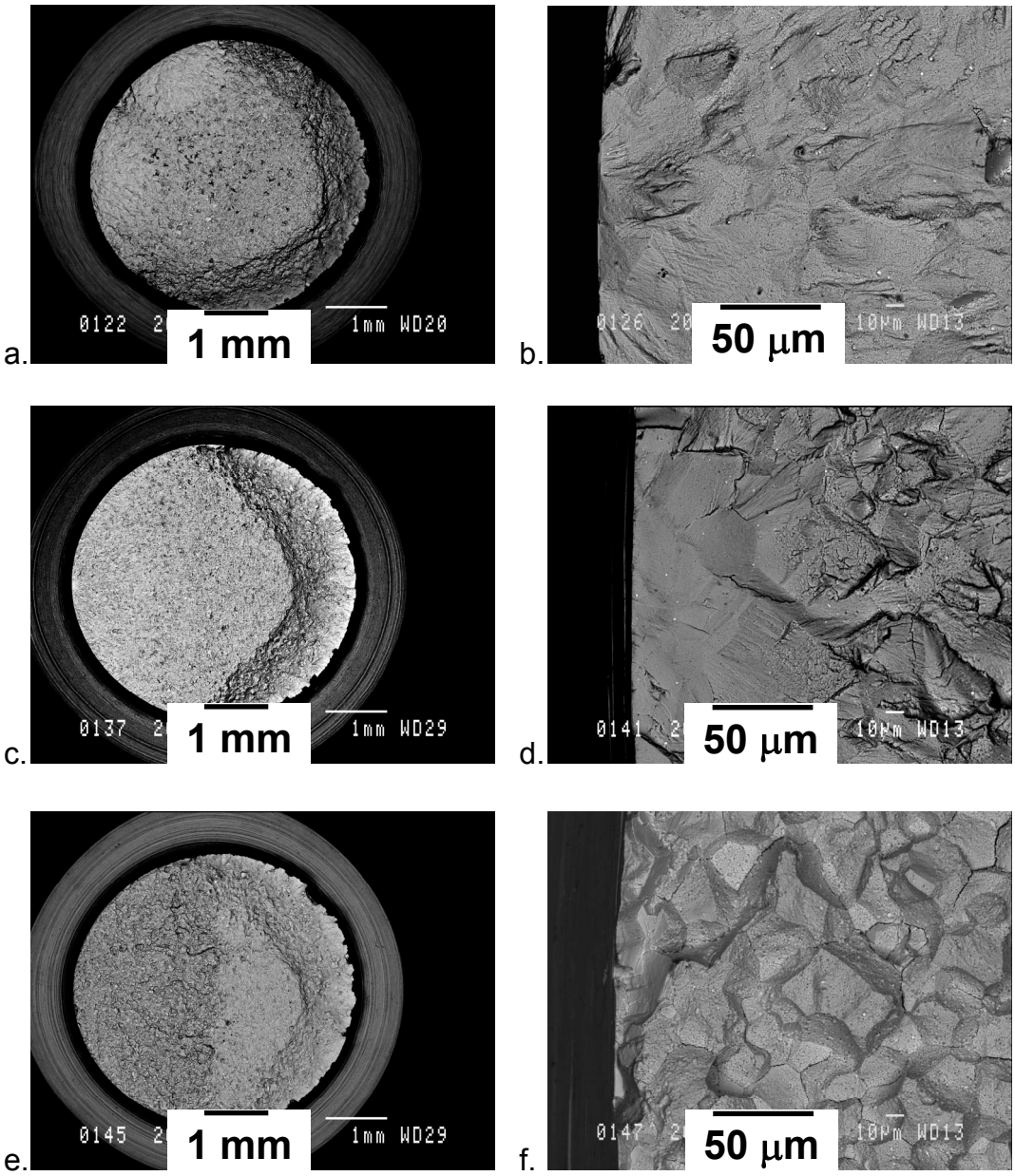

Figure 28.—Failure initiation sites observed for supersolvus notched LCF specimens tested at: a. and b. 800 °F/115 ksi maximum stress, c. and d. 1300 °F/127 ksi, e. and f. 1300 °F/127 ksi with superimposed 90 sec dwell.

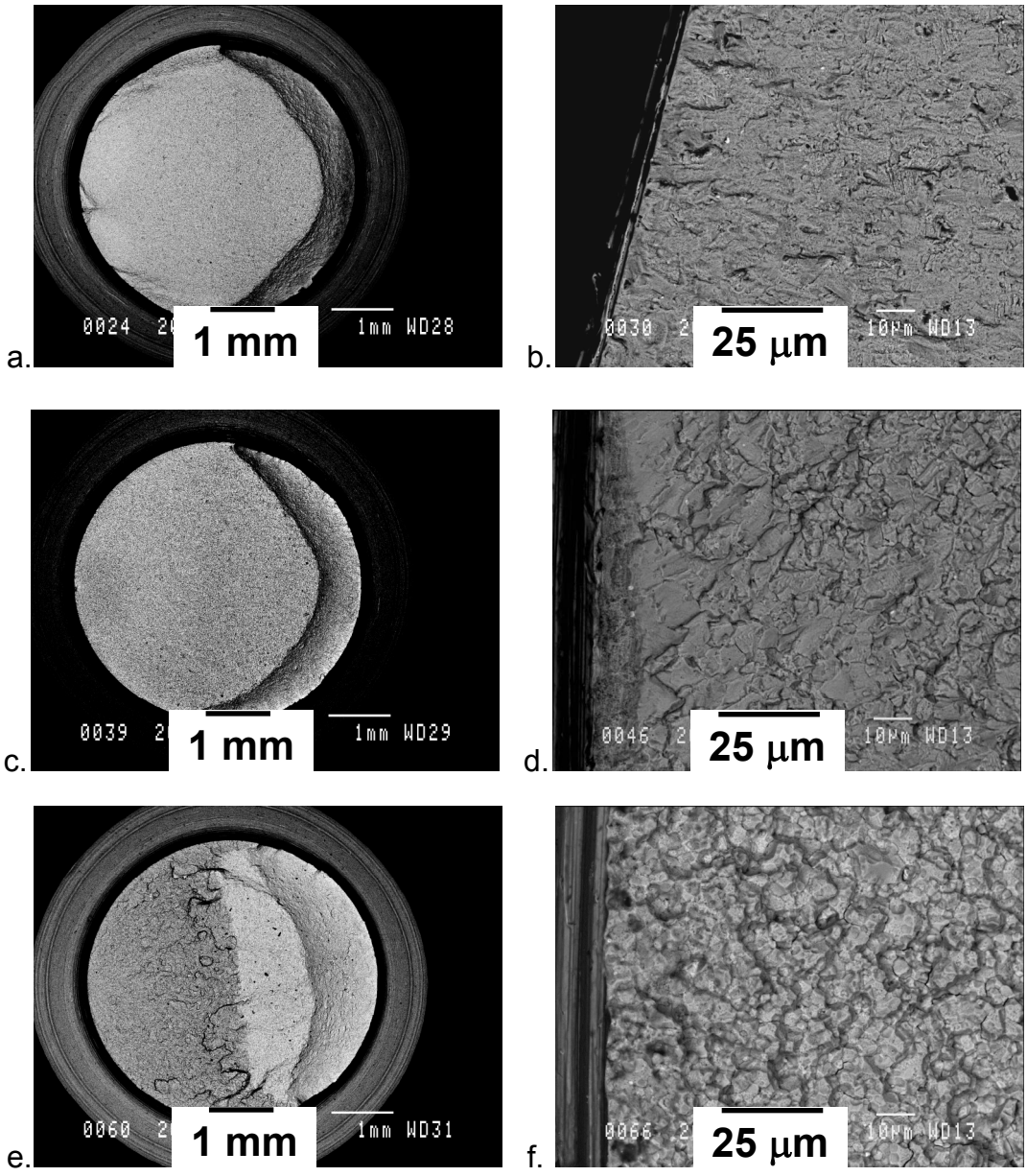

Figure 29.—Failure initiation sites observed for subsolvus notched LCF specimens tested at: a. and b. 800 °F/115 ksi maximum stress, c. and d. 1300 °F/115 ksi, e. and f. 1300 °F/127 ksi with superimposed 90 sec dwell.

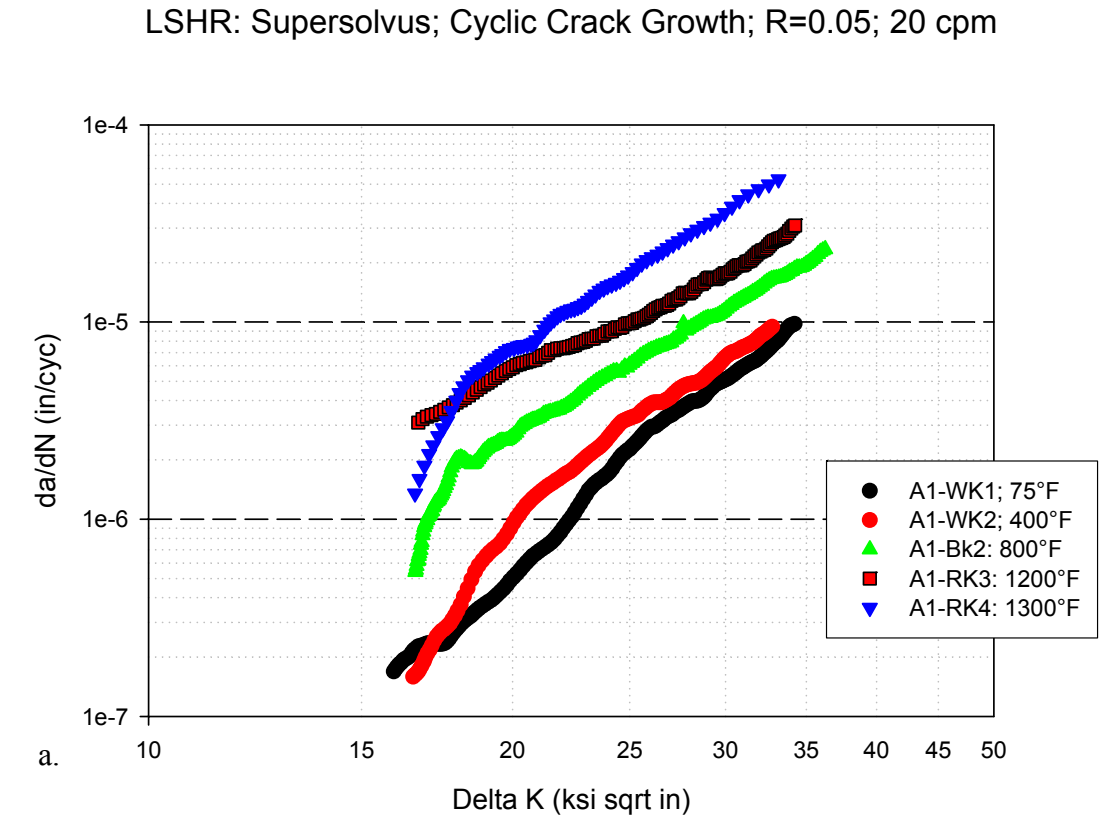

a.

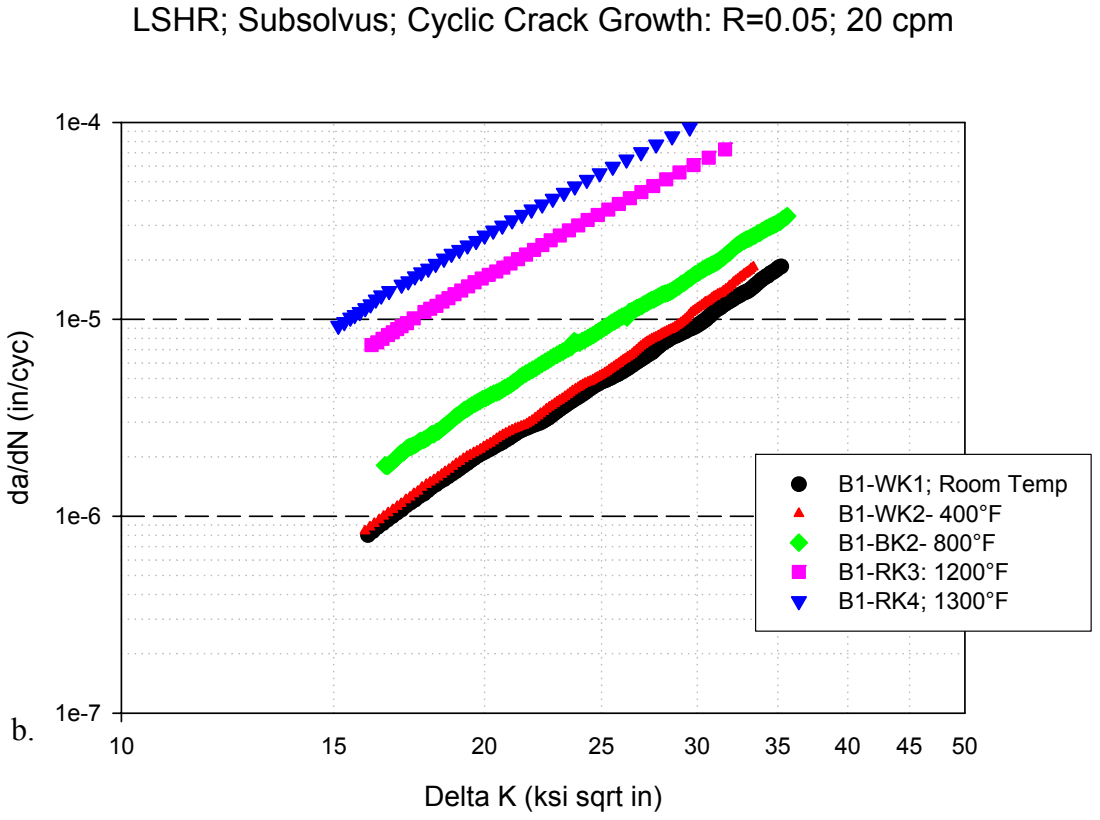

b.

Figure 30.—Comparison of fatigue crack growth rates in cyclic tests at a frequency of 0.33 Hz: a. supersolvus, b. subsolvus.

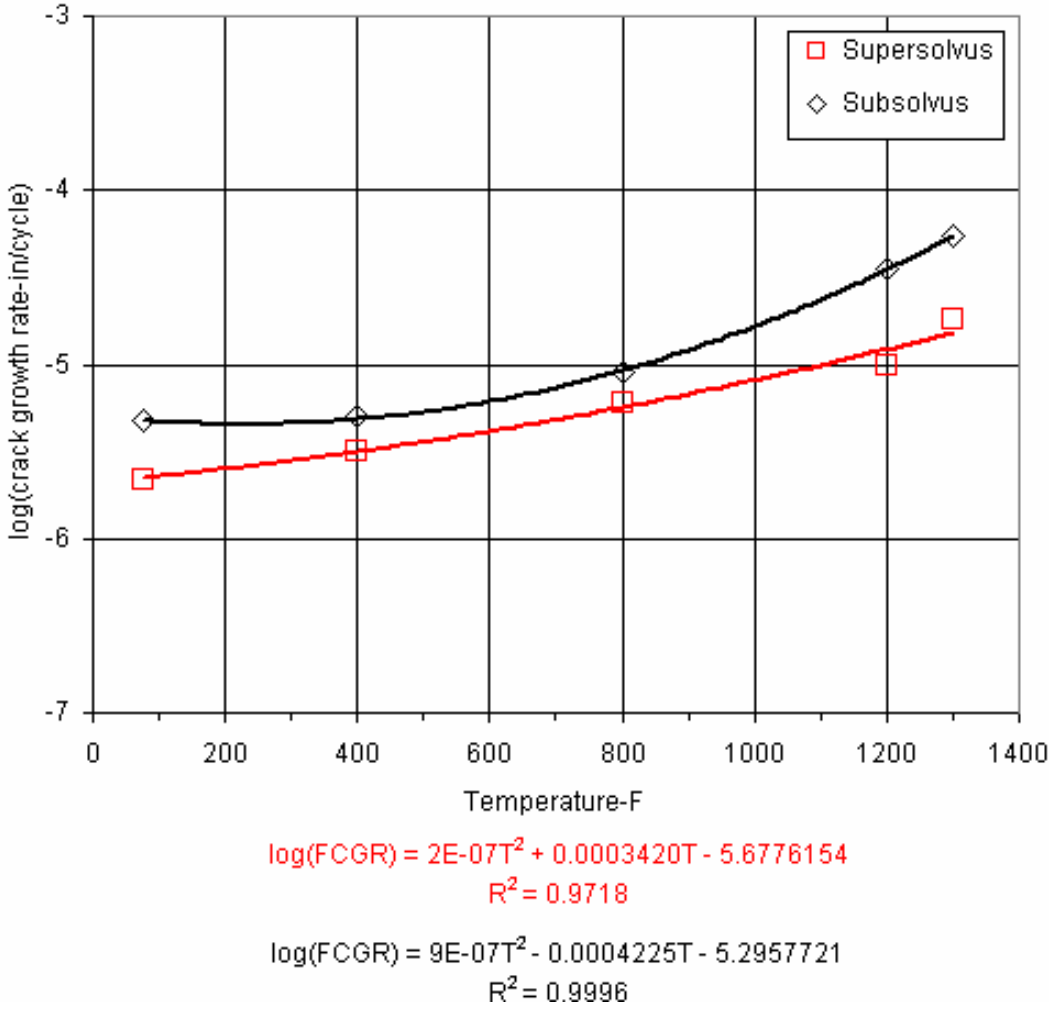

Figure 31.—Comparison of fatigue crack growth rates in cyclic tests at 25 ksi*in$^{0.5}$ vs. temperature.

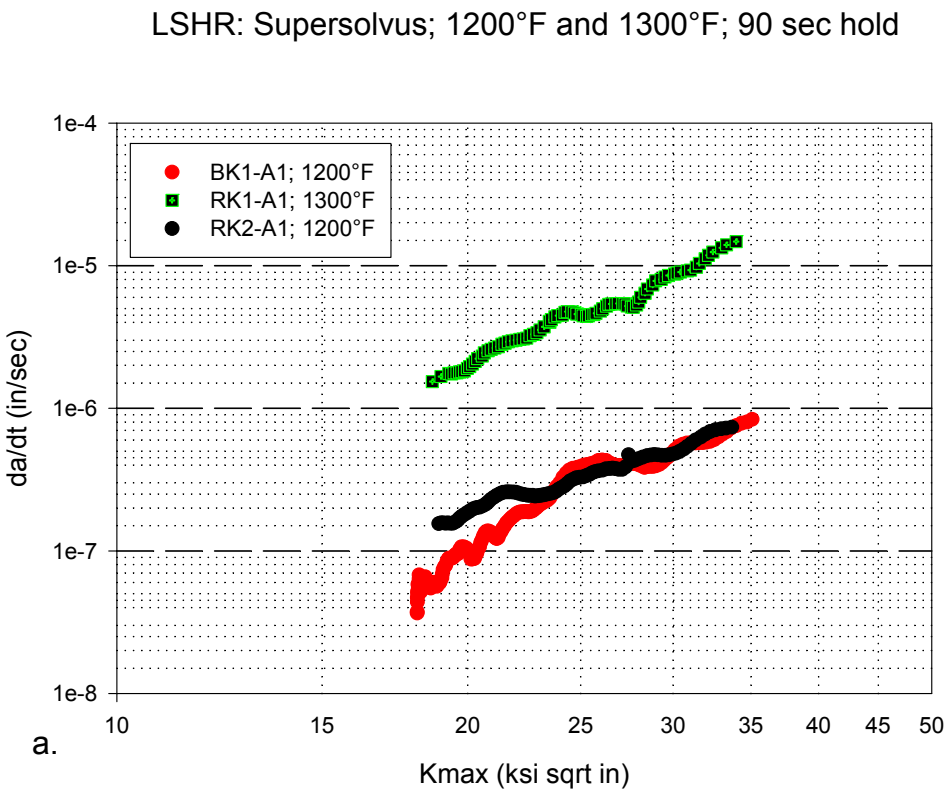

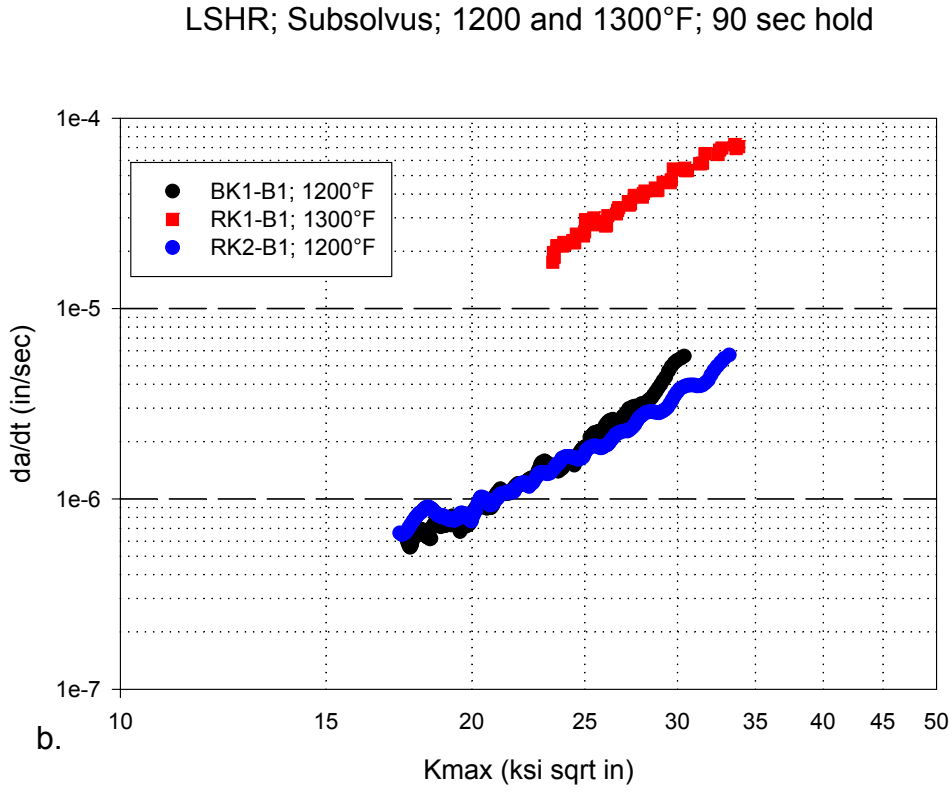

Figure 32.—Comparison of dwell fatigue crack growth rates in tests with 90 s hold at maximum stress: a. supersolvus, b. subsolvus.

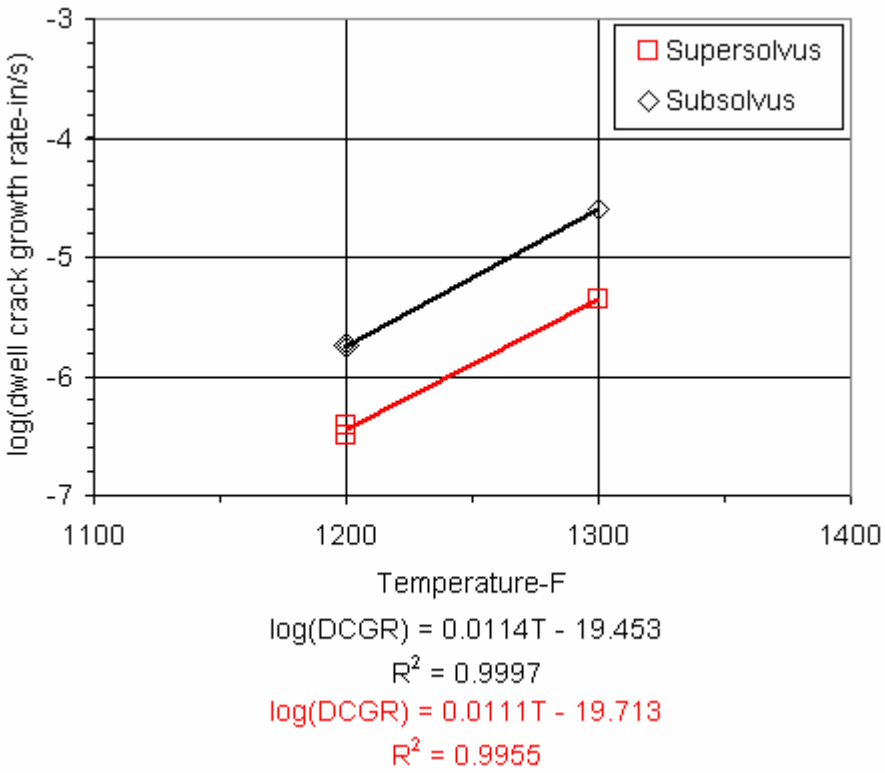

Figure 33.—Comparison of 90 s dwell fatigue crack growth rates at 25 ksi*in$^{0.5}$ vs. temperature.

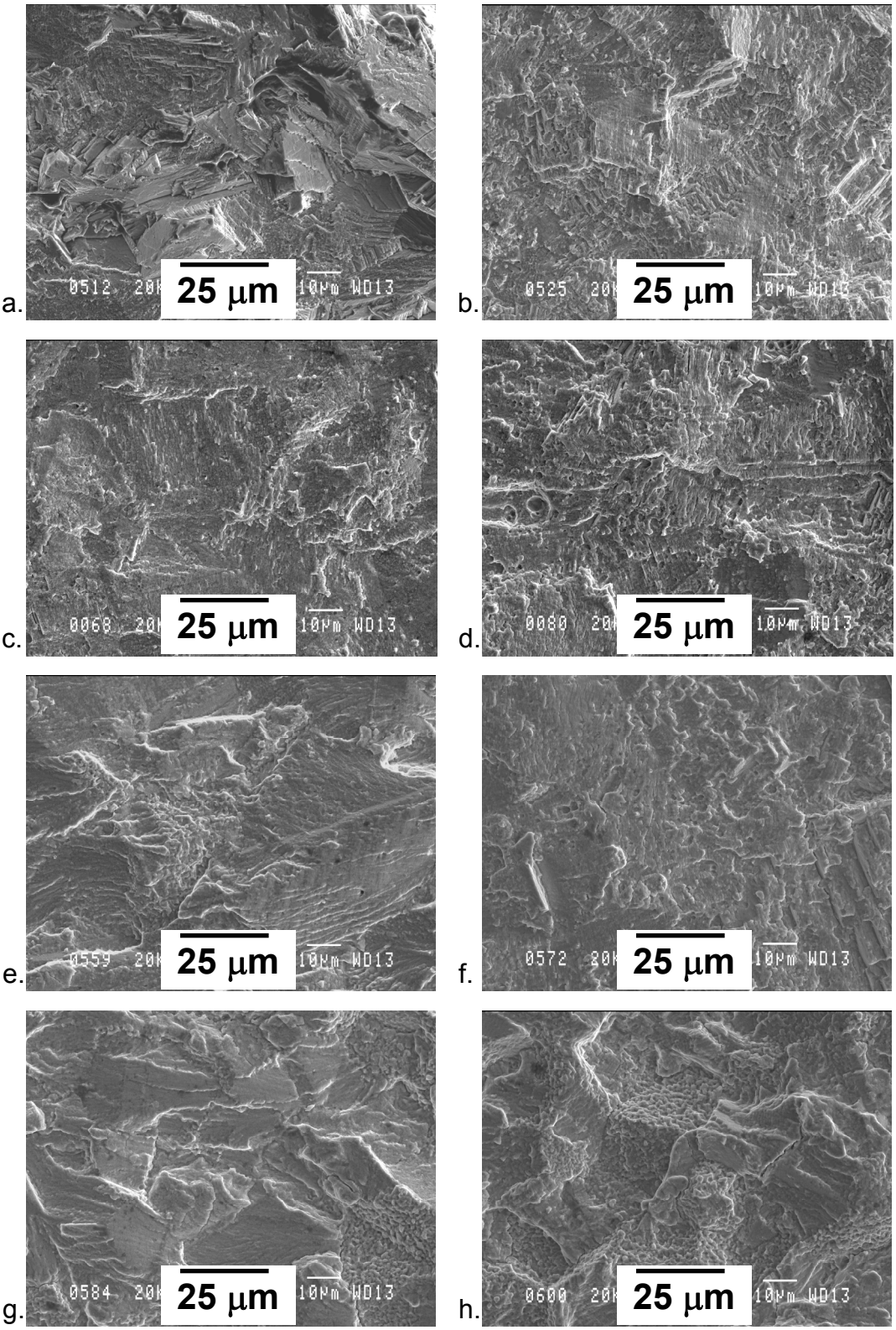

Figure 34.—Fatigue cracking of supersolvus cyclic fatigue crack growth specimens tested at: a. 75 °F, low K_{max}, b. 75 °F, high K_{max}, c. 800 °F, low K_{max}, d. 800 °F, high K_{max}, e. 1200 °F, low K_{max}, f. 1200 °F, high K_{max}, g. 1300 °F, low K_{max}, h. 1300 °F, high K_{max}

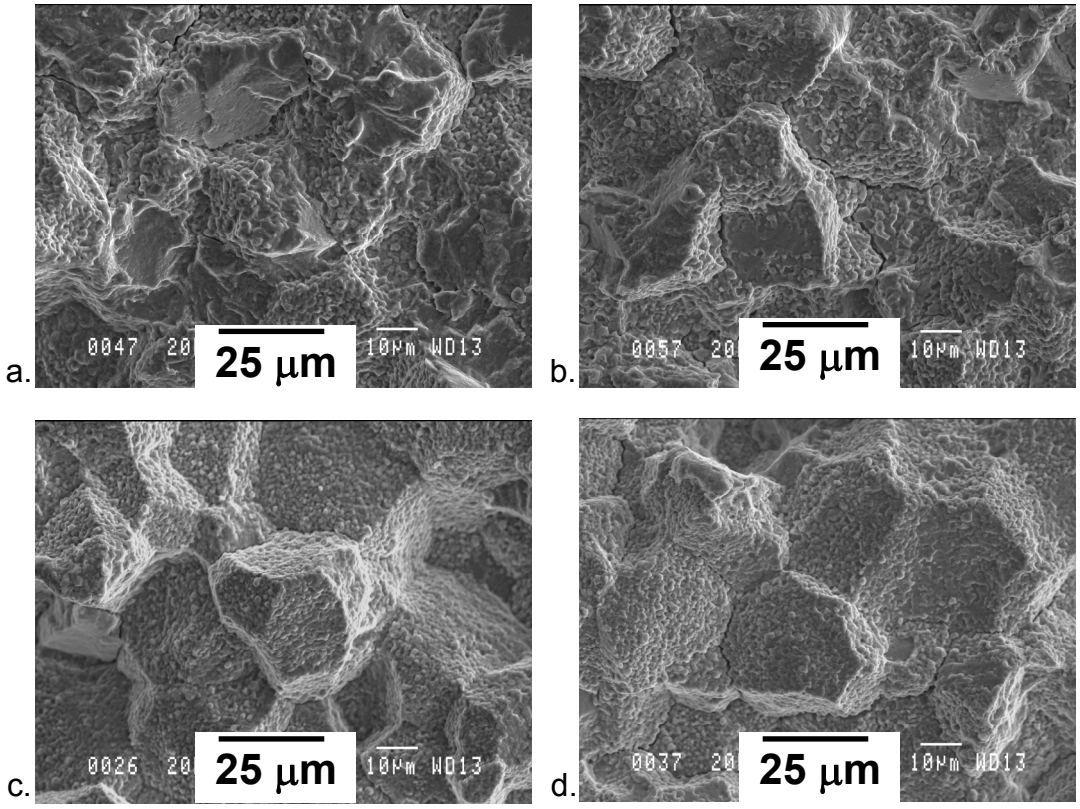

Figure 35.—Fatigue cracking of supersolvus 90 s dwell fatigue crack growth specimens tested at: a. 1200 °F, low K_{max}, b. 1200 °F, high K_{max}, c. 1300 °F, low K_{max}, d. 1300 °F, high K_{max}.

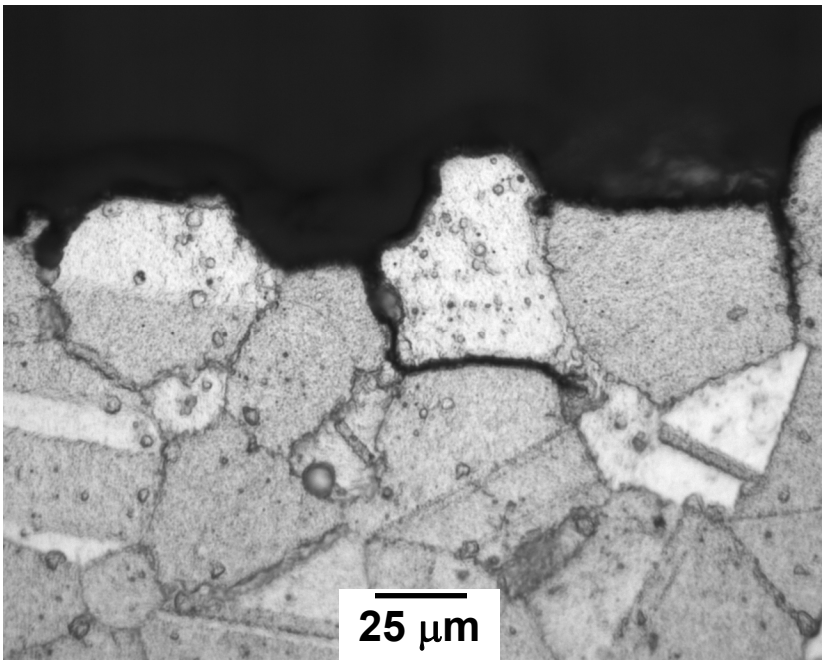

Figure 36.—Metallographic section showing intergranular fatigue cracking of supersolvus specimen tested at 1200 °F in 90 s dwell fatigue crack growth.

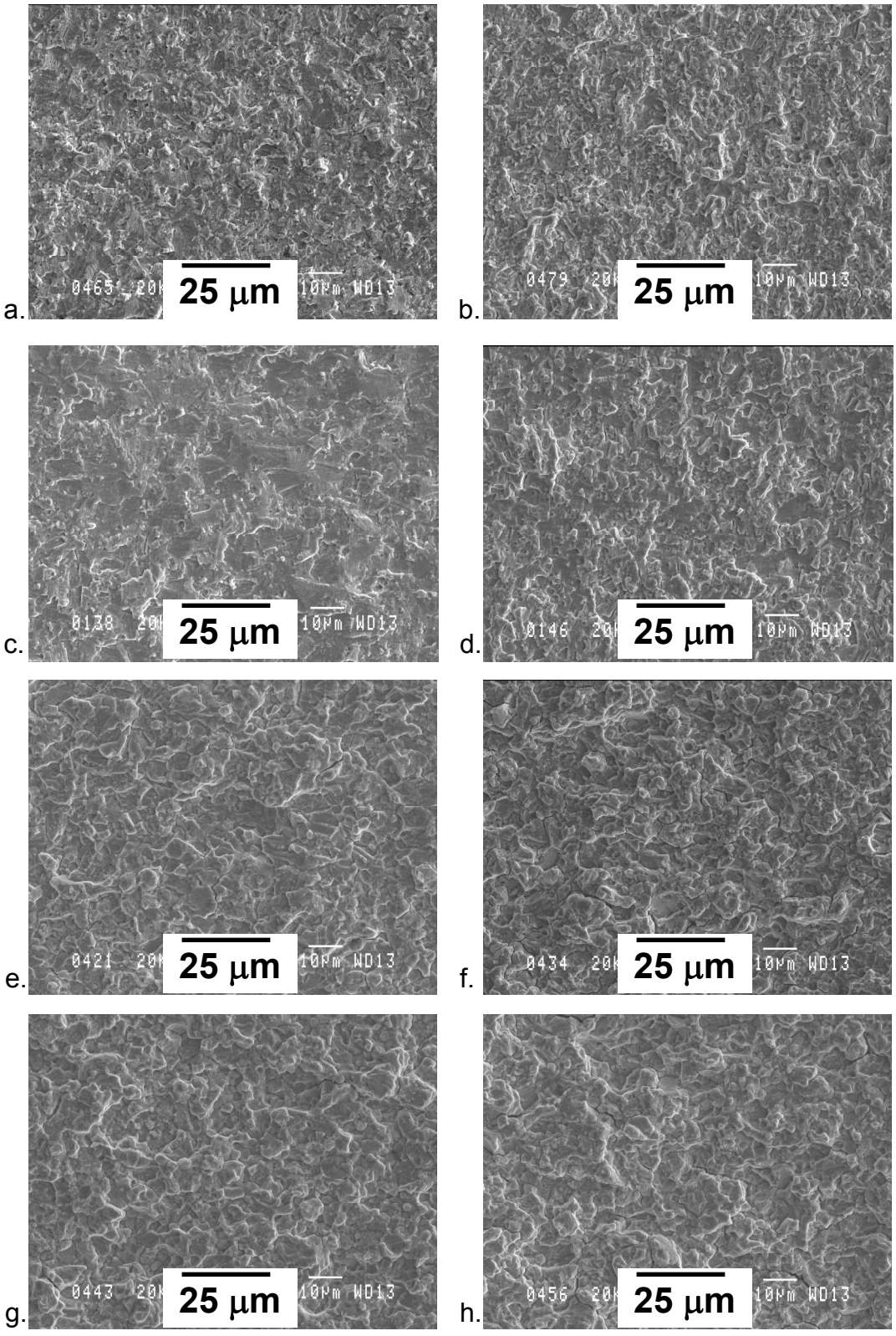

Figure 37.—Fatigue cracking of subsolvus cyclic fatigue crack growth specimens tested at: a. 75 °F, low K_{max}, b. 75 °F, high K_{max}, c. 800 °F, low K_{max}, d. 800 °F, high K_{max}, e. 1200 °F, low K_{max}, f. 1200 °F, high K_{max}, g. 1300 °F, low K_{max}, h. 1300 °F, high K_{max}

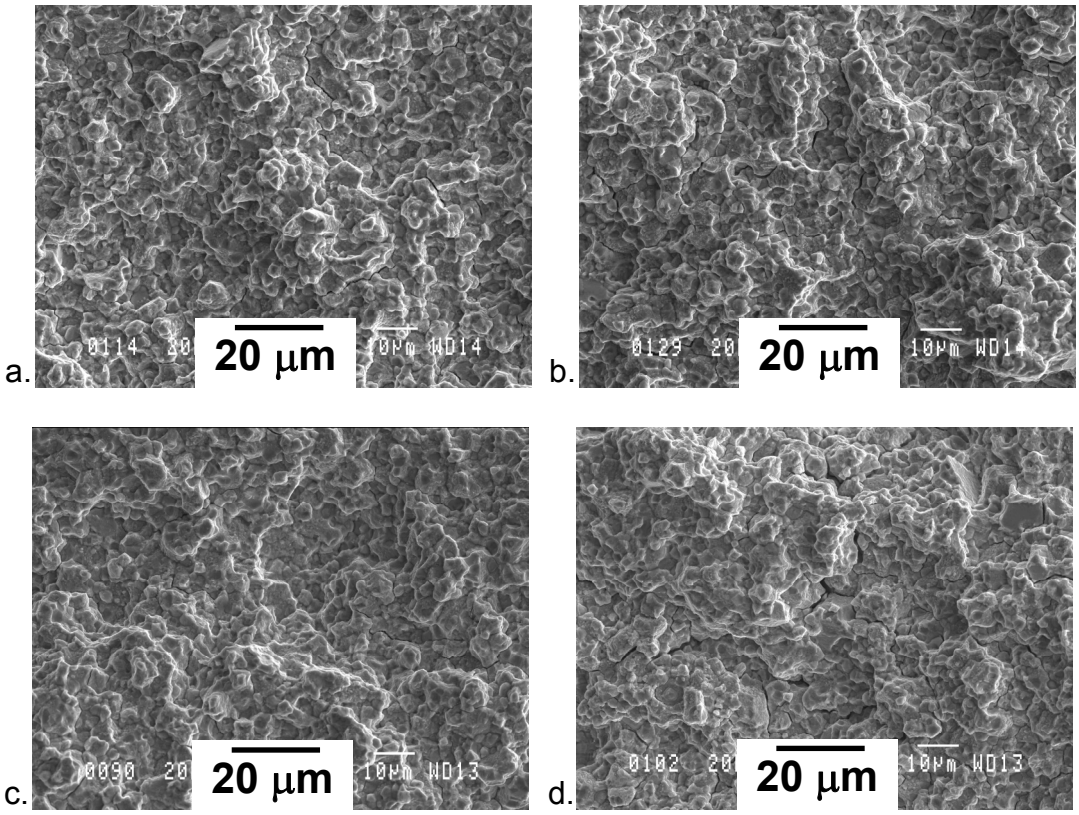

Figure 38.—Fatigue cracking of subsolvus 90 s dwell fatigue crack growth specimens tested at: a. 1200 °F, low K_{max}, b. 1200 °F, high K_{max}, c. 1300 °F, low K_{max}, d. 1300 °F, high K_{max}.

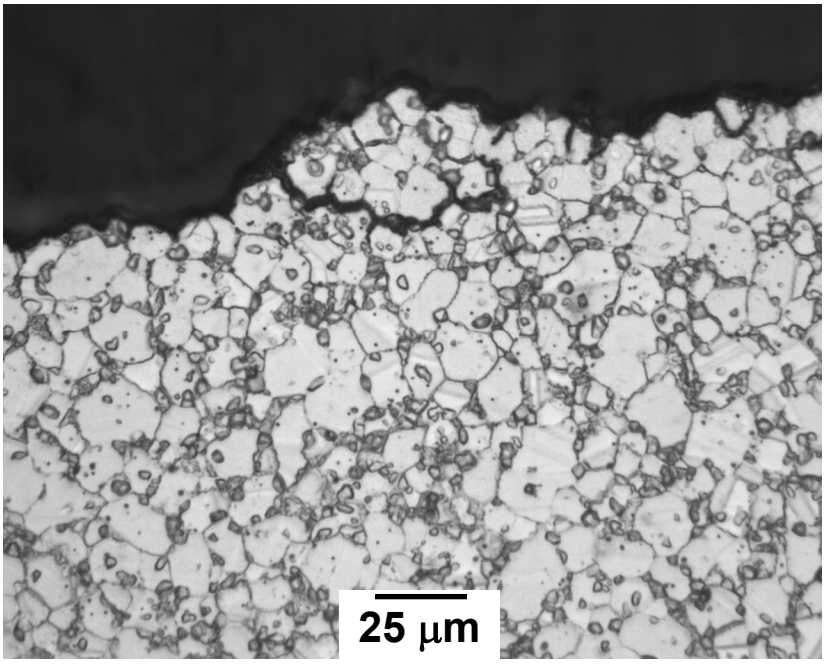

Figure 39.—Metallographic section showing intergranular fatigue cracking of subsolvus specimen tested at 1200 °F in 90 s dwell fatigue crack growth .

Appendix 1—Tabulated Thermal Diffusivity Results

Temperature-F		Thermal Diffusivity-ft^2/hr		
SpecID	2-L2-1	2-L2-2	T7-1-1	T7-1-2
Disk	Supersolvus	Supersolvus	Subsolvus	Subsolvus
73	0.10230	0.10269	0.10540	0.10540
122	0.10463	0.10618	0.10811	0.10656
212	0.11005	0.11083	0.11393	0.11276
392	0.12206	0.12129	0.12361	0.12245
572	0.13175	0.13020	0.13330	0.13175
752	0.14183	0.14105	0.14105	0.14028
932	0.15229	0.15190	0.15074	0.14996
1112	0.16236	0.16159	0.16081	0.16236
1292	0.16973	0.17128	0.17050	0.16895
1472	0.18290	0.18329	0.17748	0.17980
1652	0.17980	0.18058	0.17825	0.17631
1832	0.1802	0.18019	0.17670	0.18019
2012	0.1794	0.17980	0.17903	0.17903
2192	0.1848	0.18678	0.18484	0.18368

Appendix 2—Tabulated Specific Heat Results

Temperature-F	Specific Heat (Heating Data)-BTU/lbF			
SpecID	2-L2-1	2-L2-2	T7-1-1	T7-1-2
Disk	Supersolvus	Supersolvus	Subsolvus	Subsolvus
73	0.103	0.103	0.102	0.102
122	0.104	0.104	0.104	0.104
167	0.106	0.106	0.106	0.106
212	0.107	0.108	0.107	0.107
257	0.108	0.110	0.108	0.108
302	0.110	0.111	0.109	0.110
347	0.111	0.112	0.111	0.110
392	0.112	0.113	0.112	0.111
437	0.113	0.114	0.113	0.112
482	0.114	0.114	0.114	0.113
527	0.114	0.115	0.115	0.113
572	0.115	0.116	0.116	0.114
617	0.116	0.116	0.116	0.115
662	0.116	0.117	0.117	0.115
707	0.117	0.118	0.118	0.116
752	0.118	0.118	0.118	0.116
797	0.118	0.119	0.119	0.117
842	0.119	0.120	0.119	0.118
887	0.120	0.121	0.120	0.119
932	0.120	0.121	0.122	0.119
941	0.120	0.121	0.122	0.120
950	0.120	0.121	0.122	0.119
959	0.120	0.121	0.122	0.119
968	0.120	0.121	0.121	0.119
977	0.120	0.121	0.121	0.119
986	0.121	0.121	0.122	0.120
995	0.120	0.122	0.121	0.120
1004	0.120	0.122	0.122	0.120
1013	0.121	0.122	0.122	0.121
1022	0.120	0.122	0.122	0.120
1031	0.120	0.121	0.122	0.120
1040	0.120	0.121	0.123	0.121
1049	0.120	0.121	0.123	0.121
1058	0.120	0.121	0.123	0.122
1067	0.118	0.120	0.122	0.121
1076	0.119	0.120	0.123	0.121
1085	0.118	0.120	0.123	0.122
1094	0.118	0.120	0.124	0.123
1103	0.118	0.120	0.123	0.122
1112	0.118	0.120	0.123	0.123
1121	0.120	0.122	0.126	0.126
1130	0.121	0.122	0.127	0.126
1139	0.121	0.122	0.128	0.126
1148	0.121	0.124	0.130	0.127
1157	0.123	0.124	0.130	0.127
1166	0.125	0.126	0.131	0.129
1175	0.127	0.128	0.133	0.131
1184	0.129	0.130	0.135	0.132
1193	0.132	0.133	0.137	0.133
1202	0.132	0.133	0.137	0.133
1211	0.133	0.135	0.138	0.134
1220	0.135	0.136	0.138	0.134
1229	0.135	0.136	0.138	0.135
1238	0.135	0.136	0.138	0.136
1247	0.136	0.137	0.140	0.137
1256	0.137	0.138	0.140	0.137

Temperature-F	Specific Heat (Cooling Data)-BTU/lbF			
SpecID	2-L2-1	2-L2-2	T7-1-1	T7-1-2
Disk	Supersolvus	Supersolvus	Subsolvus	Subsolvus
392	0.110	0.107	0.111	0.114
401	0.110	0.107	0.111	0.114
410	0.110	0.107	0.111	0.114
419	0.110	0.108	0.111	0.114
428	0.111	0.108	0.111	0.114
437	0.111	0.108	0.112	0.114
446	0.111	0.108	0.112	0.114
455	0.111	0.109	0.112	0.115
464	0.112	0.109	0.112	0.115
473	0.112	0.109	0.113	0.115
482	0.112	0.109	0.113	0.115
491	0.112	0.110	0.113	0.115
500	0.112	0.110	0.113	0.115
509	0.113	0.110	0.114	0.115
518	0.113	0.110	0.114	0.115
527	0.113	0.110	0.114	0.115
536	0.113	0.111	0.114	0.116
545	0.113	0.111	0.115	0.116
554	0.114	0.111	0.115	0.116
563	0.114	0.111	0.115	0.116
572	0.114	0.112	0.116	0.116
581	0.114	0.112	0.116	0.116
590	0.115	0.112	0.116	0.117
599	0.115	0.112	0.116	0.117
608	0.115	0.113	0.117	0.117
617	0.115	0.113	0.117	0.117
626	0.115	0.113	0.117	0.117
635	0.115	0.113	0.117	0.117
644	0.115	0.113	0.117	0.117
653	0.115	0.114	0.117	0.117
662	0.115	0.114	0.117	0.117
671	0.116	0.114	0.117	0.118
680	0.116	0.114	0.117	0.118
689	0.116	0.114	0.117	0.118
698	0.116	0.115	0.118	0.118
707	0.116	0.114	0.118	0.119
716	0.116	0.114	0.118	0.118
725	0.116	0.114	0.118	0.118
734	0.116	0.114	0.118	0.118
743	0.116	0.115	0.118	0.118
752	0.117	0.115	0.119	0.119
761	0.117	0.115	0.119	0.119
770	0.117	0.115	0.118	0.119
779	0.117	0.115	0.119	0.119
788	0.117	0.115	0.119	0.119
797	0.118	0.115	0.120	0.119
806	0.118	0.116	0.120	0.120
815	0.118	0.116	0.120	0.120
824	0.118	0.115	0.119	0.119
833	0.117	0.115	0.119	0.120
842	0.118	0.115	0.120	0.120
851	0.118	0.116	0.120	0.120
860	0.119	0.116	0.120	0.120
869	0.118	0.117	0.120	0.121
878	0.118	0.117	0.120	0.120
887	0.119	0.117	0.121	0.121

Appendix 2—Tabulated Specific Heat Results (cont.)

Temperature-F	Specific Heat (Heating Data)-BTU/lbF			
SpecID	2-L2-1	2-L2-2	T7-1-1	T7-1-2
Disk	Supersolvus	Supersolvus	Subsolvus	Subsolvus
1265	0.135	0.136	0.137	0.135
1274	0.136	0.138	0.139	0.136
1283	0.136	0.137	0.139	0.136
1292	0.135	0.137	0.138	0.137
1301	0.138	0.140	0.140	0.139
1310	0.138	0.139	0.139	0.139
1319	0.138	0.140	0.140	0.139
1328	0.138	0.140	0.140	0.139
1337	0.139	0.141	0.142	0.139
1346	0.139	0.142	0.142	0.136
1355	0.140	0.142	0.144	0.138
1364	0.140	0.142	0.142	0.139
1373	0.139	0.140	0.138	0.137
1382	0.139	0.140	0.140	0.138
1391	0.141	0.142	0.141	0.139
1400	0.137	0.141	0.141	0.138
1409	0.139	0.141	0.142	0.139
1418	0.143	0.145	0.147	0.142
1427	0.142	0.144	0.149	0.141
1436	0.142	0.145	0.148	0.143
1445	0.140	0.144	0.146	0.142
1454	0.144	0.146	0.148	0.143
1463	0.144	0.149	0.151	0.146
1472	0.147	0.149	0.154	0.149
1481	0.144	0.147	0.152	0.147
1490	0.145	0.148	0.152	0.149
1499	0.147	0.149	0.154	0.152
1508	0.148	0.153	0.157	0.156
1517	0.154	0.157	0.165	0.159
1526	0.153	0.158	0.165	0.160
1535	0.160	0.165	0.172	0.168
1544	0.157	0.162	0.171	0.167
1553	0.163	0.166	0.174	0.171
1562	0.163	0.169	0.177	0.173
1571	0.166	0.171	0.177	0.173
1580	0.176	0.179	0.182	0.176
1589	0.176	0.180	0.184	0.177
1598	0.177	0.182	0.185	0.183
1607	0.182	0.185	0.192	0.189
1616	0.185	0.191	0.190	0.188
1625	0.185	0.187	0.191	0.190
1634	0.192	0.194	0.192	0.188
1643	0.192	0.190	0.194	0.192
1652	0.196	0.198	0.194	0.193
1661	0.192	0.194	0.191	0.189
1670	0.201	0.199	0.199	0.196
1679	0.197	0.198	0.197	0.194
1688	0.197	0.203	0.200	0.196
1697	0.196	0.202	0.198	0.196
1706	0.203	0.204	0.206	0.203
1715	0.201	0.206	0.210	0.205
1724	0.204	0.203	0.201	0.200
1733	0.209	0.209	0.208	0.202
1742	0.204	0.199	0.203	0.193
1751	0.212	0.206	0.207	0.203
1760	0.210	0.207	0.210	0.207

Temperature-F	Specific Heat (Cooling Data)-BTU/lbF			
SpecID	2-L2-1	2-L2-2	T7-1-1	T7-1-2
Disk	Supersolvus	Supersolvus	Subsolvus	Subsolvus
896	0.119	0.117	0.121	0.121
905	0.119	0.117	0.121	0.121
914	0.119	0.117	0.121	0.121
923	0.119	0.117	0.121	0.122
932	0.120	0.118	0.122	0.122
941	0.119	0.117	0.121	0.121
950	0.120	0.118	0.122	0.121
959	0.120	0.118	0.122	0.122
968	0.120	0.118	0.122	0.121
977	0.120	0.118	0.122	0.122
986	0.120	0.118	0.122	0.123
995	0.121	0.119	0.122	0.124
1004	0.121	0.119	0.122	0.123
1013	0.122	0.120	0.124	0.123
1022	0.123	0.121	0.125	0.124
1031	0.123	0.122	0.126	0.124
1040	0.124	0.123	0.126	0.125
1049	0.125	0.123	0.126	0.126
1058	0.125	0.123	0.126	0.126
1067	0.125	0.122	0.127	0.126
1076	0.124	0.123	0.127	0.127
1085	0.125	0.123	0.127	0.128
1094	0.125	0.123	0.126	0.127
1103	0.126	0.124	0.128	0.128
1112	0.128	0.125	0.129	0.130
1121	0.129	0.126	0.131	0.131
1130	0.129	0.128	0.132	0.131
1139	0.130	0.130	0.134	0.134
1148	0.131	0.130	0.134	0.135
1157	0.133	0.131	0.135	0.135
1166	0.133	0.130	0.135	0.134
1175	0.134	0.133	0.136	0.136
1184	0.136	0.134	0.137	0.138
1193	0.134	0.133	0.136	0.136
1202	0.135	0.132	0.136	0.136
1211	0.136	0.134	0.138	0.138
1220	0.137	0.134	0.139	0.139
1229	0.137	0.135	0.139	0.140
1238	0.138	0.137	0.139	0.139
1247	0.140	0.136	0.140	0.140
1256	0.140	0.138	0.142	0.142
1265	0.139	0.137	0.142	0.140
1274	0.141	0.138	0.144	0.143
1283	0.141	0.139	0.145	0.144
1292	0.143	0.142	0.144	0.145
1301	0.142	0.139	0.143	0.144
1310	0.142	0.139	0.142	0.145
1319	0.143	0.141	0.145	0.145
1328	0.145	0.143	0.148	0.148
1337	0.146	0.143	0.149	0.148
1346	0.148	0.146	0.150	0.153
1355	0.145	0.144	0.149	0.148
1364	0.150	0.149	0.151	0.153
1373	0.148	0.146	0.148	0.152
1382	0.151	0.149	0.153	0.154
1391	0.149	0.149	0.150	0.154

Appendix 2—Tabulated Specific Heat Results (cont.)

Temperature-F	Specific Heat (Heating Data)-BTU/lbF			
SpecID	2-L2-1	2-L2-2	T7-1-1	T7-1-2
Disk	Supersolvus	Supersolvus	Subsolvus	Subsolvus
1769	0.206	0.203	0.203	0.202
1778	0.213	0.207	0.210	0.210
1787	0.209	0.213	0.215	0.208
1796	0.210	0.217	0.213	0.210
1805	0.208	0.208	0.213	0.208
1814	0.224	0.220	0.219	0.220
1823	0.217	0.211	0.219	0.213
1832	0.218	0.216	0.227	0.217
1841	0.215	0.215	0.225	0.219
1850	0.225	0.224	0.228	0.226
1859	0.229	0.222	0.229	0.225
1868	0.223	0.223	0.222	0.220
1877	0.230	0.224	0.228	0.227
1886	0.229	0.226	0.230	0.231
1895	0.235	0.237	0.239	0.232
1904	0.230	0.234	0.233	0.226
1913	0.235	0.235	0.232	0.232
1922	0.239	0.239	0.245	0.238
1931	0.245	0.245	0.248	0.242
1940	0.256	0.251	0.255	0.250
1949	0.251	0.250	0.253	0.257
1958	0.245	0.250	0.243	0.252
1967	0.264	0.258	0.267	0.255
1976	0.259	0.265	0.259	0.253
1985	0.264	0.263	0.261	0.249
1994	0.268	0.270	0.275	0.257
2003	0.272	0.275	0.275	0.266
2012	0.265	0.279	0.273	0.275
2021	0.264	0.271	0.272	0.266
2030	0.279	0.276	0.283	0.275
2039	0.287	0.287	0.287	0.285
2048	0.289	0.290	0.289	0.284
2057	0.297	0.294	0.292	0.274
2066	0.292	0.285	0.270	0.252
2075	0.302	0.297	0.253	0.246
2084	0.310	0.316	0.248	0.256
2093	0.291	0.292	0.233	0.238
2102	0.293	0.292	0.262	0.250
2111	0.231	0.227	0.271	0.258
2120	0.196	0.204	0.263	0.260
2129	0.183	0.192	0.256	0.249
2138	0.183	0.178	0.235	0.233
2147	0.172	0.170	0.209	0.210
2156	0.174	0.176	0.207	0.201
2165	0.178	0.189	0.207	0.204
2174	0.178	0.182	0.198	0.186
2183	0.220	0.221	0.237	0.229
2192	0.252	0.251	0.260	0.260

Temperature-F	Specific Heat (Cooling Data)-BTU/lbF			
SpecID	2-L2-1	2-L2-2	T7-1-1	T7-1-2
Disk	Supersolvus	Supersolvus	Subsolvus	Subsolvus
1400	0.149	0.148	0.153	0.153
1409	0.151	0.151	0.154	0.156
1418	0.150	0.149	0.156	0.152
1427	0.159	0.154	0.162	0.160
1436	0.149	0.151	0.155	0.154
1445	0.157	0.155	0.155	0.161
1454	0.156	0.153	0.157	0.160
1463	0.157	0.156	0.160	0.158
1472	0.156	0.157	0.163	0.160
1481	0.156	0.155	0.160	0.160
1490	0.161	0.159	0.162	0.162
1499	0.163	0.161	0.163	0.164
1508	0.164	0.164	0.166	0.167
1517	0.156	0.156	0.157	0.162
1526	0.162	0.159	0.164	0.166
1535	0.163	0.159	0.161	0.169
1544	0.168	0.162	0.167	0.169
1553	0.168	0.161	0.171	0.170
1562	0.169	0.167	0.172	0.172
1571	0.166	0.164	0.166	0.170
1580	0.162	0.160	0.163	0.167
1589	0.163	0.168	0.172	0.170
1598	0.167	0.169	0.168	0.171
1607	0.167	0.167	0.168	0.172
1616	0.169	0.171	0.177	0.177
1625	0.169	0.169	0.170	0.172
1634	0.170	0.168	0.172	0.174
1643	0.173	0.171	0.175	0.177
1652	0.171	0.169	0.172	0.172
1661	0.177	0.177	0.178	0.177
1670	0.171	0.175	0.174	0.177
1679	0.178	0.180	0.185	0.185
1688	0.176	0.178	0.183	0.182
1697	0.183	0.179	0.182	0.180
1706	0.184	0.184	0.188	0.187
1715	0.184	0.186	0.189	0.186
1724	0.180	0.181	0.184	0.183
1733	0.184	0.186	0.186	0.189
1742	0.194	0.191	0.201	0.197
1751	0.192	0.187	0.192	0.188
1760	0.198	0.197	0.199	0.201
1769	0.192	0.195	0.199	0.199
1778	0.198	0.196	0.199	0.202
1787	0.201	0.199	0.198	0.202
1796	0.201	0.198	0.205	0.208
1805	0.205	0.206	0.202	0.209
1814	0.204	0.204	0.207	0.207
1823	0.205	0.203	0.212	0.216
1832	0.206	0.203	0.206	0.211
1841	0.218	0.216	0.220	0.222
1850	0.209	0.213	0.211	0.220
1859	0.213	0.213	0.219	0.218
1868	0.221	0.218	0.224	0.225
1877	0.219	0.220	0.223	0.226
1886	0.231	0.233	0.234	0.239
1895	0.224	0.224	0.232	0.227

Appendix 2—Tabulated Specific Heat Results (cont.)

Temperature-F	Specific Heat (Cooling Data)-BTU/lbF			
SpecID	2-L2-1	2-L2-2	T7-1-1	T7-1-2
Disk	Supersolvus	Supersolvus	Subsolvus	Subsolvus
1904	0.229	0.232	0.238	0.232
1913	0.227	0.225	0.224	0.233
1922	0.239	0.236	0.236	0.246
1931	0.251	0.250	0.257	0.260
1940	0.239	0.239	0.239	0.241
1949	0.253	0.251	0.247	0.252
1958	0.274	0.269	0.272	0.272
1967	0.261	0.262	0.268	0.262
1976	0.267	0.273	0.273	0.273
1985	0.283	0.292	0.297	0.300
1994	0.308	0.309	0.313	0.322
2003	0.322	0.327	0.333	0.333
2012	0.376	0.373	0.389	0.394
2021	0.388	0.392	0.397	0.399
2030	0.321	0.315	0.325	0.334
2039	0.176	0.174	0.187	0.188
2048	0.168	0.163	0.169	0.174
2057	0.169	0.164	0.168	0.176
2066	0.171	0.167	0.172	0.176
2075	0.175	0.177	0.167	0.178
2084	0.166	0.168	0.173	0.176
2093	0.173	0.171	0.169	0.179
2102	0.175	0.175	0.181	0.178
2111	0.179	0.170	0.181	0.179
2120	0.179	0.182	0.177	0.181
2129	0.175	0.174	0.174	0.175
2138	0.174	0.173	0.173	0.178
2147	0.189	0.176	0.186	0.198
2156	0.177	0.178	0.186	0.195
2165	0.189	0.184	0.185	0.188
2174	0.188	0.188	0.192	0.198
2183	0.195	0.196	0.203	0.200
2192	0.190	0.178	0.189	0.194

Appendix 3—Tabulated Thermal Conductivity Results

Temperature-F	Thermal Conductivity-BTU/(hr ft F)			
SpecID	2-L2-1	2-L2-2	T7-1-1	T7-1-2
Disk	Supersolvus	Supersolvus	Subsolvus	Subsolvus
73	5.455	5.425	5.558	5.578
122	5.683	5.713	5.825	5.755
212	6.132	6.146	6.321	6.259
392	7.138	7.039	7.179	7.070
572	7.896	7.764	7.983	7.812
752	8.692	8.614	8.644	8.463
932	9.508	9.473	9.488	9.257
1112	10.559	10.410	10.414	10.519
1292	11.550	11.546	11.562	11.471
1472	13.246	13.064	12.734	12.907
1652	13.676	13.587	13.482	13.342
1832	14.437	14.348	14.097	14.382
2012	15.187	14.965	14.987	15.032
2192	16.396	16.480	16.374	16.279

Appendix 4—Tabulated Thermal Expansion Results

Temperature-F	Thermal Expansion (Heating Data)-in/in			
SpecID	2-L2-1	2-L2-2	T7-1-1	T7-1-2
Disk	Supersolvus	Supersolvus	Subsolvus	Subsolvus
68	0.00000	0.00000	0.00000	0.00000
86	0.00013	0.00012	0.00012	0.00012
104	0.00025	0.00025	0.00025	0.00024
122	0.00037	0.00037	0.00037	0.00037
140	0.00050	0.00050	0.00049	0.00049
158	0.00062	0.00062	0.00061	0.00061
176	0.00074	0.00074	0.00073	0.00073
194	0.00087	0.00086	0.00086	0.00086
212	0.00099	0.00099	0.00099	0.00098
230	0.00112	0.00112	0.00111	0.00111
248	0.00124	0.00124	0.00124	0.00123
266	0.00137	0.00137	0.00137	0.00136
284	0.00150	0.00150	0.00149	0.00149
302	0.00163	0.00163	0.00162	0.00162
320	0.00176	0.00176	0.00175	0.00175
338	0.00189	0.00189	0.00188	0.00187
356	0.00202	0.00202	0.00201	0.00200
374	0.00215	0.00215	0.00214	0.00214
392	0.00228	0.00228	0.00228	0.00227
410	0.00241	0.00241	0.00241	0.00240
428	0.00254	0.00254	0.00254	0.00253
446	0.00268	0.00268	0.00267	0.00266
464	0.00281	0.00281	0.00281	0.00280
482	0.00295	0.00295	0.00294	0.00293
500	0.00308	0.00308	0.00308	0.00307
518	0.00321	0.00322	0.00321	0.00320
536	0.00335	0.00335	0.00335	0.00334
554	0.00349	0.00349	0.00348	0.00348
572	0.00362	0.00363	0.00362	0.00361
590	0.00376	0.00377	0.00376	0.00375
608	0.00389	0.00390	0.00390	0.00389
626	0.00403	0.00404	0.00404	0.00403
644	0.00417	0.00418	0.00418	0.00417
662	0.00431	0.00432	0.00432	0.00431
680	0.00446	0.00446	0.00446	0.00445
698	0.00460	0.00460	0.00460	0.00459
716	0.00474	0.00474	0.00474	0.00473
734	0.00488	0.00489	0.00488	0.00487
752	0.00502	0.00503	0.00503	0.00502
770	0.00517	0.00517	0.00517	0.00516
788	0.00531	0.00532	0.00531	0.00530
806	0.00545	0.00546	0.00546	0.00545
824	0.00560	0.00561	0.00560	0.00559
842	0.00574	0.00575	0.00575	0.00574
860	0.00589	0.00590	0.00589	0.00589
878	0.00603	0.00604	0.00604	0.00603
896	0.00618	0.00619	0.00619	0.00617
914	0.00633	0.00633	0.00633	0.00632
932	0.00647	0.00648	0.00648	0.00646
950	0.00662	0.00662	0.00662	0.00661
968	0.00676	0.00676	0.00676	0.00675
986	0.00690	0.00691	0.00691	0.00690
1004	0.00705	0.00705	0.00705	0.00704
1022	0.00719	0.00720	0.00720	0.00719
1040	0.00734	0.00734	0.00735	0.00734
1058	0.00750	0.00750	0.00751	0.00749

Temperature-F	Thermal Expansion (Cooling Data)-in/in			
SpecID	2-L2-1	2-L2-2	T7-1-1	T7-1-2
Disk	Supersolvus	Supersolvus	Subsolvus	Subsolvus
2192	0.02245	0.02210	0.02192	0.02209
2174	0.02221	0.02180	0.02167	0.02182
2156	0.02195	0.02150	0.02140	0.02155
2138	0.02170	0.02124	0.02115	0.02130
2120	0.02146	0.02100	0.02092	0.02106
2102	0.02123	0.02076	0.02069	0.02083
2084	0.02098	0.02051	0.02045	0.02058
2066	0.02068	0.02021	0.02016	0.02028
2048	0.02032	0.01986	0.01981	0.01992
2030	0.01991	0.01947	0.01942	0.01953
2012	0.01945	0.01904	0.01897	0.01907
1994	0.01897	0.01856	0.01850	0.01858
1976	0.01857	0.01813	0.01808	0.01816
1958	0.01819	0.01775	0.01771	0.01778
1940	0.01783	0.01738	0.01735	0.01742
1922	0.01747	0.01703	0.01701	0.01707
1904	0.01713	0.01669	0.01667	0.01673
1886	0.01680	0.01636	0.01634	0.01640
1868	0.01648	0.01604	0.01602	0.01607
1850	0.01617	0.01573	0.01571	0.01576
1832	0.01586	0.01543	0.01541	0.01546
1814	0.01557	0.01514	0.01511	0.01516
1796	0.01528	0.01485	0.01483	0.01488
1778	0.01500	0.01457	0.01455	0.01460
1760	0.01473	0.01430	0.01427	0.01433
1742	0.01447	0.01403	0.01401	0.01406
1724	0.01421	0.01377	0.01375	0.01380
1706	0.01395	0.01352	0.01349	0.01355
1688	0.01370	0.01328	0.01325	0.01330
1670	0.01346	0.01304	0.01301	0.01306
1652	0.01323	0.01280	0.01277	0.01283
1634	0.01300	0.01257	0.01254	0.01260
1616	0.01277	0.01235	0.01232	0.01238
1598	0.01255	0.01213	0.01210	0.01216
1580	0.01233	0.01191	0.01188	0.01194
1562	0.01211	0.01170	0.01167	0.01173
1544	0.01190	0.01149	0.01146	0.01152
1526	0.01169	0.01128	0.01125	0.01131
1508	0.01148	0.01108	0.01105	0.01111
1490	0.01128	0.01088	0.01085	0.01091
1472	0.01107	0.01068	0.01065	0.01071
1454	0.01087	0.01048	0.01045	0.01052
1436	0.01067	0.01028	0.01026	0.01033
1418	0.01043	0.01009	0.01007	0.01014
1400	0.01023	0.00990	0.00988	0.00996
1382	0.01010	0.00971	0.00969	0.00977
1364	0.00991	0.00952	0.00951	0.00959
1346	0.00973	0.00933	0.00933	0.00941
1328	0.00955	0.00915	0.00915	0.00924
1310	0.00937	0.00897	0.00897	0.00906
1292	0.00919	0.00879	0.00880	0.00889
1274	0.00901	0.00861	0.00862	0.00871
1256	0.00883	0.00843	0.00844	0.00854
1238	0.00866	0.00825	0.00827	0.00837
1220	0.00848	0.00808	0.00810	0.00820
1202	0.00831	0.00790	0.00792	0.00803

Appendix 4—Tabulated Thermal Expansion Results (cont.)

Temperature-F	Thermal Expansion (Heating Data)-in/in			
SpecID	2-L2-1	2-L2-2	T7-1-1	T7-1-2
Disk	Supersolvus	Supersolvus	Subsolvus	Subsolvus
1076	0.00765	0.00765	0.00767	0.00765
1094	0.00782	0.00781	0.00783	0.00781
1112	0.00798	0.00798	0.00799	0.00797
1130	0.00815	0.00814	0.00816	0.00814
1148	0.00832	0.00831	0.00832	0.00830
1166	0.00848	0.00848	0.00849	0.00846
1184	0.00866	0.00865	0.00865	0.00863
1202	0.00883	0.00882	0.00882	0.00879
1220	0.00900	0.00899	0.00899	0.00896
1238	0.00917	0.00916	0.00915	0.00912
1256	0.00934	0.00933	0.00931	0.00929
1274	0.00951	0.00949	0.00948	0.00945
1292	0.00968	0.00966	0.00964	0.00961
1310	0.00985	0.00982	0.00980	0.00978
1328	0.01002	0.00999	0.00996	0.00995
1346	0.01019	0.01016	0.01013	0.01012
1364	0.01037	0.01033	0.01031	0.01030
1382	0.01055	0.01051	0.01049	0.01049
1400	0.01073	0.01069	0.01068	0.01069
1418	0.01092	0.01087	0.01088	0.01090
1436	0.01111	0.01107	0.01109	0.01111
1454	0.01132	0.01127	0.01130	0.01134
1472	0.01153	0.01148	0.01152	0.01158
1490	0.01174	0.01170	0.01174	0.01182
1508	0.01197	0.01192	0.01197	0.01206
1526	0.01219	0.01214	0.01221	0.01231
1544	0.01242	0.01237	0.01245	0.01257
1562	0.01266	0.01261	0.01269	0.01282
1580	0.01290	0.01285	0.01294	0.01308
1598	0.01314	0.01309	0.01319	0.01334
1616	0.01339	0.01334	0.01344	0.01360
1634	0.01364	0.01359	0.01369	0.01386
1652	0.01389	0.01384	0.01395	0.01412
1670	0.01415	0.01409	0.01422	0.01439
1688	0.01440	0.01435	0.01449	0.01466
1706	0.01467	0.01462	0.01476	0.01493
1724	0.01494	0.01489	0.01504	0.01521
1742	0.01521	0.01517	0.01533	0.01549
1760	0.01549	0.01544	0.01561	0.01577
1778	0.01578	0.01573	0.01590	0.01605
1796	0.01607	0.01602	0.01619	0.01634
1814	0.01637	0.01632	0.01648	0.01662
1832	0.01667	0.01662	0.01677	0.01691
1850	0.01698	0.01693	0.01707	0.01721
1868	0.01730	0.01725	0.01737	0.01751
1886	0.01762	0.01757	0.01768	0.01782
1904	0.01795	0.01789	0.01800	0.01814
1922	0.01830	0.01823	0.01832	0.01846
1940	0.01864	0.01857	0.01864	0.01879
1958	0.01900	0.01892	0.01896	0.01912
1976	0.01937	0.01928	0.01929	0.01946
1994	0.01975	0.01965	0.01962	0.01980
2012	0.02013	0.02003	0.01993	0.02013
2030	0.02053	0.02042	0.02023	0.02043
2048	0.02093	0.02081	0.02050	0.02068

Temperature-F	Thermal Expansion (Cooling Data)-in/in			
SpecID	2-L2-1	2-L2-2	T7-1-1	T7-1-2
Disk	Supersolvus	Supersolvus	Subsolvus	Subsolvus
1184	0.00813	0.00773	0.00775	0.00786
1166	0.00796	0.00755	0.00758	0.00769
1148	0.00779	0.00739	0.00741	0.00753
1130	0.00763	0.00722	0.00725	0.00736
1112	0.00746	0.00705	0.00708	0.00720
1094	0.00729	0.00688	0.00692	0.00703
1076	0.00713	0.00672	0.00675	0.00687
1058	0.00707	0.00656	0.00659	0.00671
1040	0.00691	0.00640	0.00643	0.00656
1022	0.00676	0.00626	0.00627	0.00642
1004	0.00661	0.00613	0.00612	0.00627
986	0.00646	0.00599	0.00596	0.00612
968	0.00632	0.00585	0.00583	0.00597
950	0.00617	0.00571	0.00568	0.00582
932	0.00603	0.00558	0.00555	0.00567
914	0.00589	0.00545	0.00541	0.00555
896	0.00575	0.00532		0.00540
878	0.00561	0.00519		0.00525
860	0.00547	0.00505		0.00511
842	0.00533	0.00492		0.00500
824	0.00519	0.00478		0.00487
806	0.00505	0.00464		0.00473
788	0.00492	0.00452		0.00461
770	0.00479	0.00438		0.00448
752	0.00466	0.00425		0.00436
734	0.00453	0.00412		0.00423
716	0.00439	0.00398		0.00411
698	0.00427	0.00385		0.00399
680	0.00414	0.00372		0.00386
662	0.00403	0.00359		0.00373
644	0.00390	0.00346		0.00362
626	0.00377	0.00332		0.00350
608	0.00364	0.00319		0.00338
590	0.00351	0.00305		0.00326
572	0.00338	0.00292		0.00313
554	0.00325	0.00279		0.00301
536	0.00312	0.00266		0.00289
518	0.00300	0.00253		0.00278
500	0.00287	0.00240		0.00265
482	0.00275	0.00227		0.00253
464	0.00263	0.00215		0.00241
446	0.00250	0.00202		0.00229
428	0.00238	0.00189		0.00217
410	0.00226	0.00176		0.00207
392	0.00214	0.00163		0.00202
72	-0.00020	-0.00055	-0.00015	-0.00022

Appendix 4—Tabulated Thermal Expansion Results (cont.)

Temperature-F	Thermal Expansion (Heating Data)-in/in			
SpecID	2-L2-1	2-L2-2	T7-1-1	T7-1-2
Disk	Supersolvus	Supersolvus	Subsolvus	Subsolvus
2066	0.02129	0.02115	0.02077	0.02094
2084	0.02161	0.02145	0.02102	0.02119
2102	0.02188	0.02172	0.02124	0.02140
2120	0.02211	0.02193	0.02143	0.02159
2138	0.02227	0.02208	0.02159	0.02177
2156	0.02241	0.02218	0.02176	0.02193
2174	0.02252	0.02225	0.02190	0.02206
2192	0.02260	0.02230	0.02202	0.02217

Appendix 5—Tabulated Instantaneous CTE Results

Temperature-F	Instantaneous CTE-μin/inF			
SpecID	2-L2-1	2-L2-2	T7-1-1	T7-1-2
Disk	Supersolvus	Supersolvus	Subsolvus	Subsolvus
212	6.98726	7.03407	6.95703	6.94125
230	6.96631	6.95631	6.97119	7.01381
248	7.03745	7.00040	7.07160	6.98049
266	7.09225	7.11513	7.12332	7.07372
284	7.16599	7.17022	7.14482	7.15031
302	7.17642	7.19646	7.19831	7.24454
320	7.15570	7.15869	7.15843	7.13385
338	7.15034	7.13390	7.14249	7.11194
356	7.29233	7.30506	7.28662	7.31976
374	7.29257	7.38488	7.36074	7.40441
392	7.30056	7.32376	7.33042	7.27966
410	7.42643	7.33586	7.33594	7.27768
428	7.31055	7.34466	7.34379	7.33410
446	7.39844	7.42278	7.44467	7.40823
464	7.49748	7.46269	7.49382	7.49371
482	7.44904	7.48688	7.48125	7.47477
500	7.48294	7.52290	7.48005	7.49062
518	7.49366	7.49433	7.51715	7.51941
536	7.52453	7.60425	7.58845	7.59291
554	7.56871	7.69358	7.66128	7.64905
572	7.57020	7.66833	7.66255	7.65485
590	7.56085	7.66273	7.64120	7.61606
608	7.66544	7.67680	7.67255	7.64129
626	7.78610	7.74223	7.75006	7.76198
644	7.79704	7.75238	7.82334	7.80810
662	7.83128	7.76720	7.84406	7.80140
680	7.83495	7.77079	7.84005	7.79205
698	7.80558	7.79140	7.83706	7.83448
716	7.85614	7.93054	7.92626	7.91703
734	7.92935	7.95699	7.92269	7.95387
752	7.97744	7.92793	7.92730	7.95413
770	7.96788	7.95324	7.99494	7.98510
788	7.94922	8.00462	8.00019	7.97000
806	8.04092	8.05826	8.04179	8.03275
824	8.08813	8.07300	8.08875	8.11680
842	8.05622	8.08464	8.08338	8.10558
860	8.08247	8.08322	8.08945	8.08671
878	8.06685	8.07609	8.05277	8.06528
896	8.10921	8.10590	8.07360	8.04410
914	8.12787	8.05778	8.10277	8.03815
932	8.05892	7.99768	8.02255	7.99635
950	8.02662	7.96211	7.99932	7.96916
968	7.96131	7.89960	7.95912	7.96982
986	7.98931	7.94253	7.99971	8.00598
1004	8.04274	8.03480	8.14460	8.10403
1022	8.16194	8.14151	8.29005	8.25086
1040	8.37805	8.32607	8.48794	8.45616
1058	8.62890	8.62694	8.72552	8.68731
1076	8.89359	8.88079	8.92331	8.87758
1094	9.13335	9.05494	9.04766	8.95398
1112	9.26923	9.16097	9.12374	9.04773
1130	9.26800	9.23081	9.17013	9.05959
1148	9.32132	9.32455	9.17401	9.06821
1166	9.47562	9.42839	9.28167	9.19418
1184	9.58695	9.49854	9.31228	9.22201

Appendix 5—Tabulated Instantaneous CTE Results (cont.)

Temperature-F	Instantaneous CTE-μin/inF			
SpecID	2-L2-1	2-L2-2	T7-1-1	T7-1-2
Disk	Supersolvus	Supersolvus	Subsolvus	Subsolvus
1202	9.55570	9.45880	9.22277	9.17044
1220	9.57168	9.37706	9.16853	9.12909
1238	9.53957	9.32468	9.07874	9.11609
1256	9.44352	9.31443	9.03066	9.08024
1274	9.45663	9.20248	8.93042	9.07259
1292	9.43171	9.18381	8.84093	9.15518
1310	9.38744	9.21860	9.02055	9.25260
1328	9.45401	9.25158	9.28952	9.43758
1346	9.62612	9.47403	9.60874	9.80657
1364	9.85049	9.66987	10.03726	10.29517
1382	10.01446	9.88603	10.44094	10.70326
1400	10.26361	10.19375	10.83220	11.29215
1418	10.62239	10.55181	11.27237	11.87895
1436	11.06261	10.99749	11.68117	12.32215
1454	11.51301	11.44760	11.96238	12.88640
1472	11.82610	11.79393	12.29177	13.26183
1490	12.19246	12.16284	12.60267	13.50977
1508	12.38156	12.43819	12.89106	13.78050
1526	12.75945	12.72550	13.13192	14.01451
1544	13.11016	13.04251	13.40296	14.20645
1562	13.26350	13.18762	13.63933	14.24593
1580	13.44390	13.39252	13.75482	14.26831
1598	13.56107	13.52976	13.95597	14.38600
1616	13.75714	13.73964	14.12772	14.55959
1634	13.87710	13.94656	14.35144	14.56149
1652	14.09056	14.07432	14.55704	14.69275
1670	14.26619	14.25999	14.83210	14.93051
1688	14.46715	14.50611	15.09443	15.06271
1706	14.81191	14.86748	15.38813	15.28897
1724	15.19850	15.15608	15.76943	15.50484
1742	15.39910	15.46360	15.88844	15.58414
1760	15.67551	15.77489	15.84535	15.69881
1778	16.00837	16.05228	15.98817	15.71424
1796	16.32033	16.39528	16.09377	15.76221
1814	16.65580	16.67448	16.15512	16.03647
1832	17.12463	16.95861	16.41685	16.27884
1850	17.50464	17.29777	16.68638	16.60441
1868	17.66952	17.60236	17.00183	16.97019
1886	18.21630	18.07047	17.38981	17.31644
1904	18.81093	18.36966	17.62387	17.75802
1922	19.12722	18.63620	17.76382	18.11358
1940	19.64027	19.28404	17.85471	18.36380
1958	20.23020	19.73537	18.12981	18.55184
1976	20.68488	20.20276	18.45650	18.95587
1994	21.16618	20.91525	18.04515	18.89172
2012	21.64171	21.51263	16.91584	17.66648
2030	22.44449	22.02825	15.50050	15.02985
2048	21.60569	20.43019	15.20538	14.13186
2066	18.72114	17.61270	14.72262	14.27746
2084	16.15604	15.71210	13.08115	12.91224
2102	14.07457	13.52167	11.17095	11.01422
2120	10.78872	9.93061	9.36475	9.85164
2138	8.20523	6.86235	9.20720	9.62396
2156	6.84959	4.72670	8.64562	8.19074
2174	5.82714	3.31262	7.58576	7.04136
2192	6.63331	4.39647	8.53914	8.05148

Appendix 6—Tabulated Mean CTE Results

Temperature-F	Mean CTE-μin/inF			
SpecID	2-L2-1	2-L2-2	T7-1-1	T7-1-2
Disk	Supersolvus	Supersolvus	Subsolvus	Subsolvus
212	6.90090	6.89242	6.85555	6.81599
230	6.90712	6.90317	6.86834	6.84078
248	6.91704	6.90931	6.88162	6.85220
266	6.93033	6.92299	6.90373	6.87002
284	6.94676	6.94192	6.92111	6.88870
302	6.96492	6.96027	6.94160	6.91353
320	6.97884	6.97673	6.95848	6.93459
338	6.99072	6.98705	6.97108	6.94499
356	7.00339	7.00050	6.98487	6.96157
374	7.02334	7.02260	7.00675	6.98657
392	7.03575	7.04060	7.02472	7.00687
410	7.05454	7.05560	7.04144	7.01964
428	7.07077	7.07007	7.05589	7.03491
446	7.08224	7.08425	7.07173	7.04991
464	7.10068	7.10155	7.09043	7.06899
482	7.11621	7.11693	7.10754	7.08698
500	7.13085	7.13381	7.12316	7.10330
518	7.14523	7.14857	7.13786	7.11944
536	7.15903	7.16335	7.15390	7.13589
554	7.17349	7.18204	7.17126	7.15428
572	7.18778	7.19385	7.18927	7.17194
590	7.20074	7.21581	7.20489	7.18828
608	7.21394	7.23093	7.21999	7.20228
626	7.23087	7.24611	7.23556	7.21853
644	7.24854	7.26230	7.25307	7.23647
662	7.26542	7.27685	7.27065	7.25373
680	7.28251	7.29188	7.28759	7.26968
698	7.29766	7.30526	7.30321	7.28499
716	7.31232	7.32072	7.31897	7.30143
734	7.32805	7.33802	7.33603	7.31874
752	7.34457	7.35373	7.35084	7.33545
770	7.36085	7.36875	7.36688	7.35159
788	7.37567	7.38393	7.38253	7.36754
806	7.39046	7.39978	7.39807	7.38241
824	7.40697	7.41573	7.41397	7.39937
842	7.42230	7.43107	7.42979	7.41582
860	7.43693	7.44603	7.44448	7.43141
878	7.45133	7.46001	7.45878	7.44562
896	7.46475	7.47369	7.47137	7.45896
914	7.47913	7.48693	7.48498	7.47120
932	7.49177	7.49795	7.49692	7.48284
950	7.50305	7.50794	7.50731	7.49274
968	7.51295	7.51634	7.51690	7.50247
986	7.52165	7.52400	7.52558	7.51169
1004	7.53143	7.53305	7.53614	7.52225
1022	7.54174	7.54338	7.54895	7.53437
1040	7.55538	7.55607	7.56439	7.54959
1058	7.57237	7.57255	7.58333	7.56805
1076	7.59380	7.59403	7.60562	7.58997
1094	7.61858	7.61799	7.62991	7.61332
1112	7.64627	7.64400	7.65506	7.63710
1130	7.67376	7.67010	7.68038	7.66147
1148	7.70064	7.69702	7.70533	7.68452
1166	7.72834	7.72440	7.72993	7.70824
1184	7.75765	7.75268	7.75574	7.73267

Appendix 6—Tabulated Mean CTE Results (cont.)

Temperature-F	Mean CTE-μin/inF			
SpecID	2-L2-1	2-L2-2	T7-1-1	T7-1-2
Disk	Supersolvus	Supersolvus	Subsolvus	Subsolvus
1202	7.78658	7.78013	7.77953	7.75587
1220	7.81410	7.80578	7.80176	7.77766
1238	7.84125	7.82942	7.82209	7.79827
1256	7.86607	7.85201	7.84067	7.81810
1274	7.88962	7.87324	7.85790	7.83669
1292	7.91265	7.89221	7.87279	7.85544
1310	7.93423	7.91148	7.88771	7.87498
1328	7.95533	7.93011	7.90601	7.89579
1346	7.97754	7.95012	7.92745	7.91987
1364	8.00198	7.97287	7.95380	7.94942
1382	8.02859	7.99735	7.98514	7.98457
1400	8.05680	8.02499	8.02098	8.02468
1418	8.08879	8.05615	8.06127	8.07276
1436	8.12472	8.09188	8.10640	8.12549
1454	8.16605	8.13256	8.15475	8.18364
1472	8.21100	8.17749	8.20549	8.24674
1490	8.25894	8.22546	8.25940	8.31167
1508	8.30978	8.27675	8.31532	8.37841
1526	8.36153	8.32953	8.37356	8.44655
1544	8.41818	8.38537	8.43293	8.51570
1562	8.47517	8.44241	8.49459	8.58472
1580	8.53364	8.49994	8.55642	8.65207
1598	8.59185	8.55861	8.61870	8.71883
1616	8.65086	8.61721	8.68187	8.78563
1634	8.71029	8.67769	8.74555	8.85243
1652	8.77000	8.73804	8.81065	8.91741
1670	8.83105	8.79918	8.87642	8.98407
1688	8.89224	8.86097	8.94440	9.05065
1706	8.95545	8.92503	9.01320	9.11801
1724	9.02108	8.99129	9.08479	9.18623
1742	9.08903	9.05909	9.15754	9.25486
1760	9.15707	9.12901	9.22898	9.32249
1778	9.22788	9.20037	9.29900	9.39016
1796	9.29975	9.27348	9.36965	9.45578
1814	9.37419	9.34850	9.43896	9.52232
1832	9.45034	9.42454	9.50881	9.58998
1850	9.53045	9.50242	9.57995	9.65910
1868	9.61073	9.58189	9.65252	9.73040
1886	9.69290	9.66335	9.72716	9.80381
1904	9.77960	9.74778	9.80372	9.87946
1922	9.86903	9.83233	9.88019	9.95797
1940	9.96001	9.91993	9.95664	10.03747
1958	10.05539	10.01173	10.03269	10.11788
1976	10.15337	10.10520	10.11099	10.19881
1994	10.25415	10.20238	10.18780	10.28156
2012	10.35730	10.30503	10.25566	10.35613
2030	10.46408	10.41020	10.31039	10.41273
2048	10.57200	10.51167	10.35449	10.44653
2066	10.65862	10.58708	10.39795	10.48279
2084	10.71844	10.64119	10.42906	10.51041
2102	10.75733	10.67689	10.44463	10.52419
2120	10.77377	10.68759	10.44240	10.52148
2138	10.76002	10.66550	10.43070	10.51520
2156	10.73301	10.62430	10.41991	10.50251
2174	10.69411	10.56609	10.39876	10.47627
2192	10.63977	10.49746	10.36599	10.43733

Appendix 7—Tabulated Young's Modulus Results

Temperature-F	Young's Modulus-Msi							
SpecID	T7-2-M1L	T7-2-M1S	T7-2-M2L	T7-2-M2S	T7-2-M3L	T7-2-M3S	T7-2-M4L	T7-2-M4S
81	32.62	33.10	32.61	32.91	32.27	32.80	32.59	32.94
86	32.61	33.10	32.59	32.86	32.26	32.75	32.60	32.94
104	32.52	32.97	32.52	32.75	32.18	32.65	32.52	32.79
122	32.42	32.79	32.41	32.60	32.08	32.49	32.42	32.65
140	32.31	32.67	32.30	32.44	31.97	32.34	32.31	32.50
158	32.18	32.55	32.19	32.29	31.85	32.19	32.18	32.36
176	32.05	32.36	32.05	32.19	31.71	32.04	32.05	32.21
194	31.93	32.24	31.93	32.03	31.59	31.94	31.90	32.07
212	31.81	32.12	31.80	31.93	31.48	31.79	31.80	31.97
230	31.69	32.06	31.69	31.83	31.38	31.69	31.68	31.83
248	31.59	31.94	31.58	31.73	31.25	31.59	31.57	31.73
266	31.48	31.82	31.47	31.63	31.16	31.49	31.46	31.64
284	31.38	31.76	31.38	31.52	31.05	31.39	31.35	31.54
302	31.28	31.64	31.27	31.42	30.95	31.29	31.26	31.45
320	31.19	31.58	31.17	31.32	30.86	31.24	31.17	31.35
338	31.10	31.46	31.09	31.22	30.77	31.14	31.07	31.26
356	30.99	31.34	30.99	31.12	30.67	31.04	30.97	31.17
374	30.91	31.28	30.89	31.07	30.58	30.94	30.87	31.07
392	30.81	31.16	30.81	30.97	30.49	30.84	30.79	30.98
410	30.73	31.10	30.71	30.87	30.40	30.74	30.69	30.88
428	30.64	30.98	30.63	30.77	30.31	30.69	30.61	30.79
446	30.56	30.92	30.54	30.72	30.23	30.59	30.51	30.74
464	30.47	30.86	30.46	30.62	30.14	30.49	30.43	30.65
482	30.38	30.75	30.37	30.52	30.06	30.45	30.34	30.55
500	30.30	30.69	30.28	30.47	29.98	30.35	30.26	30.46
518	30.21	30.57	30.19	30.37	29.88	30.25	30.18	30.37
536	30.13	30.51	30.11	30.27	29.80	30.15	30.08	30.27
554	30.05	30.39	30.03	30.22	29.72	30.10	30.00	30.23
572	29.96	30.33	29.94	30.12	29.64	30.00	29.93	30.14
590	29.88	30.27	29.86	30.02	29.56	29.91	29.84	30.04
608	29.80	30.16	29.78	29.97	29.47	29.86	29.75	29.95
626	29.70	30.10	29.68	29.87	29.39	29.76	29.65	29.86
644	29.62	29.98	29.60	29.78	29.30	29.66	29.57	29.81
662	29.52	29.92	29.51	29.68	29.20	29.57	29.49	29.72
680	29.44	29.81	29.42	29.63	29.12	29.52	29.40	29.63
698	29.37	29.75	29.34	29.53	29.04	29.42	29.31	29.53
716	29.28	29.69	29.26	29.43	28.96	29.33	29.23	29.44
734	29.19	29.57	29.18	29.38	28.88	29.28	29.14	29.40
752	29.11	29.52	29.08	29.28	28.80	29.18	29.06	29.31
770	29.03	29.40	29.01	29.19	28.72	29.08	28.98	29.21
788	28.95	29.34	28.93	29.14	28.63	29.04	28.90	29.12
806	28.86	29.23	28.82	29.04	28.54	28.94	28.80	29.03
824	28.77	29.17	28.74	28.94	28.45	28.85	28.72	28.94
842	28.68	29.06	28.66	28.85	28.36	28.75	28.63	28.89
860	28.59	29.00	28.57	28.80	28.28	28.65	28.55	28.80
878	28.51	28.88	28.49	28.70	28.20	28.61	28.46	28.71
896	28.43	28.83	28.41	28.60	28.11	28.51	28.37	28.62
914	28.33	28.77	28.33	28.51	28.03	28.42	28.28	28.53
932	28.25	28.65	28.24	28.46	27.95	28.32	28.65	28.44
950	28.17	28.60	28.15	28.36	27.87	28.27	28.12	28.35
968	28.09	28.48	28.07	28.27	27.78	28.18	28.26	28.31
986	28.00	28.40	27.99	28.22	27.70	28.08	28.18	28.22
1004	27.92	28.31	27.91	28.12	27.62	27.99		28.13
1022	27.84	28.21	27.82	27.98	27.53	27.90		28.04
1040	27.75	28.11	27.73	27.93	27.44	27.80		27.90
1058	27.64	28.01	27.62	27.79	27.35	27.71	27.82	27.81
1076	27.54	27.91	27.53	27.69	27.24	27.61		27.72

Appendix 7—Tabulated Young's Modulus Results (cont.)

Temperature-F	Young's Modulus-Msi							
SpecID	T7-2-M1L	T7-2-M1S	T7-2-M2L	T7-2-M2S	T7-2-M3L	T7-2-M3S	T7-2-M4L	T7-2-M4S
1094	27.44	27.80	27.42	27.60	27.15	27.47	27.39	27.59
1112	27.33	27.70	27.33	27.51	27.03	27.38		27.50
1130	27.23	27.59	27.21	27.36	26.93	27.29	27.18	27.41
1148	27.12	27.48	27.11	27.27	26.84	27.20	27.08	27.28
1166	27.02	27.37	27.01	27.17	26.73	27.06		27.19
1184	26.92	27.27	26.91	27.08	26.63	26.96	26.87	27.10
1202	26.81	27.15	26.80	26.99	26.52	26.87	26.76	26.97
1220	26.68	27.05	26.68	26.85	26.41	26.78	26.85	26.88
1238	26.58	26.93	26.57	26.75	26.30	26.64	26.54	26.75
1256	26.47	26.83	26.47	26.61	26.19	26.55	26.44	26.67
1274	26.37	26.72	26.36	26.52	26.08	26.46	26.32	26.54
1292	26.26	26.61	26.25	26.43	25.98	26.32	26.21	26.45
1310	26.15	26.51	26.15	26.29	25.87	26.23	26.11	26.32
1328	26.05	26.40	26.04	26.20	25.76	26.14	26.00	26.23
1346	25.94	26.30	25.93	26.10	25.66	26.00	25.90	26.10
1364	25.83	26.19	25.81	25.97	25.55	25.91	25.79	26.01
1382	25.72	26.08	25.70	25.87	25.44	25.82	25.69	25.89
1400	25.61	25.96	25.59	25.78	25.34	25.68	25.58	25.80
1418	25.48	25.84	25.47	25.64	25.22	25.59	25.46	25.67
1436	25.36	25.73	25.35	25.51	25.10	25.46	25.34	25.54
1454	25.24	25.60	25.22	25.42	24.97	25.32	25.21	25.41
1472	25.11	25.48	25.09	25.28	24.84	25.23	25.09	25.33
1490	24.98	25.36	24.96	25.14	24.71	25.10	24.96	25.20
1508	24.84	25.24	24.82	25.05	24.57	24.97	24.81	25.07
1526	24.70	25.11	24.68	24.92	24.44	24.83	24.68	24.95
1544	24.57	24.99	24.54	24.78	24.29	24.74	24.72	24.82
1562	24.43	24.86	24.59	24.65	24.17	24.57	24.58	24.69
1580		24.72	24.45	24.51	24.22	24.48		24.57
1598		24.58		24.38		24.30		24.40
1616		24.44		24.25		24.17		24.28
1634		24.29		24.11		24.04		24.11
1652		24.12		23.94		23.87		23.94
1670		23.95		23.76		23.69		23.78
1688		23.77		23.58		23.52		23.61
1706		23.58		23.41		23.35		23.45
1724		23.40		23.19		23.13		23.25
1742		23.17		22.97		22.96		23.04
1760		22.93		22.80		22.71		22.80
1778		22.69		22.59		22.45		22.60
1796		22.58		22.29		22.12		22.36
1814		21.99		21.82		21.78		22.16
1832				21.44		21.53		21.88
1850				21.28		21.00		
1868				21.07		20.71		
1886				20.78	20.40	20.51		
1904				20.53	19.83	20.23		
1922		19.28			19.27	20.03		
1940		19.11			18.70	19.75		
1958		18.92			18.37			
1976		18.63		17.85	17.89			
1994		18.21		17.75	17.56			
2012				17.63	17.11			
2019				17.64	17.07			

Appendix 8—Tabulated Tensile Results

Disk	SpecID	Av. Cooling Rate Soln to 1600F-F/min	Test Temp-F	0.2% Yield Strength-ksi	Ultimate Tensile Strength-ksi	Elongation-%	Reduction in Area-%
Supersolvus	BT1	75	1100	147.9	220.7	15.0	18
Supersolvus	BT2	70	800	146.7	217.4	20.5	25
Supersolvus	BT3	70	1300	142.3	193.5	21.3	24.5
Supersolvus	BT4	70	75	155.6	227.9	20.7	23
Supersolvus	BST	80	1500	131.8	151.6	3.9	9.5
Supersolvus	BSB	70	400	148.7	220.5	18.7	21.5
Supersolvus	WT1	105	1000	154.3	222.4	13.1	19.5
Supersolvus	WT2	97	75	162.5	232.9	23.9	26
Supersolvus	WT3	95	1200	144.7	213.0	24.7	24
Supersolvus	WT4	95	1000	148.4	215.6	19.6	21.5
Supersolvus	WT5	97	1400	145.2	177.7	11.6	15.5
Supersolvus	WT6	83	1300	146.0	194.9	15.0	18
Supersolvus	WTS	87	1100	145.3	218.5	17.9	22.2
Supersolvus	RT1	165	1100	157.1	226.5	14.0	17.5
Supersolvus	RT2	160	1400	156.9	168.7	5.8	9
Supersolvus	RT3	155	1300	149.3	192.1	9.9	14.5
Supersolvus	RT5	120	1200	150.3	220.3	14.3	18.5
Supersolvus	RT6	115	400	151.6	221.1	15.3	19.8
Supersolvus	RT7	110	800	152.6	217.5	21.3	23
Supersolvus	RT8	115	1400	142.8	168.5	10.7	18
Subsolvus	BT1	360	1100	173.4	251.4	19.7	19.5
Subsolvus	BT2	325	800	173.5	242.9	18.1	21.5
Subsolvus	BT3	325	1300	168.6	192.0	13.6	19.5
Subsolvus	BT4	360	75	186.4	253.1	20.3	26
Subsolvus	BST	450	1300	169.7	211.3	12.0	15.9
Subsolvus	BSB	500	400	179.7	247.9	18.3	19.1
Subsolvus	WT1	570	1000	172.2	241.8	19.7	18.5
Subsolvus	WT2	375	75	187.5	252.3	21.8	26
Subsolvus	WT3	350	1200	171.6	223.7	13.7	17
Subsolvus	WT4	360	1000	172.5	240.9	20.1	26.5
Subsolvus	WT5	490	1400	161.5	177.9	7.1	11
Subsolvus	WT6	360	1300	169.9	199.5	9.2	14
Subsolvus	WTS	375	1200	167.0	223	10.0	15.5
Subsolvus	RT1	725	1100	173.5	243.1	14.0	16.5
Subsolvus	RT2	600	1400	165.9	170.6	5.4	11
Subsolvus	RT3-B	400	1300	171.3	194.3	8.1	9.5
Subsolvus	RT4	590	1500	134.1	154.7	9.3	8.5
Subsolvus	RT6	420	400	174.8	241.9	18.9	25
Subsolvus	RT7	420	800	175.8	242.7	16.9	21
Subsolvus	RT8	510	1400	159.0	176.1	10.0	7.5

Appendix 9—Tabulated Notch Tensile Results

Disk	SpecID	Av. Cooling Rate Soln to 1600F-F/min	Temp-F	Ultimate Tensile Strength-ksi
Supersolvus	BNT1	78	75	266.6
Supersolvus	BNT3	80	1000	254.4
Supersolvus	BNT4	77	1300	259.4
Supersolvus	BNT5	77	1100	251.4
Supersolvus	WNT1	95	1200	245.8
Supersolvus	WNT2	85	800	256.1
Supersolvus	WNT3	83	1400	241.5
Supersolvus	WNT4	85	1100	250.9
Subsolvus	BNT1	600	75	297.5
Subsolvus	BNT2	375	400	280.3
Subsolvus	BNT3	320	1000	284.6
Subsolvus	BNT4	320	1300	252.6
Subsolvus	BNT5	420	1100	274.5
Subsolvus	WNT1	430	1200	268.6
Subsolvus	WNT2	325	800	284.5
Subsolvus	WNT3	325	1400	225.1
Subsolvus	WNT4	480	1100	284.4

Appendix 10—Tabulated creep results

Disk	SpecID	Av. Cooling Rate Soln to 1600F-F/min	Temp-F	Creep Stress-ksi	0.2% Creep Time-h	Rupture Life-h	Rupture Elongation-%	Rupture Reduction in Area-%
Supersolvus	BC1	75	1300	100	557	1691.9	7.3	9.8
Supersolvus	BC2	65	1200	135	233			
Supersolvus	WC1	115	1400	80	153			
Supersolvus	WC2	100	1300	95	710			
Supersolvus	WC3	100	1500	35	1590	2231.4	2.9	4.2
Supersolvus	WC4	110	1400	100	14.8			
Supersolvus	WC5	100	1500	50	132			
Supersolvus	WC6	100	1400	65	680			
Supersolvus	WC7	110	1500	35	935			
Supersolvus	WC8	100	1400	80	86			
Supersolvus	WC9	125	1300	125	46.6			
Supersolvus	WC10	110	1500	65	42.4	141.4	14.2	16.2
Supersolvus	WC11	110	1200	125	1347	3574.2	3.2	7.3
Supersolvus	RC1	135	1300	100	895	1881.7	5.4	8.5
Supersolvus	RC2	130	1500	50	93.6			
Supersolvus	RC3	125	1400	65	970	1849.7	4.0	5.7
Supersolvus	RC4	110	1300	110	183			
Subsolvus	BC1	685	1300	100	495.2	886.7	7.1	10.1
Subsolvus	BC2	685	1200	135	1260			
Subsolvus	WC1	650	1300	80	1380	2647.1	8.4	13.3
Subsolvus	WC2	400	1400	35	420			
Subsolvus	WC3	500	1500	35	17.7	157.1		
Subsolvus	WC4	650	1400	65	50			
Subsolvus	WC5	400	1300	80	415			
Subsolvus	WC6	520	1200	125	1616	5265	6.7	11.9
Subsolvus	WC7	725	1400	35	225			
Subsolvus	WC8	560	1200	150	202			
Subsolvus	WC9	670	1300	125	139	224	5.7	9.6
Subsolvus	WC10	425	1200	150	94.5			
Subsolvus	WC11	525	1400	100	5.7	34	5.9	11.2
Subsolvus	RC1	700	1300	100	86	671.5	9.6	14.2
Subsolvus	RC2	550	1500	50	4.3			
Subsolvus	RC3	675	1200	135	770			
Subsolvus	RC4	575	1400	65	33			

Appendix 11—Tabulated Low Cycle Fatigue Results

Disk	SpecID	Av. Cooling Rate Soln to 1600F-F/min	Temperature-F	Strain Range-%	Fatigue life-cycles
Supersolvus	BL1	87	800	1.196	3,033
Supersolvus	BL2	80	1300	0.8	6,937
Supersolvus	BL3	78	800	0.598	48,725
Supersolvus	BL4	75	800	0.598	81,939
Supersolvus	BL5	75	800	0.598	94,733
Supersolvus	BL13	75	800	0.997	8,125
Supersolvus	WL2	110	800	0.798	20,254
Supersolvus	RL2	110	800	1.192	3,150
Supersolvus	RL3	132	800	0.799	28,195
Supersolvus	RL5	130	800	0.998	6,986
Supersolvus	RL8	130	800	0.597	77,950
Supersolvus	BL6	83	1300	0.597	332,061
Supersolvus	BL7	78	1300	0.598	223,970
Supersolvus	BL8	75	1300	0.598	10,366
Supersolvus	BL9	95	1300	1.195	1,023
Supersolvus	BL11	85	1300	0.999	2,557
Supersolvus	BL12	85	1300	0.797	7,128
Supersolvus	WL3	90	1300	0.999	2,157
Supersolvus	RL1	117	1300	0.798	7,128
Supersolvus	RL4	125	1300	1.199	1,038
Supersolvus	RL7	135	1300	0.599	246,425
Subsolvus	BL1	400	800	1.199	6,586
Subsolvus	BL3	350	800	0.598	350,207
Subsolvus	BL4	275	800	0.6	572,745
Subsolvus	BL5	375	800	0.597	338,501
Subsolvus	BL13	300	800	0.998	8,134
Subsolvus	WL2	425	800	0.798	104,771
Subsolvus	RL2	440	800	1.196	8,225
Subsolvus	RL3	550	800	0.8	68,356
Subsolvus	RL5	550	800	0.999	7,547
Subsolvus	RL8	520	800	0.596	307,903
Subsolvus	BL2	300	1300	0.798	44,737
Subsolvus	BL6	325	1300	0.6	9,529,316
Subsolvus	BL7	275	1300	0.594	916,939
Subsolvus	BL8	350	1300	0.597	2,557,193
Subsolvus	BL9	425	1300	1.197	499
Subsolvus	BL11	320	1300	0.997	16,951
Subsolvus	BL12	300	1300	0.797	12,185
Subsolvus	WL1	525	1300	0.999	3,121
Subsolvus	RL1	525	1300	0.802	9,133
Subsolvus	RL4	490	1300	1.195	1,214
Subsolvus	RL7	560	1300	0.601	963,423

Appendix 12—Tabulated Notch Fatigue Results

Disk	SpecID	Av. Cooling Rate Soln to 1600F-F/min	Temperature-F	Maximum Stress-ksi	LCF or FCG life -cycles	Notes
Supersolvus	BNL2	97	800	158	8,122	5Hz
Supersolvus	RNL3	130	800	137	15,061	5Hz
Supersolvus	BNL6	75	800	115	29,744	5Hz
Supersolvus	BNL5	75	800	94.5	218,404	5Hz
Supersolvus	RNL4	120	1300	137	4,675	5Hz
Supersolvus	BNL4	85	1300	126.5	18,242	5Hz
Supersolvus	RNL1	105	1300	116	187,412	5Hz
Supersolvus	BNL1	115	1300	126.5	456	90s dwell
Supersolvus	RNL2	100	1300	137	1,163	90s dwell
Subsolvus	BNL6	360	800	158	9,642	5Hz
Subsolvus	RNL3	550	800	137	15,831	5Hz
Subsolvus	BNL5	300	800	115	51,207	5Hz
Subsolvus	BNL4	350	800	105	621,145	5Hz
Subsolvus	RNL2	420	800	94.5	2560007+	5Hz, Runout
Subsolvus	BNL2	400	1300	158	2,168	5Hz
Subsolvus	RNL4	450	1300	137	57,722	5Hz
Subsolvus	BNL1	730	1300	115	2,163,114	5Hz
Subsolvus	RNL6	450	1300	126.5	14,112	90s dwell
Subsolvus	RNL1	500	1300	126.5	57	90s dwell

Appendix 13—Tabulated Fatigue Crack Growth Results

Disk	SpecID	Av. Cooling Rate Soln to 1600F-F/min	Temperature-F	da/dt at 20 ksi*in.5, in./sec	da/dt at 25 ksi*in.5, in./sec	da/dn at 20 ksi*in.5, in/cyc	da/dn at 25 ksi*in.5, in/cyc	Test Type
Supersolvus	BK2	66	800			2.7E-06	6.0E-06	0.33Hz
Supersolvus	WK1	110	75			5.0E-07	2.2E-06	0.33Hz
Supersolvus	WK2	90	400			9.5E-07	3.2E-06	0.33Hz
Supersolvus	RK3	110	1200			5.8E-06	9.8E-06	0.33Hz
Supersolvus	RK4	110	1300			7.3E-06	1.8E-05	0.33Hz
Supersolvus	BK1	66	1200	1.0E-07	3.9E-07			90s dwell
Supersolvus	RK1	130	1300	2.0E-06	4.5E-06			90s dwell
Supersolvus	RK2	130	1200	2.0E-07	3.2E-07			90s dwell
Subsolvus	BK2	360	800			4.0E-06	9.0E-06	0.33Hz
Subsolvus	WK1	425	75			2.0E-06	4.7E-06	0.33Hz
Subsolvus	WK2	340	400			2.2E-06	5.0E-06	0.33Hz
Subsolvus	RK3	425	1200			1.8E-05	3.5E-05	0.33Hz
Subsolvus	RK4	425	1300			2.8E-05	5.5E-05	0.33Hz
Subsolvus	BK1	360	1200	8.0E-07	1.8E-06			90s dwell
Subsolvus	RK1	470	1300		2.5E-05			90s dwell
Subsolvus	RK2	470	1200	8.5E-07	1.8E-06			90s dwell

REPORT DOCUMENTATION PAGE

Form Approved
OMB No. 0704-0188

1. AGENCY USE ONLY (*Leave blank*)	2. REPORT DATE	3. REPORT TYPE AND DATES COVERED
	June 2005	Technical Memorandum

4. TITLE AND SUBTITLE

Thermal and Mechanical Property Characterization of the Advanced Disk Alloy LSHR

5. FUNDING NUMBERS

WBS–22–079–30–09

6. AUTHOR(S)

Timothy P. Gabb, John Gayda, Jack Telesman, and Peter T. Kantzos

7. PERFORMING ORGANIZATION NAME(S) AND ADDRESS(ES)

National Aeronautics and Space Administration
John H. Glenn Research Center at Lewis Field
Cleveland, Ohio 44135–3191

8. PERFORMING ORGANIZATION REPORT NUMBER

E–15133

9. SPONSORING/MONITORING AGENCY NAME(S) AND ADDRESS(ES)

National Aeronautics and Space Administration
Washington, DC 20546–0001

10. SPONSORING/MONITORING AGENCY REPORT NUMBER

NASA TM—2005–213645

11. SUPPLEMENTARY NOTES

Timothy P. Gabb, John Gayda, and Jack Telesman, NASA Glenn Research Center; and Peter T. Kantzos, Ohio Aerospace Institute, 22800 Cedar Point Road, Brook Park, Ohio 44142. Responsible person, Timothy P. Gabb, organization code RMM, 216–433–3272.

12a. DISTRIBUTION/AVAILABILITY STATEMENT

Unclassified - Unlimited
Subject Category: 07

Available electronically at http://gltrs.grc.nasa.gov

This publication is available from the NASA Center for AeroSpace Information, 301–621–0390.

12b. DISTRIBUTION CODE

13. ABSTRACT ***(Maximum 200 words)***

A low solvus, high refractory (LSHR) powder metallurgy disk alloy was recently designed using experimental screening and statistical modeling of composition and processing variables on sub-scale disks to have versatile processing-property capabilities for advanced disk applications. The objective of the present study was to produce a scaled-up disk and apply varied heat treat processes to enable full-scale demonstration of LSHR properties. Scaled-up disks were produced, heat treated, sectioned, and then machined into specimens for mechanical testing. Results indicate the LSHR alloy can be processed to produce fine and coarse grain microstructures with differing combinations of strength and time-dependent mechanical properties, for application at temperatures exceeding 1300 °F.

14. SUBJECT TERMS

Gas turbine engines; Rotating disks; Heat resistant alloys; Mechanical properties; Thermal properties

15. NUMBER OF PAGES

81

16. PRICE CODE

17. SECURITY CLASSIFICATION OF REPORT	18. SECURITY CLASSIFICATION OF THIS PAGE	19. SECURITY CLASSIFICATION OF ABSTRACT	20. LIMITATION OF ABSTRACT
Unclassified	Unclassified	Unclassified	